AAE

AERONAUTICAL AND ASTRONAUTICAL ENGINEERING DEPARTMENT

ENGINEERING EXPERIMENT STATION, COLLEGE OF ENGINEERING, UNIVERSITY OF ILLINOIS, URBANA

AIR FORCE OFFICE OF SCIENTIFIC RESEARCH (AFSC)
NOTICE OF TRANSMITTAL TO DDC
This technical report has been reviewed and is approved for public release IAW AFR 190-12 (7b).
Distribution is unlimited.
A. D. BLOSE
Technical Information Officer

UNCLASSIFIED

SECURITY CLASSIFICATION OF THIS PAGE (When Data Entered)

REPORT DOCUMENTATION PAGE	READ INSTRUCTIONS BEFORE COMPLETING FORM
1. REPORT NUMBER (19) (1) AFOSR-TR- 77-0842	2. GOVT ACCESSION NO.
	3. RECIPIENT'S CATALOG NUMBER (9)
(6) 4. TITLE (and Subtitle) DIRECT INITIATION OF DETONATION BY NON-IDEAL BLAST WAVES,	5. TYPE OF REPORT & PERIOD COVERED INTERIM Rept.
(14)	6. PERFORMING ORG. REPORT NUMBER AAE-77-4, UILU-Eng-77-0504
(10) 7. AUTHOR(s) ROBERT JOHN CESARONE	8. CONTRACT OR GRANT NUMBER(s) AFOSR 73-2524
9. PERFORMING ORGANIZATION NAME AND ADDRESS UNIVERSITY OF ILLINOIS AT URBANA-CHAMPAIGN AERONAUTICAL AND ASTRONAUTICAL ENGINEERING DEPT URBANA, IL 61801	10. PROGRAM ELEMENT, PROJECT, TASK AREA & WORK UNIT NUMBERS 9711-02 61102F
11. CONTROLLING OFFICE NAME AND ADDRESS AIR FORCE OFFICE OF SCIENTIFIC RESEARCH/NA BLDG 410 BOLLING AIR FORCE BASE, D C 20332	(11) 12. REPORT DATE June 1977 13. NUMBER OF PAGES 77
14. MONITORING AGENCY NAME & ADDRESS (if different from Controlling Office) (12) 93p.	15. SECURITY CLASS. (of this report) UNCLASSIFIED 15a. DECLASSIFICATION/DOWNGRADING SCHEDULE

16. DISTRIBUTION STATEMENT (of this Report)

Approved for public release; distribution unlimited.

(15) AFOSR-TR-77-0842

17. DISTRIBUTION STATEMENT (of the abstract entered in Block 20, if different from Report)

(16) 9711 (17) 02F

18. SUPPLEMENTARY NOTES

19. KEY WORDS (Continue on reverse side if necessary and identify by block number)

DETONATION INITIATION
BLAST WAVES

20. ABSTRACT (Continue on reverse side if necessary and identify by block number)

This study is a theoretical investigation of the initiation of detonation by non-ideal blast waves. The study used the output of the CLOUD program as the source of flow data for blast waves generated by bursting spheres. Each cell that surrounds the bursting sphere is assumed to be reactive with an Arrhenius type kinetic rate law over a temperature range of from 1000 - 2700°K. Outside this range the cell is assumed to be nonreactive. In the technique the delay to explosion is integrated numerically from the time of shock passage over that cell until the temperature of the cell drops below 1000°K. A minimum of this

DD FORM 1 JAN 73 1473 EDITION OF 1 NOV 65 IS OBSOLETE

UNCLASSIFIED

SECURITY CLASSIFICATION OF THIS PAGE (When Data Entered)

176 700

summation time was found for cells either near the bursting sphere or right at the edge of the sphere. Conceptually, as the bursting sphere is made larger and larger one eventually reaches a point at which the delay time to explosion in at least one of the cells is long enough such that an explosion process can start. This is taken as the criterion for detonation initiation in this model. Numerous cases were run and initiation behavior was plotted both as a function of the total energy of the bursting sphere and the energy density of the bursting sphere. In addition, a few runs were made for the ramp edition of energy to compare to the bursting sphere results. The study shows that as the energy density of the sphere gas becomes lower the total energy required for initiation increases sharply. This is in agreement with experimental studies using spark initiation.

Aeronautical and Astronautical Engineering Department
University of Illinois at Urbana-Champaign

Technical Report AAE 77-4
UILU-Eng 77 0504

Prepared for

Air Force Office of Scientific Research
Aerospace Sciences Directorate
Bolling Air Force Base, D.C.

DIRECT INITIATION OF DETONATION BY NON-IDEAL BLAST WAVES

by

Robert J. Cesarone

Approved for public release; distribution unlimited
Grant No. AFOSR 73-2524 June 1977
Interim Technical Report
AFOSR-TR

TABLE OF CONTENTS

I. INTRODUCTION

Since the early 1940's, there have been a number of models for the process called detonation. These range from the early one-dimensional model of Zel'dovich and Kompaneets[1] to models taking account of three-dimensional structure including those of Barthel and Strehlow[2] and Barthel[3]. The one-dimensional model is well developed and the three-dimensional model, though less well understood, yet provides much qualitative insight into the mechanism responsible for the self-sustaining nature of the detonation.

Within the scope of the subject of detonation, one can specifically focus attention on the initiation process. Initiation is usually considered to include the following events. First, a shock wave travels through a combustible mixture, raising its temperature and pressure. Next an induction zone develops in which chemical reaction begins to take place. The temperature and pressure in this zone remain fairly constant as any heat release is approximately cancelled by a corresponding endothermic dissociation. The induction zone is characterized by the induction delay, also called the delay time to ignition, which is simply the time a particle of the mixture spends in the induction zone. Finally, the recombination or heat release region develops. This of course yields the observed exothermic nature of a detonation. As can be seen this entire process is non-steady.

It would be instructive to obtain a model for this initiation process which will yield the qualitative behavior which results as one varies input parameters such as temperature and shock overpressure. This then is the scope of this paper. A model for the initiation of shock induced detonation is developed for a spherical flow field. Two different types of non-ideal flow fields are then generated in which the initiation may occur.

These include flows generated by massless, high pressure, bursting spherical vessels and flows resulting from finite rate depositions of energy at a spherical region in space. For all these flow fields, the model then yields information on delay time to ignition, minimum energy requirements, sound speed effects and explosion loci.

II. BACKGROUND FLOW

The initiation process must occur in the flow field under consideration. This flow field is generated by a computer program, which was obtained from A. K. Oppenheim.[4] The CLOUD program, as it is called in this paper, uses a finite difference scheme to evaluate the fluid dynamic conservation equations in one-dimensional Lagrangian form. These include the continuity, momentum and energy equations. A fourth expression, the equation of state is also evaluated. The equation of state for this investigation takes the form of the perfect gas law.

The CLOUD program performs its calculations with non-dimensional variables. This fact is crucial to later computations because it allows one to substitute in desired reference parameters after a given computer run has been made.

The independent variables for the numerical computation are $\tau = t/t_0$ and $R = r/r_0$ where τ and r denote dimensional time and radial position and t_0 and r_0 are the reference parameters used to non-dimensionalize the calculations.

The dependent variables of prime importance are the specific volume and energy, which are given by $V = v/v_0$ and $E = e/P_0 v_0$ respectively, where again the v and e have dimensions and the subscripted symbols are used to non-dimensionalize the calculations. Other dependent variables which the CLOUD program calculates are velocity, pressure and viscosity. The pressure at various points in the flow field is used to determine the time of shock

passage even though the pressure does not enter into initiation calculations. The viscosity term is used to smooth out infinite gradients at the shock location, as these are unacceptable in the finite-difference computational scheme.

In order to validate the data concerning the flow field which are obtained from the CLOUD program, three comparison runs were made for the case of a bursting sphere. These include sphere bursts of 22 atm air into 1 atm ambient air and 15.79 atm helium into 1 atm ambient air. These runs are compared to corresponding runs made by Brode.[5] Also a high pressure sphere burst of 200 atm air into 1 atm ambient air is compared to a corresponding run made by Huang and Chou.[6] These data are shown graphically on Figs. 1-3. On these plots $\bar{P}_s$, the non-dimensional shock overpressure is shown as a function of non-dimensional energy scaled radius or shock location. $\bar{P}_s$ is determined from the expression

$$\bar{P}_s = \frac{P_s - P_0}{P_0} = \frac{P_s}{P_0} - 1 \tag{1}$$

where P_s is the value of the shock overpressure and P_0 is the ambient reference pressure. $\bar{R}_s$ is obtained from the expression

$$\bar{R}_s = \frac{R_s}{R_0} \tag{2}$$

where R_s is the location of the shock and R_0 is called the scaling radius and is determined by the following relation, as discussed in Strehlow and Ricker.[7]

$$R_0 = \left[\frac{I_1}{P_0}\right]^{1/3} \tag{3}$$

Here P_0 again represents the ambient reference pressure and I_1 is the

amount of energy which must be added to a sphere at ambient conditions to raise its temperature and pressure to the conditions necessary for the burst. This energy addition is assumed to occur instantaneously and at constant volume. E_1 is found from the relation,

$$E_1 = \frac{4\pi}{3} \frac{P_2 - P_o}{\gamma_1 - 1} r_o^3 \tag{4}$$

where P_2 is the pressure in the sphere just prior to burst, γ_1 is the specific heat ratio of the gas in the sphere and r_o is the initial radius of the sphere. Then substituting eqn. 4 into eqn. 3 and the resulting form of eqn. 3 into eqn. 2, it is found that

$$\bar{R}_s = \frac{R_s}{\left[\frac{4\pi}{3} \frac{P_a - P_o}{P_o} \frac{1}{\gamma_1 - 1}\right]^{1/3} r_o} \tag{5}$$

It must also be noted that in Figs. 1-3 the first point is not obtained from the finite-difference calculation but is determined analytically from the shock wave-rarefaction contact surface requirement, as found in Liepmann and Roshko.[8]

$$\frac{P_a}{P_o} = \frac{P_s}{P_o}\left[1 - \frac{(\gamma_1 - 1)(a_o/a_s)(P_s/P_o - 1)}{\sqrt{2\gamma_o}\sqrt{2\gamma_o + (\gamma_o+1)(P_s/P_o - 1)}}\right]^{\frac{-2\gamma_1}{\gamma_1 - 1}} \tag{6}$$

where a_o refers to the ambient sound speed, a_2 is the sphere sound speed just prior to burst and γ_o is the specific heat ratio in the ambient air. All other quantities are the same as defined previously. Eqn. 6 is iteratively solved for the quantity P_s/P_o which is then substituted into eqn. 1 to obtain the initial point.

Also shown in Figs. 1-3 are data obtained from another numerical program. This other program, known as the WINDY program was obtained from H. M. Sternberg.[9] As can be seen the CLOUD and WINDY data are in

very good agreement. This will then be taken as evidence of the accuracy and validity of data obtained from the CLOUD program.

III. IGNITION MODEL

The ignition model analyzed in this investigation is viewed as a simple one-dimensional model which will allow a parameter study of the problem. General trends and behavior are sought rather than specific numerical values. With this in mind then, the following procedure is employed.

As given in Cusey[10] the local delay time to ignition for a hydrogen-oxygen system is given by the formula,

$$\tau_i = \frac{A}{[O_2]} \exp(E_A/RT) \tag{7}$$

where A is called the pre-exponential factor, $[O_2]$ is the oxygen concentration, E_A in the chemical activation energy, R is the universal gas constant and T is the temperature. The local delay time will refer to a particular particle or "cell" in the flow field. Thus at each instant of time, each particle in the flow will have an instantaneous value of local delay time, τ_i. We can then define the variable Ψ to be the fraction of total delay time consumed, where the total delay time is equal to the time spent in the induction zone. Ψ is then given by the following expression taken from Strehlow,[11]

$$\Psi = \int_{t_s}^{t} \frac{dt}{\tau_i} \tag{8}$$

where t_s refers to the time of shock passage.

The basic approach is to integrate eqn. 8 along a particle path until its value is equal to unity. This will correspond to the location

in space and time when the particle leaves the induction zone and ignites, The Lagrangian approach is thus seen to be very useful as one must integrate eqn. 8 while following individual particles in the flow. Eqn. 8 must be cast into a slightly different form for use with the CLOUD program. This will be discussed later.

It is now necessary to specify the combustible mixture and the chemical kinetics to be studied. For simplicity, all computer runs were made with the expanding shock wave passing into ambient air with $\gamma_o = 1.4$. Air is not a combustible mixture but it is assumed that there is enough H_2 for a reaction. In this analysis only particles or cells which are outside of the pressurized sphere or region of energy addition are considered to be combustible. Then as the flow progresses, a contact surface will always separate these two regions. Cells inside of this contact surface are not followed as they are not considered to be combustible. Cells outside of the contact surface are followed as they are considered to be combustible and hence are necessary for the delay time calculations. The inside cells do however serve the purpose of providing the necessary energy for the establishment of the shock wave which processes the combustible mixture. This is illustrated in Fig. 4 for the case of a bursting sphere. Note that the outward travelling shock wave begins at the contact surface but because of the infinite gradients involved, this area must initially be smoothed out over the space of two particles, known as fairing cells.

For the actual reaction, a simple hydrogen-oxygen system is considered. Schott and Kinsey[12] have shown that the primary reactions involved are:

$$H_2, O_2 \longrightarrow H_2O \text{ or } OH \qquad \text{(i)}$$

$$H + O_2 \longrightarrow OH + O \qquad \text{(ii)}$$

$$O + H_2 \longrightarrow OH + H \qquad \text{(iii)}$$

$$OH + H_2 \longrightarrow H_2O + H \qquad \text{(iv)}$$

where reaction (ii) is the most highly endothermic reaction in the chain (reactions ii, iii and iv). For this system of reactions, Schott and Kinsey[12] and Strehlow[13] show plots of local delay time times oxygen concentration vs. 1000 over the temperature. From these plots the quantities E_A, the activation energy and A, the pre-exponential factor can be determined. The plot from Strehlow is reproduced in Fig. 5. The above quantities are found in the following way.

We have that that the local delay time is given by eqn. 7, repeated here

$$\tau_i = \frac{A}{[O_2]} \exp(E_A/RT) \tag{7}$$

Then

$$\log_{10}\{[O_2]\tau_i\} = \log_{10}\{A e^{E_A/RT}\}$$

$$= \frac{\ln\{A e^{E_A/RT}\}}{\ln 10}$$

$$= \frac{1}{\ln 10}\left[\ln A + \ln e^{E_A/RT}\right]$$

$$= \frac{1}{\ln 10}\left[\ln A + E_A/RT\right]$$

or

$$\log_{10}\{[O_2]\tau_i\} = \frac{\ln A}{\ln 10} + \frac{E_A}{R \ln 10}\cdot\frac{1}{T} \tag{9}$$

Notice that this equation is of the form $y = mx + b$ where

$$y = \log_{10}\{[O_2]\cdot\tau_i\}$$

$$m = \frac{E_A}{R \ln 10}$$

$$x = \frac{1}{T}$$

and

$$b = \frac{\ln A}{\ln 10}$$

The slopes and intercepts on the Strehlow and Schott and Kinsey graphs can be determined and then the values of E_A and A follow. These values are shown in Table I below.

Investigator	$m = \frac{E_A}{R\ell n\ 10}$	$b = \frac{\ell nA}{\ell n\ 10}$	E_A(kcal/mole)	$A\left(\frac{\text{sec-moles}}{\text{liter}}\right)$
Strehlow	3541.18	- 10.165	16.19	6.8418×10^{-11}
Schott & Kinsey	3966	- 10.647	18.14	2.2542×10^{-11}

TABLE 1

At this point an arbitrary choice was made to use the values obtained from Strehlow for the initiation and delay time calculations. It was felt that this is justified by the fact that the two sets of values are in fairly good agreement. Also, the actual numbers are not of that great a concern since the main purpose of this work is to determine qualitative behavior.

To completely determine the chemical kinetics, the range of temperatures for which the hydrogen-oxygen reactions discussed earlier are valid must be stated. Schott and Kinsey studied hydrogen-oxygen reactions in the temperature range between 1100° and 2600°K. Slightly broader limits were chosen for this work, specifically 1000° to 2700°K. Again this is a fairly arbitrary choice but the limits used correspond roughly to values of three to nine times the usual standard atmosphere ambient air temperature at sea level. In this temperature range then, the simple Arrhenius kinetics are assumed to hold for the chemical process under consideration. Below 1000°K, the temperature is assumed to be low enough that no appreciable reaction will occur. Above 2700°K, there is assumed to be so much endothermic dissociation that no appreciable fraction of the total delay time will be used up. This situation is shown in Fig. 6.

Next it is necessary to derive the specific form of eqn. 8 which is usable with CLOUD program output for initiation and delay time studies. Since CLOUD uses non-dimensional values of time the quantity dt is not directly obtainable. However, the quantity dt/t_0 is obtainable where t_0

has been defined previously. Thus one can write

$$\psi_{CLOUD} = \int_{t_s/t_o}^{t/t_o} \frac{dt/t_o}{\tau_i} = \frac{1}{t_o}\psi \tag{10}$$

Now all that remains is to substitute the expression for τ_i into eqn. 10. However τ_i is given in terms of the oxygen concentration and the temperature of a cell of the combustible mixture. Thus expressions must first be found for these two quantities.

To determine the cell temperature, one may proceed as follows. Since for a perfect gas the temperature is a function of the internal energy only, we see that the cell temperature can be obtained from the cell energy, which is a part of the CLOUD program output. As noted earlier CLOUD yields a value of $E = e/P_o v_o$, where e is the actual internal energy per unit mass and P_o and v_o are non-dimensionalizing reference quantities. It can also be shown that for a perfect gas

$$e = \frac{P v}{\gamma_o - 1} \tag{11}$$

We may then substitute eqn. 11 into the CLOUD expression for cell energy to obtain,

$$E = \frac{e}{P_o v_o} = \frac{P v}{P_o v_o} \frac{1}{\gamma_o - 1} \tag{12}$$

which by the perfect gas law may be re-written as

$$E = \frac{RT}{R_o T_o} \frac{1}{\gamma_o - 1} \tag{13}$$

where T_o is the initial ambient temperature and R_o is the gas constant of the ambient gas. But since we are considering that the ambient gas is the

combustible mixture we can say that $R = R_o$ and eqn. 13 reduces to

$$E = \frac{T}{T_o} \frac{1}{\gamma_o - 1}$$

or rearranging, we obtain an expression for the cell temperature as

$$T = E T_o (\gamma_o - 1) \tag{14}$$

Finally the oxygen concentration, $[O_2]$ must be determined. Since A, the pre-exponential factor is given with the units $\frac{\text{sec-moles}}{\text{liter}}$, we require to have $[O_2]$ in the units $\frac{\text{moles}}{\text{liter}}$ so that in eqn. 7 we will be left with units of time only. The expression for $[O_2]$ is then given by

$$[O_2]\frac{\text{moles}}{\text{liter}} = \left[\left(\rho \frac{g}{\text{liter}}\right)/\left(MW \frac{g}{\text{gmole}}\right)\right] M.F. \tag{15}$$

where ρ and MW refer to the density and molecular weight of the cell in question and M.F. refers to the mole fraction of O_2.

The density of a cell is not obtainable directly from CLOUD. However the specific volume ratio v/v_o is. Then because $\rho = 1/v$ we have

$$\frac{\rho}{\rho_o} = \frac{v_o}{v} = 1/\left(\frac{v}{v_o}\right)$$

where again the subscript refers to initial ambient conditions. Then ρ is given by

$$\rho = \rho_o/\left(\frac{v}{v_o}\right) \tag{16}$$

Eqn. 16 is then substituted back into eqn. 15 to obtain the expression for $[O_2]$.

$$[O_2]\frac{\text{moles}}{\text{liter}} = \left[\left(\rho_o \frac{g}{\text{liter}}\right)/\left(\frac{v}{v_o}\right)\left(MW \frac{g}{\text{gmole}}\right)\right] M.F. \tag{17}$$

Eqns. 14 and 17 may then be substituted back into eqn. 7 to obtain an expression for τ_i,

$$\tau_i = \frac{A}{\left[\left(\rho_o \frac{g}{liter}\right)/\left(\frac{V}{V_o}\right)\left(MW \frac{g}{gmole}\right)\right] M.F.} \exp\left(E_A/RET_o(\gamma_o - 1)\right)$$

$$= \frac{A\left(\frac{V}{V_o}\right)\left(MW \frac{g}{gmole}\right)}{\left(\rho_o \frac{g}{liter}\right) M.F.} \exp\left(E_A/RET_o(\gamma_o - 1)\right) \qquad (18)$$

We can now substitute into eqn. 18 numerical values for the following quantities,

$A = 6.8418 \times 10^{-11} \frac{sec\text{-}moles}{liter}$ (from Strehlow)

$E_A = 16.19 \frac{kcal}{mole}$ (from Strehlow)

$MW_{MIXTURE} = MW_{AIR} = 28.97 \frac{g}{gmole}$

$\rho_o = 1.2247 \frac{g}{liter}$

$M.F._{O_2} = .21$

$R = .001986 \frac{kcal}{gmole - {}^oK}$

$T_o = 298\ {}^oK$

$\gamma_o = 1.4$

Using these values then eqn. 18 reduces to

$$\tau_i = 7.7067 \times 10^{-9} \left(\frac{V}{V_o}\right) \exp(68.3898/E) \qquad (19)$$

where τ_i has units of seconds. Recall also that E is the non-dimensional cell energy obtained from CLOUD.

Eqn. 19 is now substituted back into eqn. 10 to obtain,

$$\psi_{CLOUD} = \int_{t_e/t_o}^{t/t_o} \frac{dt/t_o}{7.067 \times 10^{-9}\left(\frac{V}{V_o}\right) \exp(68.3898/E)} = \frac{1}{t_o}\psi$$

$$= \int_{t_i/t_o}^{t/t_o} \frac{(1.2976 \times 10^8)\, e^{-(68.3898/E)}}{\left(\frac{V}{V_o}\right)} \frac{dt}{t_o} = \frac{1}{t_o}\psi \qquad (20)$$

where the factor $\frac{1.2976 \times 10^8\ e^{-(68.3898/E)}}{(V/V_o)}$ is equal to $1/\tau_i$.

Eqn. 20 is now integrated numerically from the non-dimensional time of shock passage to the time t/t_o. For this calculation, eqn. 20 is re-written as:

$$\psi_{CLOUD} = \sum_{t_s/t_0}^{t/t_0} \frac{(12976 \times 10^8)\, e^{-(68.3898/E)}}{\left(\frac{V}{V_0}\right)} \frac{\Delta t}{t_0} = \frac{1}{t_0}\psi \qquad (21)$$

or more compactly,

$$\psi_{CLOUD} = \sum_{t_s/t_0}^{t/t_0} \frac{1}{\tau_i} \frac{\Delta t}{t_c} = \frac{1}{t_0}\psi \qquad (22)$$

where $1/\tau_i$ has been defined above. Note that the quantity ψ_{CLOUD} has units of sec^{-1} and that ψ is dimensionless.

The actual integration is then performed using eqn. 22 or equivalently eqn. 21 on an IBM 360 computer. The limits of integration are t_s/t_0 and t/t_0 as shown above. However, it must be noted that eqn. 22 was derived with the assumption that the reactive kinetics are valid only between the temperatures of 1000° and 2700°K. If the cell temperature drops below 1000°K, the integration is temporarily halted. If the cell temperature rises above 2700°K, the integration is likewise temporarily halted. If and when the cell temperature returns to the acceptable range, the integration is then resumed. Thus the actual limits of integration may be narrower than those given above.

In Fig. 7 are shown qualitatively four different types of temperature variation which may be observed for a given cell. In Fig. 7a, the shock passes the cell in question and raises its temperature. However, the temperature never reaches the 1000°K point. This cell will then never begin reaction, its ψ value will remain zero and it will have an infinite delay time, i.e., it will not ignite. Fig. 7b shows a cell for which the temperature does rise above 1000°K after shock passage. Once past the point of highest temperature, there is a monotonic decrease until the temperature is once again below the 1000°K cutoff limit. While this cell has a temperature in the acceptable range, integration of eqn. 22 along its

trajectory will proceed. Thus this cell will undergo reaction and have finite values of ψ and delay time. This cell may or may not reach the point of ignition. This will depend on the initial dimensional conditions and will be discussed later. Fig. 7c shows a cell for which the temperature rises above the upper cutoff limit. This cell will undergo the same procedure as that for the cell of Fig. 7b except that during the time when the temperature is above the 2700°K point, the integration of eqn. 22 will be temporarily halted. This integration will resume when the temperature has dropped below 2700°K and will proceed as long as the temperature is greater than 1000°K. All else is the same. Finally, Fig. 7d shows a temperature-time plot for which non-ideal effects are pronounced. Due to the non-ideal nature of the flow, second, third, etc. shocks may propagate past a cell after the lead shock has passed. The effect of these later shocks is to cause a temperature perturbation on the generally decreasing temperature profile. These perturbations raise the temperature of the cell but not by as much as the lead shock raised the temperature. As shown in the plot, a perturbation can occur in such a way as to raise the temperature above the upper limit and so cause a temporary halt in the integration. It can also raise the temperature above the lower limit and hence allow a longer integration for a cell for which the integration would otherwise have been completed.

With this information in mind then, eqn. 2. is integrated along the necessary particle or cell trajectories to obtain the data for this investigation.

IV. TEST CASE

To determine the validity of the numerical integrating scheme, a test case was run with the Huang and Chou 200 atm bursting sphere run described earlier. The numerical integrating scheme was run on a number of cells

for this sphere burst. Two of these cells are discussed here, namely cell 130 and cell 135. For these two cells, the quantity $1/\tau_i$ was also obtained at various times during the integration period. Plots were then made of $1/\tau_i$ vs t/t_o for these cells. These are shown in Figs. 8 and 9. As eqn. 22 can also be integrated graphically by determining the area under the $1/\tau_i$ vs t/t_o graph this was also done and used as a check on the numerical scheme. In Figs. 8 and 9 the cross-hatched areas represent half time increments which were included to make the graphical integration correspond exactly to the numerical integration. The area under these curves was then determined by a planimeter.

For cell 130, the numerical scheme yielded a value for Ψ_{CLOUD} of 3.379×10^4 sec^{-1}. The planimeter integration yielded a value of 3.376×10^4 sec^{-1}. The percent error can then be determined from,

$$\% \text{ error} = \frac{\left|\Psi_{CLOUD(NUMERICAL)} - \Psi_{CLOUD(PLANIMETER)}\right|}{\Psi_{CLOUD(PLANIMETER)}} \times 100 \qquad (23)$$

For cell 130, eqn. 23 yields a value of .09% error.

For cell 135, the numerical scheme yielded a value for Ψ_{CLOUD} of 1.622×10^4 sec^{-1} whereas the planimeter yielded a value of 1.62×10^4 sec^{-1}. Eqn. 23 then gives a value of .12% error for cell 135.

These values of percentage error are certainly within an acceptable error margin and so this is taken as evidence that the numerical integration is returning valid output.

Also shown for illustrative purposes is Fig. 10, which is a three-dimensional plot of Ψ_{CLOUD} vs cell number vs t/t_o, where Ψ_{CLOUD} was obtained with the numerical integration. Note that for all the cells plotted, a large fraction of the final value of Ψ_{CLOUD} is obtained very quickly, even for the first four cells in which the integration proceeds for a long time. Note also that Ψ_{CLOUD} may attain a value greater than unity even though Ψ

itself is limited by this value. This fact becomes important for explosion loci determination and will be discussed below.

It is desired to determine three things for the Huang and Chou 200 atm case: the delay time to ignition for various cells, explosion loci and minimum energy requirements for ignition.

First of all, the value of Ψ_{CLOUD} was obtained for a number of cells for this run. These values are plotted vs cell number on Fig. 11. Notice again that Ψ_{CLOUD} can be greater than unity. Eqn. 22 can be re-written simply as:

$$\Psi_{CLOUD} = \frac{1}{t_o} \Psi \tag{22}$$

Now for a cell to ignite, its value of Ψ must be equal to unity. Then eqn. 22 reduces to:

$$\Psi_{CLOUD} = \frac{1}{t_o}$$

or

$$t_o = \frac{1}{\Psi_{CLOUD}} \tag{24}$$

Thus knowing the value of Ψ_{CLOUD}, the value of t_o, which has been used to non-dimensionalize the time variable can be determined. Then, knowing the value of t/t_o at which Ψ_{CLOUD} for the cell is such that it causes Ψ for the cell to equal unity, one can easily determine the real time t_{DELAY} for the cell to ignite from:

$$t_{DELAY} = \left(\frac{t}{t_o}\right)_{\Psi=1} t_o \tag{25}$$

Suppose now that one looks at the maximum value of Ψ_{CLOUD} on Fig. 11. This is equal to 1.962×10^6 sec^{-1} and occurs for cell 82. Substituting this value into eqn. 24 one finds that $t_o = 5.097 \times 10^{-7}$ sec. From the computer output, it is known that cell 82 sums to a value of $\Psi_{CLOUD} = 1.962 \times 10^6$ sec^{-1} at non-dimensional $t/t_o = 1.155$. Thus from eqn. 25, for cell 82

$$t_{DELAY} = (1.155)(5.097 \times 10^{-7}\ sec.)$$

$$= 5.887 \times 10^{-7}\ sec.$$

If the value of ψ_{CLOUD} for cell 82 and the value of t_o just determined are entered back into eqn. 22, they will of course yield a value of $\psi = 1$ for cell 82. However, if the value of ψ_{CLOUD} for any other cell in the Huang and Chou run is entered into eqn. 22 with the given t_o, it will yield a value $\psi < 1$. Thus only cell 82 will undergo ignition.

Suppose however, that one considers a value of ψ_{CLOUD} which is less than the maximum value of ψ_{CLOUD}, e.g. $\psi_{CLOUD} = 1.855 \times 10^6\ sec^{-1}$, which is the value obtained for cell 83. Then from eqn. 24, we obtain $t_o = 5.391 \times 10^{-7}$ sec. From eqn. 25 we get for cell 83 $t_{DELAY} = 6.119 \times 10^{-7}$ sec. where the value of t/t_o for which ψ_{CLOUD} was completely summed was obtained from the computer output. Again, entering the value of ψ_{CLOUD} for cell 83 with the t_o just determined back into eqn. 22 gives $\psi = 1$, as expected. Suppose that one now looks at cells 80, 81, and 82. These cells have values of ψ_{CLOUD} which are greater than the value obtained for cell 83. So when these values are entered back into eqn. 22 with the t_o given above, they will yield values which are greater than unity. This means that in addition to cell 83, these other three cells will also ignite. Of course, ψ can not physically exceed unity. What is done to correct this is to look at the value of t/t_o for which each of these cells attained the value, $\psi_{CLOUD} = 1.855 \times 10^6 sec^{-1}$. This is of course the value of ψ_{CLOUD} for cell 83. Any further summation beyond this value is then ignored. Now all of these cells will yield $\psi = 1$ in eqn. 22.

One can of course consider values of ψ_{CLOUD} which are still lower, e.g. $\psi_{CLOUD} = 1.656 \times 10^6 sec^{-1}$, the value obtained for cell 85. Now, all the cells from 79 to 85 will ignite. Their various ignition parameters

may be determined as above.

Since each value of ψ_{CLOUD} uniquely determines a value of t_o, we can now work back to obtain dimensional initial conditions for the bursting sphere. This is done as follows. Adamczyk[14] shows that there is a relation between t_o and r_o, the initial sphere size. This is given by:

$$t_o = \frac{r_o \sqrt{\gamma_1}}{a_o} \tag{26}$$

where a_o refers to the ambient undisturbed sound speed and γ_1 is as defined earlier. For a perfect gas, the quantity a_o can be replaced by,

$$a_o = \sqrt{\gamma_o R_o T_o} \tag{27}$$

Thus

$$t_o = \frac{r_o \sqrt{\gamma_1}}{\sqrt{\gamma_o R_o T_o}}$$

However, since this investigation assumes air on both sides of the contact surface (for flow field determination) we have that $\gamma_o = \gamma_1 = 1.4$ and

$$t_o = \frac{r_o}{\sqrt{R_o T_o}}$$

which can be re-written as

$$r_o = t_o \sqrt{R_o T_o} \tag{28}$$

where t_o is determined from ignition analysis as above, $R_o = R_{AIR}$ $= 6.855 \times 10^{-5} \frac{kcal}{g-°K}$ and $T_o = 298°K$. Eqn. 28 yields the initial radius, r_o of the bursting sphere.

One can then use this value of r_o in eqn. 4,

$$E_1 = \frac{4\pi}{3} \frac{p_s - p_o}{\gamma_1 - 1} r_o^3 \tag{4}$$

to obtain the quantity E_1, which as discussed earlier, is the amount of energy which must be added to yield the initial sphere burst conditions.

Table 2 displays the ignition data discussed above. For three values of ψ_{CLOUD}, the values of $(t/t_o)_{\psi=1}$ and t_{DELAY} are shown for cells 79 through 85. Also included are the values of t_o, r_o and E_1 for each case.

TABLE 2

C E L L	$\psi_{CLOUD} = 1.962\times10^{6}$ sec^{-1} $t_o = 5.097\times10^{-7}$ sec $r_o = 1.491\times10^{-2}$ cm $E_1 = 6.992\times10^{-4}$ joules		$\psi_{CLOUD} = 1.855\times10^{6}$ sec^{-1} $t_o = 5.391\times10^{-7}$ sec $r_o = 1.577\times10^{-2}$ cm $E_1 = 8.273\times10^{-4}$ joules		$\psi_{CLOUD} = 1.656\times10^{6}$ sec^{-1} $t_o = 6.039\times10^{-7}$ sec $r_o = 1.766\times10^{-2}$ cm $E_1 = 1.163\times10^{-3}$ joules	
	$(t/t_o)_{\psi=1}$	t_{DELAY}(sec)	$(t/t_o)_{\psi=1}$	t_{DELAY}(sec)	$(t/t_o)_{\psi=1}$	t_{DELAY} (sec)
79	∞	∞	∞	∞	.290	1.75×10^{-7}
80	∞	∞	.775	4.178×10^{-7}	.230	1.389×10^{-7}
81	∞	∞	.340	1.833×10^{-7}	.201	1.214×10^{-7}
82	1.155	5.887×10^{-7}	.300	1.617×10^{-7}	.195	1.178×10^{-7}
83	∞	∞	1.135	6.119×10^{-7}	.227	1.371×10^{-7}
84	∞	∞	∞	∞	.295	1.782×10^{-7}
85	∞	∞	∞	∞	1.115	6.733×10^{-7}

Fig. 12 shows a plot of the dimensional ignition delay times vs cell number for the given values of E_1 in the table above. Note that cell 82 has the shortest delay time for all three energy levels. This makes intuitive sense because cell 82 had the highest value of ψ_{CLOUD}. However, it may occur that another cell will sum to a given value of ψ_{CLOUD} before cell 82 does, even though cell 82 eventually sums to the highest value. In such a case, if that value of ψ_{CLOUD} is chosen as a reference for an ignition analysis, cell 82 will not have the shortest delay time. Thus one can not say in general that cell 82 will always ignite first.

It is also seen from Fig. 12 that as the energy added to the bursting sphere, E_1 increases, the delay time for all the cells decreases. Again, this makes intuitive sense because one would expect a quicker reaction for a larger amount of energy in the source area.

Fig. 13 shows a pictorial view of the Huang and Chou 200 atm flow field generated by the CLOUD program. On this graph, the axes are non-dimensional distance r/r_o vs non-dimensional time t/t_o. The particle paths or cell trajectories are shown. The lead shock is very evident in the lower left corner. Initially, the cells travel vertically, i.e., they cover no distance with time and are stationary. When the lead shock arrives, it bends the trajectories towards the horizontal, i.e., it accelerates the particles and hence causes a change in distance with time. As can be seen, the particles eventually decelerate and tend back toward a vertical inclination. As mentioned earlier, due to the non-ideal nature of the flow, secondary wave systems will occur. These can be seen as ripples superimposed on the general behavior of the cell trajectories.

The blocked-off portion of Fig. 13 is the area of the flow field which is of interest for ignition calculations. This region is magnified and displayed in Fig. 14. Recall that in Table 2 the quantity $(t/t_o)_{\psi=1}$ was tabulated against cell number for various energy levels, E_1. For each of these energy levels, one can plot the points at which ignition occurs for cells in question by simply locating the proper trajectory and travelling along it until the required value of t/t_o on the vertical axis is reached. These points can then be connected to form what will be called the explosion loci. These loci are plotted for two energy levels, namely $E_1 = 8.273 \times 10^{-4}$ joules and $E_1 = 1.163 \times 10^{-3}$ joules in Fig. 14.

Note that the explosion locus for the lower value of the energy is higher up the cell trajectories. This corresponds to the fact that a lower

energy will result in a longer time for reaction, as was discussed earlier. The explosion locus for the energy level $E_1 = 6.992 \times 10^{-4}$ joules is not shown as it is only a single point.

By this time, it should be evident that there is something special about the $E_1 = 6.992 \times 10^{-4}$ joules energy level, because it allows only one particle in the entire flow field to ignite. What this means is that this is the minimum amount of energy which will result in an ignition in the Huang and Chou 200 atm flow field. If this energy were decreased slightly, it would cause every particle in the flow field to have an infinite delay time which means of course that there would be no ignition of any kind. Thus this value of E_1 represents a cutoff between ignition and no ignition for this particular flow field. The values of the lowest energies for ignition will be obtained for other flow fields in the following sections and the general behavior of these quantities will be discussed.

V. BURSTING SPHERE RESULTS

The above procedure described for the Huang and Chou case has also been applied to a number of other bursting sphere runs. These sphere bursts are generated by the CLOUD program and are characterized by three parameters: the pressure ratio P_2/P_0, the temperature ratio T_2/T_0 and the values of γ for the source region and ambient region, called γ_1, and γ_0 respectively. For all the flow fields generated by the CLOUD program, the source and ambient regions are assumed to contain air. Thus $\gamma_1 = \gamma_0 = 1.4$.

It is first necessary to determine which combinations of these parameters will lead to flow fields in which initiation may occur. This criterion can be determined analytically in the following manner.

We have set the minimum temperature for reaction at 1000°K. Therefore

the flow field must show temperatures at least this high behind the incident shock. Now for a bursting sphere, the shock will have maximum strength at the instant of burst. From this point on it will decay, eventually to approach an acoustic-type behavior. Thus at the moment of burst, the shock must be capable of raising the temperature of the mixture to 1000°K. One can now use the Rankine-Hugoniot relation for temperature from Liepmann and Roshko.[8]

$$\frac{T_s}{T_o} = \frac{P_s}{P_o} \frac{\frac{\gamma+1}{\gamma-1} + \frac{P_s}{P_o}}{1 + \frac{\gamma+1}{\gamma-1}\frac{P_s}{P_o}} \tag{29}$$

where T_s/T_o is the temperature ratio across the shock, P_s/P_o is the pressure ratio across the shock and γ replaces γ_1 and γ_o since it was assumed that $\gamma_1 = \gamma_o = \gamma = 1.4$. If $T_o = 298°K$ and at the moment of burst we must have 1000°K behind the shock then,

$$\frac{T_s}{T_o} = \frac{1000°K}{298°K} = 3.3557$$

We can then substitute this value of T_s/T_o and $\gamma = 1.4$ back into eqn. 29. After some rearrangement it is found that

$$\left(\frac{P_s}{P_o}\right)^2 - 14.1342\left(\frac{P_s}{P_o}\right) - 3.3557 = 0$$

This is a quadratic in the quantity P_s/P_o. It may be solved to yield the values

$$\frac{P_s}{P_o} = 14.3678\ ,\ -0.2336$$

where the negative solution is not physically meaningful. We now have the pressure ratio across the shock at the instant of burst which is necessary to produce a 1000°K temperature. Recall eqn. 6

$$\frac{P_2}{P_0} = \frac{P_s}{P_0}\left[1 - \frac{(\gamma-1)\ (a_0/a_2)(P_s/P_0-1)}{\sqrt{2\gamma}\sqrt{2\gamma+(\gamma+1)(P_s/P_0-1)}}\right]^{\frac{-2\gamma}{\gamma-1}} \quad (6)$$

where γ has now replaced γ_1 and γ_0. The quantity (a_0/a_2) may be expressed as,

$$\frac{a_0}{a_2} = \sqrt{\frac{\gamma_0 R_0 T_0}{\gamma_1 R T_2}}$$

Again because we are considering air for the flow field calculations, the specific heat ratio and gas constant ratio drop out and we have

$$\frac{a_0}{a_2} = \left(\frac{T_0}{T_2}\right)^{1/2}$$

$$\frac{a_0}{a_2} = \left(\frac{T_2}{T_0}\right)^{-1/2} \quad (30)$$

Substituting eqn. 30 back into eqn. 6 we obtain

$$\frac{P_2}{P_0} = \frac{P_s}{P_0}\left[1 - \frac{(\gamma-1)(T_2/T_0)^{-1/2}\ (P_s/P_0-1)}{\sqrt{2\gamma}\sqrt{2\gamma+(\gamma+1)(P_s/P_0-1)}}\right]^{\frac{-2\gamma}{\gamma-1}}$$

which, after substituting in the values determined for γ and P_s/P_0, reduces to,

$$\frac{P_2}{P_0} = 14.3678\left[1 - .5410\left(\frac{T_2}{T_0}\right)^{-1/2}\right]^{-7} \quad (31)$$

Eqn. 31 now relates the initial sphere pressure ratio to the initial sphere temperature ratio, while satisfying the constraint of a 1000°K temperature behind the lead shock at the instant of burst.

Suppose the minimum temperature defined for the Arrhenius reaction kinetics had been 1200°K instead of 1000°K. Although this criterion is not made use of in this investigation, it can be mentioned for comparison purposes. If this were the case however, then an equation similar to eqn. 31 could be derived using the same logic. This equation would be,

$$\frac{P_a}{P_o} = 18.3799 \left[1 - .6227 \left(\frac{T_a}{T_o}\right)^{-1/2}\right]^{-7} \qquad (32)$$

Eqns. 31 and 32 are plotted on Fig. 15 for comparison purposes. For a 1000°K minimum temperature it can be seen that only points which are to the right and above the 1000°K curve will provide the proper initial sphere conditions for an ignition. No set of initial sphere conditions below and to the left of the curve will produce an ignition in the flow field. A corresponding argument can be made for the 1200°K curve.

Note that the curve for a 1200°K minimum temperature lies higher on the graph than the curve for 1000°K. This makes sense because one would expect that it would require larger initial values of sphere temperature and pressure ratios to cause a higher temperature in the flow field. Note also that for either curve as the temperature ratio decreases to zero the pressure ratio rises very rapidly. Likewise, the required temperature ratio increases markedly as the pressure ratio decreases. Also shown on this graph is the curve of temperature ratio equal to pressure ratio.

For this investigation a number of bursting sphere runs were made to study the ignition behavior in the flow field. The initial conditions for all of these runs lie above and to the right of the 1000°K curve. The intersection of the 1000°K curve and the curve of temperature ratio equal to pressure ratio was chosen as a starting point. This intersection corresponds to the initial conditions:

$$\frac{P_a}{P_o} = 30 \qquad \frac{T_a}{T_o} = 30$$

As this set of initial conditions lies on the 1000°K cutoff curve, it was not expected to yield any actual finite ignition data with the numerical routine. Thus to provide the numerical integration with a flow field slightly above the cutoff flow field, the above initial conditions were increased by ten percent. Thus

$$\frac{P_a}{P_o} = 33 \qquad \frac{T_a}{T_o} = 33$$

Then with this set of more reasonable initial conditions as a starting point, eight bursting sphere flow fields were generated. Four of these flow fields successively doubled the initial pressure ratio while holding the initial temperature ratio constant. The other four flow fields successively doubled both the initial pressure and temperature ratios. These flow fields, or equivalently computer runs, as they will henceforth be called are displayed in Tables 3a and 3b.

FLOW FIELD/RUN	PRESSURE RATIO	TEMPERATURE RATIO
THEORETICAL CUTOFF	30	30
A) 10% ABOVE CUTOFF	33	33
1	66	33
2	132	33
3	264	33
4	528	33

(a)

FLOW FIELD/RUN	PRESSURE RATIO	TEMPERATURE RATIO
THEORETICAL CUTOFF	30	30
A) 10% ABOVE CUTOFF	33	33
5	66	66
6	132	132
7	264	264
8	528	528

(b)

FLOW FIELD/RUN	PRESSURE RATIO	TEMPERATURE RATIO
THEORETICAL CUTOFF	60	10
B) 10% ABOVE CUTOFF	66	11
9	132	11
10	264	11
11	528	11

(c)

TABLE 3

It was also desired to study ignition behavior in another portion of the admissible region of Fig. 15. For this purpose a new point on the 1000°K cutoff curve was chosen as a starting point for another series of runs. The initial conditions at this cutoff point were

$$\frac{P_a}{P_o} = 60 \quad ; \quad \frac{T_a}{T_o} = 10$$

As before these values were increased by ten percent to yield a better starting point for numerical integration. Thus,

$$\frac{P_a}{P_o} = 66 \quad ; \quad \frac{T_a}{T_o} = 11$$

Then with this new set of initial conditions as a starting point, three more bursting sphere runs were made in which the pressure ratio was successively doubled while the temperature ratio was held constant. These runs are also shown in Table 3c.

As was done for the Huang and Chou 200 atm case in Fig. 11, the values of ψ_{CLOUD} vs. cell number are plotted for runs 1 through 11 in Figs. 16, 17, and 18. Two things can be observed in Figs. 16, 17 and 18. First for a given set of runs, the maximum value of ψ_{CLOUD} increases as the run number increases. Then since the initial pressure ratio increases as the run number increases, we conclude that the maximum value of ψ_{CLOUD} increases as the initial pressure ratio increases.

We would now like to relate this pressure dependence of the maximum value of ψ_{CLOUD} to an energy dependence. This can be done with the following derivation. Let the quantity $P_a/P_o = x$. Then we may write

$$P_a = P_c\, x$$

and we derive:

$$P_a - P_o = P_o x - P_o = P_o(x-1)$$

But $x = \frac{P_2}{P_o}$

So

$$P_a - P_o = P_o\left(\frac{P_a}{P_o} - 1\right) \tag{33}$$

Thus we can see that an increase in the initial pressure ratio yields a monotonic increase in the expression $P_2 - P_o$. Now from eqn. 4 we know that the initial sphere energy, E_1 is directly proportional to the quantity $P_2 - P_o$. Thus we may finally conclude that the maximum value of ψ_{CLOUD} increases as the initial sphere energy increases. This is a logical conclusion because it has been shown that a large value of ψ_{CLOUD} yields a small value of t_o and hence small values of dimensional delay time. Thus we see that as the energy E_1 increases, the value of the maximum ψ_{CLOUD} will increase and corresponding to this, the dimensional delay times will decrease. This is exactly what one would expect. It should be noted however that there may be slight perturbations on this general trend due to the non-steady and non-ideal nature of the flow fields under consideration.

It is interesting to note that the quantity $(P_2/P_o - 1)$ in eqn. 33 has been studied previously by Strehlow and Rieker[7] and Adamczyk[14]. This quantity is called the dimensionless energy density for the bursting sphere and is given the symbol q. Thus

$$q = \frac{P_a}{P_o} - 1 \tag{34}$$

The quantity q represents the amount of energy added to the sphere E_1 normalized by the amount of energy that would have been in an equivalent volume but unpressurized sphere. From eqn. 4, E_1 is given by,

$$E_1 = \frac{4\pi}{3}\,\frac{P_a - P_o}{\gamma_1 - 1}\,r_o^3$$

$$= \frac{P_a - P_o}{\gamma_1 - 1}\,V_{o\,source}$$

The energy for the equivalent volume, unpressurized sphere will be given by the quantity $P_o V_o/(\gamma_1 - 1)$. Then we have

$$q = \frac{E_1}{P_o V_{o\,source}/(\gamma_1 - 1)} = \frac{P_2 - P_o}{\gamma_1 - 1} V_{o\,source} \frac{\gamma_1 - 1}{P_o V_{o\,source}}$$

or

$$q = \frac{P_2 - P_o}{P_o}$$

or

$$q = \frac{P_2}{P_o} - 1$$

The quantity q will be used later in this investigation when delay times and minimum energy requirements for ignition are studied, because it has a closer physical relation to the energy than does the actual initial sphere pressure ratio.

The second noteworthy fact, in regard to Figs. 16, 17 and 18, is that the cell which has the largest value of ψ_{CLOUD} can not be determined prior to the actual numerical integration. This is because the cell for maximum ψ_{CLOUD} is a very complicated function of the flow field variables, which are themselves complicated functions of the initial bursting sphere conditions. From eqn. 21 one may note that for a given cell in a given run,

$$\psi_{CLOUD} = \sum_{t_s/t_o}^{t/t_o} \frac{\left(e^{-\frac{1}{E}}\right)^{68.3498}}{\left(\frac{V}{V_o}\right)} \qquad (35)$$

Thus ψ_{CLOUD} is a complicated function of the time histories of the dimensionless cell energies and specific volumes.

One can however state that the maximum value of ψ_{CLOUD} does not in general occur at or around the contact surface (cells 50 and 51). For runs 1, 2 and 5 the cell which has the largest value of ψ_{CLOUD} is cell 51 which is adjacent to the contact surface. What is probably happening in these runs is that as one progresses out from the contact surface, the cell energy E decays rapidly. Then the term

$$\left(e^{-\frac{1}{E}}\right)^{68.3898} = \left(e^{68.3898}\right)^{-\frac{1}{E}}$$

$$= \frac{1}{\left(e^{68.3898}\right)^{1/E}}$$

gets very small and results in a small value of ψ_{CLOUD}. This behavior is not evident for other, higher initial energy runs.

Finally in regard to Figs. 16, 17 and 18 one fact must be noted. For a few of the cells in runs 7 and 8 the numerical integration could not proceed to completion. This was due to the fact that in these runs the cell energies became so high that the temperatures did not decay below the 1000°K cutoff value by the time the CLOUD program reached the limits of its array dimensions. For some analyses, this would not lead to large errors because as was evident from Fig. 10, cells attain most of their final values of ψ_{CLOUD} very rapidly. The temperature decay portion of the flow field is seen to contribute only a small amount to ψ_{CLOUD}. However for the delay time and minimum ignition energy analysis discussed later the above incomplete numerical integration could lead to some erroneous results. This will be discussed in more detail later.

Further data reduction was undertaken for runs 1 through 4. Tables 4, 5, 6 and 7 show data for these runs as was shown for the Huang and Chou 200 atm case in Table 2. These results are then plotted in Figs. 19, 20, 21 and 22 as was also done for the Huang and Chou case.

Figs. 19, 20, 21 and 22 show an interesting range of delay time behavior. For runs 1 and 2, Figs. 19 and 20 show only half-curves. This is of course due to the fact that in these runs the cells which had the largest values of ψ_{CLOUD} were adjacent to the contact surface. In Fig. 19 it can also be seen that cell 51, adjacent to the contact surface, ignites at virtually

TABLE 4

CELL	$\psi_{CLOUD} = 1.726 \times 10^{5}$ sec^{-1} $t_o = 5.793 \times 10^{-6}$ sec $r_o = 1.694 \times 10^{-1}$ cm $E_1 = 3.353 \times 10^{-1}$ joules		$\psi_{CLOUD} = 1.286 \times 10^{5}$ sec^{-1} $t_o = 7.776 \times 10^{-6}$ sec $r_o = 2.274 \times 10^{-1}$ cm $E_1 = 8.109 \times 10^{-1}$ joules		$\psi_{CLOUD} = 1.179 \times 10^{5}$ sec^{-1} $t_o = 8.482 \times 10^{-6}$ sec $r_o = 2.480 \times 10^{-1}$ cm $E_1 = 1.052 \times 10^{0}$ joules	
	$t/t_o)_{\psi=1}$	t_{DELAY} (sec)	$t/t_o)_{\psi=1}$	t_{DELAY} (sec)	$t/t_o)_{\psi=1}$	t_{DELAY} (sec)
51	.295	1.709×10^{-6}	.120	9.331×10^{-7}	.110	9.330×10^{-7}
52	∞	∞	.170	1.322×10^{-6}	.145	1.230×10^{-6}
53	∞	∞	.265	2.061×10^{-6}	.185	1.569×10^{-6}
54	∞	∞	∞	∞	.265	2.248×10^{-6}

RUN #1

TABLE 5

C E L L	ψ_{CLOUD}= 8.964x10^{5} sec^{-1} t_o = 1.116x10^{-6} sec r_o = 3.262x10^{-2} cm E_1 = 4.826x10^{-3} joules		ψ_{CLOUD}=7.698x10^{5} sec^{-1} t_o = 1.299x10^{-6} sec r_o = 3.799x10^{-2} cm E_1 = 7.619x10^{-3} joules		ψ_{CLOUD}= 6.439x10^{5} sec^{-1} t_o = 1.553x10^{-6} sec r_o = 4.542x10^{-2} cm E_1 = 1.302x10^{-2} joules	
	$t/t_o)_{\psi=1}$	t_{DELAY}(sec)	$t/t_o)_{\psi=1}$	t_{DELAY} (sec)	$t/t_o)_{\psi=1}$	t_{DELAY} (sec)
51	.485	5.413x10^{-7}	.200	2.598x10^{-7}	.145	2.252x10^{-7}
52	∞	∞	.255	3.312x10^{-7}	.150	2.330x10^{-7}
53	∞	∞	.295	3.832x10^{-7}	.170	2.640x10^{-7}
54	∞	∞	.315	4.092x10^{-7}	.180	2.795x10^{-7}
55	∞	∞	.475	6.170x10^{-7}	.195	3.028x10^{-7}
56	∞	∞	∞	∞	.205	3.184x10^{-7}
57	∞	∞	∞	∞	.225	3.494x10^{-7}
58	∞	∞	∞	∞	.260	4.038x10^{-7}
59	∞	∞	∞	∞	.305	4.737x10^{-7}
60	∞	∞	∞	∞	.475	7.377x10^{-7}

RUN #.

TABLE 6

CELL	$\psi_{CLOUD} = 3.016 \times 10^{6}$ sec^{-1} $t_o = 3.316 \times 10^{-7}$ sec $r_o = 9.696 \times 10^{-3}$ cm $E_1 = 2.544 \times 10^{-4}$ joules		$\psi_{CLOUD} = 2.846 \times 10^{6}$ sec^{-1} $t_o = 3.514 \times 10^{-7}$ sec $r_o = 1.028 \times 10^{-2}$ cm $E_1 = 3.027 \times 10^{-4}$ joules		$\psi_{CLOUD} = 2.725 \times 10^{6}$ sec^{-1} $t_o = 3.670 \times 10^{-7}$ sec $r_o = 1.073 \times 10^{-2}$ cm $E_1 = 3.449 \times 10^{-4}$ joules	
	$t/t_o)_{\psi=1}$	t_{DELAY} (sec)	$t/t_o)_{\psi=1}$	t_{DELAY} (sec)	$t/t_o)_{\psi=1}$	t_{DELAY} (sec)
53	∞	∞	.745	2.618×10^{-7}	.345	1.266×10^{-7}
54	∞	∞	.375	1.318×10^{-7}	.300	1.101×10^{-7}
55	.785	2.603×10^{-7}	.335	1.177×10^{-7}	.275	1.009×10^{-7}
56	∞	∞	.350	1.230×10^{-7}	.290	1.064×10^{-7}
57	∞	∞	.375	1.318×10^{-7}	.305	1.119×10^{-7}
58	∞	∞	.410	1.441×10^{-7}	.325	1.193×10^{-7}
59	∞	∞	∞	∞	.380	1.395×10^{-7}
60	∞	∞	∞	∞	.805	2.954×10^{-7}

Run # 5

TABLE 7

CELL	$\psi_{CLOUD} = 4.367 \times 10^{6}$ sec^{-1} $t_o = 2.290 \times 10^{-7}$ sec $r_o = 6.697 \times 10^{-3}$ cm $E_1 = 1.679 \times 10^{-4}$ joules		$\psi_{CLOUD} = 3.787 \times 10^{6}$ sec^{-1} $t_o = 2.641 \times 10^{-7}$ $r_o = 7.722 \times 10^{-3}$ cm $E_1 = 2.575 \times 10^{-4}$ joules		$\psi_{CLOUD} = 3.724 \times 10^{6}$ sec^{-1} $t_o = 2.685 \times 10^{-7}$ sec $r_o = 7.853 \times 10^{-3}$ cm $E_1 = 2.708 \times 10^{-4}$ joules	
	$t/t_o)_{\psi=1}$	t_{DELAY} (sec)	$t/t_o)_{\psi=1}$	t_{DELAY} (sec)	$t/t_o)_{\psi=1}$	t_{DELAY} (sec)
79	∞	∞	∞	∞	2.365	6.350×10^{-7}
80	∞	∞	.405	1.070×10^{-7}	.385	1.054×10^{-7}
81	∞	∞	.475	1.254×10^{-7}	.450	1.208×10^{-7}
82	∞	∞	.625	1.651×10^{-7}	.535	1.436×10^{-7}
83	1.175	2.691×10^{-7}	.355	9.380×10^{-8}	.335	8.990×10^{-8}
84	∞	∞	.395	1.043×10^{-7}	.375	1.007×10^{-7}
85	∞	∞	.465	1.228×10^{-7}	.430	1.155×10^{-7}
86	∞	∞	.535	1.413×10^{-7}	.485	1.302×10^{-7}
87	∞	∞	1.115	2.945×10^{-7}	.605	1.624×10^{-7}

RUN #4

the same time for two different initial sphere energies. Figs. 20, 21 and 22 show some ripples in the curves which are most likely due to the passage of the secondary wave systems and general non-ideal nature of the flow fields. Fig. 22 especially shows some rather striking behavior around the vicinity of cell 80, where there is a secondary extremum in the curve for each of the two larger energy levels. This type of behavior would be almost, if not impossible to deduce analytically, whereas the numerical procedure shows the results quite well.

To compare these runs with each other in terms of delay time to ignition, Fig. 23 has been obtained. On this graph are plotted the delay times which correspond to the minimum energy for ignition level for each given run. These data are plotted vs. the non-dimensional energy density, q which is used to characterize each run. Runs 1, 2, 3 and 4 which have just been investigated yield points on the curve labelled $T_2/T_0 = 33$. Also shown on this curve is a data point for run A. Included on this plot also are two other curves. The bottom curve corresponds to runs 4, 5 and 6 for which the temperature ratio initially in the bursting sphere equalled the initial pressure ratio. Runs 7 and 8 have not been reduced for delay time data due to the incomplete numerical integration of Ψ_{CLOUD} for these runs. The top curve corresponds to runs B, 9, 10 and 11. In these runs the initial bursting sphere temperature ratio was held constant at a value of $T_2/T_0 = 11$.

Looking at each curve on Fig. 23 alone, it is obvious that the delay time is a function of the initial bursting sphere pressure ratio. However, since a change in the bursting sphere temperature ratio causes a switch to another curve altogether, it is also seen that the delay time is a function of this initial temperature ratio. From observing the relative positions

of the various curves one could conclude that the relation between initial sphere temperature ratio and corresponding delay time is highly non-linear.

The physical reason for the dependence of the delay time on the temperature ratio can be shown as follows. We know that the energy added to the sphere E_1 is a function only of the pressure and not of the sphere temperature. Thus the temperature does not contribute to the bursting sphere energy. Nevertheless the temperature does influence the flow field. At the instant of burst a travelling wave system is set up. The lead shock propagates outward from the contact surface while a rarefaction fan propagates inward toward the center of the sphere. This rarefaction fan, being an isentropic, acoustic wave must propagate at the local sound speed, which with the assumption of a perfect gas is a direct function of the temperature in the bursting sphere. The energy available from the high pressure sphere cannot be utilized to drive the lead shock until the rarefaction fan has passed through and hence released it to the flow field. Thus the rapidity with which this energy is made available to the flow field is dependent on the sound speed in the high pressure gas, which is then in turn related to the temperature or temperature ratio in the initial bursting sphere. Thus changes in the sphere temperature ratio, while not changing the bursting sphere energy, do alter the flow field enough to have a definite effect on the delay times for various runs.

To provide a qualitative picture of the ignition behavior in the flow field of a bursting sphere explosion loci have been plotted for runs 1, 2 and 3. These are shown in Figs. 24, 25, 26, 27, 28, and 29. For each run, the entire flow field is depicted first, with the area of interest for ignition studies blocked off. This blocked off area is then magnified to provide a clearer view of the detailed behavior being studied. Explosion

loci for the two higher values of E_1 for each run are plotted in the magnified graphs.

In Figs. 24, 26 and 28 note the increasing strength of the lead shock as the run number and hence initial sphere pressure ratio increases. This vividly illustrates the changing flow field which results when initial sphere conditions are varied. Secondary shocks are also visible on Figs. 26 and 28 for cases 2 and 3.

In the magnified plots, Figs. 25, 27 and 29 it should first be noted that the rather irregular termination of the particle paths in the upper right parts of the graphs is not physically realistic but results from plotter limitations. Figs. 25 and 27 again show only one half of the explosion loci. As before this is due to the fact that the runs for these plots have their maximum value of ψ_{CLOUD} for the cell adjacent to the contact surface. Fig. 29 for run 3 shows the full expected explosion loci.

It is interesting to note that the explosion loci are nearly parallel to the actual particle trajectories for these runs. In other words, each cell has a distinct non-dimensional time at which it will ignite. One might have expected the explosion loci to lie horizontally. If this were the case then it would imply that a number of cells would ignite simultaneously. However, this type of behavior has not been observed for flow fields studied in this investigation.

Finally we would like to study the minimum energy for ignition behavior for the bursting sphere cases. Recall for the Huang and Chou 200 atm case that there was one value of E_1 for which only one cell in the flow field, that one with the largest value of ψ_{CLOUD}, would ignite. This was called the minimum energy for ignition as energy less than this amount would cause all cells to have an infinite delay time. A corresponding energy level can

also be found for all the bursting sphere runs presented. This has been done and the results plotted in Fig. 30. On this graph the minimum sphere energy for ignition, E_1 is plotted as a function of the non-dimensional energy density, q.

It can be seen that Fig. 30 bears a striking resemblance to Fig. 23, the delay time plot for the combined bursting sphere runs. On Fig. 30, the curves for initial temperature ratio equal to 33, initial temperature ratio equal to 11, and initial temperature ratio equal to initial pressure ratio are drawn. Moreover, the curves occupy the same relative positions as those drawn on Fig. 23. It is not surprising that the two figures are similar because the delay time and the bursting sphere energy are intimately related, as has been discussed previously. There is one important difference between the two figures however. Fig. 23 shows that the delay times for the runs under investigation span about two orders of magnitude. On the other hand, Fig. 30 indicates that the minimum energies for ignition for the same runs span about seven orders of magnitude. Thus the minimum ignition energy is a much stronger function of the energy density than the delay time.

All three of the curves on Fig. 30 show the expected behavior, i.e., as the energy density increases, the minimum energy for ignition decreases. Note that as one approaches the cutoff energy density, which is analogous to approaching the 1000°K curve on Fig. 15, the required energy increases extremely rapidly, eventually reaching an infinite value when one encounters the Fig. 15 cutoff curve. On the other hand it is seen that as one approaches very large energy densities, very little change in the minimum bursting sphere energy is required to produce an ignition.

As in the Fig. 23 delay time plot, runs 7 and 8 are not shown on the temperature ratio equal to pressure ratio curve, because the incomplete numerical integration would yield erroneous data. Nevertheless, the sound

speed effects are evident in this curve and in the curve of temperature ratio equal to 11. The same reasoning discussed earlier applies. That is, as the initial sphere temperature ratio increases, so does the sphere sound speed. This enables the inward moving rarefaction fan to release the sphere energy to the flow field more quickly and from a minimum ignition energy standpoint more efficiently.

In summary, it should be noted that a bursting sphere may be characterized by an instantaneous addition of the energy E_1. This is because at time zero plus all of the energy which is ever going to be present is already present. We now wish to investigate a number of flow fields in which a finite amount of time is required to add the energy E_1 to the high pressure source region.

VI. ENERGY ADDITION RESULTS

To determine the effects of finite rate energy deposition times on ignition behavior in the computer generated flow field, a number of computer runs were made with a non-dimensional deposition time of $t/t_0 = .02$. In addition one run was made with a non-dimensional deposition time of $t/t_0 = .01$. This case will be discussed last. The mechanics of how this energy is added with a finite rate in the CLOUD program is discussed in Adamczyk.[14]

To obtain a certain consistency between the finite rate energy addition flow fields and those generated by a bursting sphere, it was decided to force the pressure and temperature ratios in the source regions of the energy addition runs at the instant the addition was completed to be equal to the initial pressure and temperature ratios in the source regions of the corresponding bursting spheres. Thus we have at the instant the deposition is completed the same temperature ratios and hence the same sound speed effects

as were encountered for the bursting sphere case. We must note two things however. First, since the wave system begins propagating at non-dimensional time $t/t_o = 0+$, by the time the deposition is complete, the source region is not completely homogeneous. Nevertheless the inner portion of the source region is homogeneous since the inward travelling wave does not reach this area until after the deposition is completed. Second, the addition is assumed to occur at constant volume. Again because of the wave system, this is not strictly true but as the change in volume during this time interval is small, the effect is ignored.

To yield the proper conditions at $t/t_o = .02$, we must have the proper initial conditions for the energy addition runs. This is determined as follows. Recall the bursting sphere energy is given by,

$$E_3 = \frac{4\pi}{3}\frac{P_2 - P_0}{\gamma_1 - 1} r_0^3$$

$$= \frac{P_2 - P_0}{\gamma_1 - 1} V_{0\,\text{SOURCE}}$$

In terms of intensive variables this may be re-written,

$$\frac{E_3}{m} = \frac{P_2 - P_0}{\gamma_1 - 1}\frac{V_{0\,\text{SOURCE}}}{m}$$

$$= \frac{P_2 - P_0}{\gamma_1 - 1} V_{\substack{\text{SOURCE} \\ \text{BURSTING SPHERE}}} \qquad (36)$$

where m represents the mass in the source region. Adamczyk[14] then defines a new variable Q_f which is the energy input term for the finite rate deposition CLOUD runs. Q_f is then given by the expression,

$$Q_f = \frac{E_3/m}{P_0 v_0}$$

$$= \frac{P_2 - P_0}{P_0}\frac{1}{\gamma_1 - 1}\left(\frac{v}{v_0}\right)_{\substack{\text{SOURCE} \\ \text{BURSTING SPHERE}}}$$

$$= \frac{q}{\gamma_1 - 1}\left(\frac{v}{v_0}\right)_{\substack{\text{SOURCE} \\ \text{BURSTING SPHERE}}} \qquad (37)$$

Q_f is then used to characterize the energy input for the CLOUD program where the values of γ_1 and $(v/v_0)_{\substack{\text{SOURCE} \\ \text{BURSTING SPHERE}}}$ are those values obtained for the corresponding bursting sphere case.

It remains to determine the initial pressure and temperature ratios for the energy addition cases. For all of these runs the initial pressure ratio was taken to be unity i.e., ambient pressure. However, the initial temperature ratio is not necessarily equal to unity. We can solve for the initial temperature ratio in the following manner. Since we are assuming a constant volume energy addition, we may write:

$$\left(\frac{V}{V_0}\right)_{\substack{\text{SOURCE}\\ \text{ENERGY ADDITION}}} = \left(\frac{V}{V_0}\right)_{\substack{\text{SOURCE}\\ \text{BURSTING SPHERE}}}$$

Then from the perfect gas law,

$$\left(\frac{V}{V_0}\right)_{\substack{\text{SOURCE}\\ \text{ENERGY ADDITION}}} = \frac{(T_a/T_0)_{\text{ENERGY ADDITION}}}{(P_a/P_0)_{\text{ENERGY ADDITION}}}$$

and

$$\left(\frac{V}{V_0}\right)_{\substack{\text{SOURCE}\\ \text{BURSTING SPHERE}}} = \frac{(T_a/T_0)_{\text{BURSTING SPHERE}}}{(P_a/P_0)_{\text{BURSTING SPHERE}}}$$

where $R_{\text{ENERGY ADDITION}} = R_{\text{BURSTING SPHERE}} = R_0$ and thus the gas constant drops out of the above expressions. Then,

$$\frac{(T_a/T_0)_{\text{ENERGY ADDITION}}}{(P_a/P_0)_{\text{ENERGY ADDITION}}} = \frac{(T_a/T_0)_{\text{BURSTING SPHERE}}}{(P_a/P_0)_{\text{BURSTING SPHERE}}}$$

or

$$\left(\frac{T_a}{T_0}\right)_{\text{ENERGY ADDITION}} = \left(\frac{T_a}{T_0}\right)_{\text{BURSTING SPHERE}} \frac{(P_a/P_0)_{\text{ENERGY ADDITION}}}{(P_a/P_0)_{\text{BURSTING SPHERE}}}$$

or since $(P_a/P_0)_{\text{ENERGY ADDITION}} = 1$ from above, we have

$$\left(\frac{T_a}{T_0}\right)_{\text{ENERGY ADDITION}} = \frac{(T_a/T_0)_{\text{BURSTING SPHERE}}}{(P_a/P_0)_{\text{BURSTING SPHERE}}} \tag{38}$$

Then using eqns. 37 and 38, eight energy addition runs were made. These runs are displayed in Table 8. For each of these runs, the computer output was checked to verify that the proper conditions were obtained at the instant the deposition was completed. In all cases, verification was obtained.

TABLE 3

FLOW FIELD RUN	CORRESPONDING BURSTING SPHERE RUN	PRESSURE RATIO	TEMPERATURE RATIO	Q_f
12	1	1	.5	81.25
13	2	1	.25	81.875
14	3	1	.125	82.1875
15	4	1	.0625	82.34375
16	5	1	1	162.5
17	6	1	1	327.5
18	7	1	1	657.5
19	8	1	1	1317.5
20 *	1	1	.5	81.25

*Run 20 has deposition time, $t/t_o = .01$

All other runs have deposition times, $t/t_o = .02$

The plots of ψ_{CLOUD} vs. cell number, t_{DELAY} vs. cell number and explosion loci are not shown for the energy addition runs as they are qualitatively similar to their bursting sphere counterparts. However, it has been worthwhile to display the minimum energy for ignition data for the energy addition runs. This has been done in Fig. 31. On this graph the minimum energy required for ignition for a given energy addition run has been plotted vs. the non-dimensional energy density, q of the corresponding bursting sphere run. Also shown on this graph for the sake of comparison are the corresponding bursting sphere curves, taken from Fig. 30. As before, data for runs 18 and 19 are not shown because of incomplete numerical integrations for these runs.

It can be seen on Fig. 31 that for most of the range of q, the minimum energy required to obtain an ignition in an energy addition flow field is less than the amount required in a corresponding bursting sphere flow field. A qualitative explanation of this behavior depends on two observations. First, in the bursting sphere case the initial compression wave is a shock.

In the energy addition case, the initial compression wave is an acoustic wave and builds up to a shock as the energy is being deposited in the source region. As it is known that an acoustic wave will do more compressive work than a shock wave, we may conclude that the lead wave in the energy addition case will have higher pressures and temperatures in its wake than will the corresponding lead wave in the bursting sphere case. This is conducive to larger values of ψ_{CLOUD} and hence smaller values of minimum ignition energy for the energy addition cases. Second,[15] because of the time-dependent nature of the deposition in the energy addition cases, the resulting lead wave may "focus" certain particles of the flow field to produce local hot spots. This will then also lead to larger values of ψ_{CLOUD} and smaller values of minimum ignition energy.

At the far left of Fig. 31, where the values of q are small, the energy addition curves are seen to merge into the bursting sphere curves. What is happening here is that at these low energy densities, ignition becomes hard to produce as we are approaching the critical cutoff curve of Fig. 15. Thus both the energy addition and bursting sphere curves approach a vertical asymptote and because of this are seen to merge into each other. It should also be noted that at q = 500 the bursting sphere curve, for the temperature ratio equal to 33 is seen to intersect its corresponding energy addition curve. It is believed that this is caused by an incomplete numerical integration in run 15 and thus not representative of true physical behavior. However, this has not been confirmed at the time of this writing.

Finally, we may examine one further phenomenon. We can define a new variable p, called the power density by the following relation.

$$p = \left(\frac{P_a}{P_0} - 1\right) \Big/ \left(\frac{t}{t_0}\right)_{DEPOSITION}$$

or

$$p = q \Big/ \left(\frac{t}{t_o}\right)_{DEPOSITION} \tag{39}$$

where q has been defined previously and $(t/t_o)_{DEPOSITION}$ represents the non-dimensional energy deposition time. We may look at bursting sphere run 1 and energy addition runs 12 and 20. For each of these case, q = 65. Run 12 has a deposition time of $t/t_o = .02$ whereas run 20 has a deposition time of $t/t_o = .01$. Because run 1 is a bursting sphere it is known to have a deposition time $t/t_o = 0$. For these cases then the power densities have been determined from eqn. 39. The inverses of these power densities have also been determined. These data are shown in Table 9.

TABLE 9

FLOW FIELD RUN	$q = \frac{p_2}{p_o} - 1$	$\left(\frac{t}{t_o}\right)_{DEPOSITION}$	$p = \frac{q}{(t/t_o)_{DEPOSITION}}$	$\frac{1}{p}$
1	65	0	∞	0
12	65	.0.	6500	1.538×10^{-4}
20	65	.01	3250	3.077×10^{-4}

Fig. 32 is a plot of the minimum energy required for ignition vs. the quantity 1/p for the above three cases. The data points are connected by straight dashed lines to indicate that the exact shape of the curve is not known at this time. However, from the three data points plotted, we can say that the curve appears to exhibit relative extremum behavior. This suggests that there may possibly be optimal power densities for ignition. This has not been investigated further at the time of writing.

VII CONCLUSIONS

We have seen that the ignition behavior in a non-steady, non-ideal flow field is a complicated function of the flow variables, particularly cell energy or temperature and cell specific volume. These quantities are

themselves complicated functions of the initial conditions in the source region.

We have also seen that the important quantities to determine are the delay times to ignition and the minimum energies required for ignition, and that both of these quantities tend to decrease as the non-dimensional energy density increases.

We have also studied the differences in ignition behavior as the source was changed from a bursting sphere to a finite-rate energy deposition source, and found that for most values of q, the finite rate energy addition cases required a smaller amount of dimensional energy E_1 to produce an ignition in the flow field.

Finally we have briefly examined the effects of power density on minimum energy required for ignition and shown that there may be optimal power densities to produce an ignition.

VIII. SUGGESTIONS FOR FUTURE RESEARCH

A number of variables have been held constant during this investigation. These could be varied to yield additional data. For example one could change the temperature cutoff limit from 1000°K to 1200 °K to see what effect it has on the ignition behavior in the resulting flow fields. One could also substitute the values for the activation energy and pre-exponential factor from the Schott and Kinsey data for the values obtained from Strehlow. One could also use source regions which contain for example helium ($\gamma_1 = 1.667$). In addition it would be instructive to obtain more data points for Fig. 32 at different power densities.

There are three limitations of the model used in this investigation which might be removed in future work. First, a more detailed reaction

kinetics scheme could be incorporated. Second, when a particle ignites, it then adds heat to the neighboring particles, thus altering the flow field. This heat addition could also be included in the model. Third, the combustible mixture, which was assumed to have the properties of air in this investigation could be replaced by a more realistic combustible mixture.

Finally, the point source solution for spherical blast waves could be used as a means of establishing a flow field for ignition behavior studies. As the point source solution provides an ideal flow field it would contrast nicely with the non-ideal bursting sphere and energy addition flow fields studied in this report.

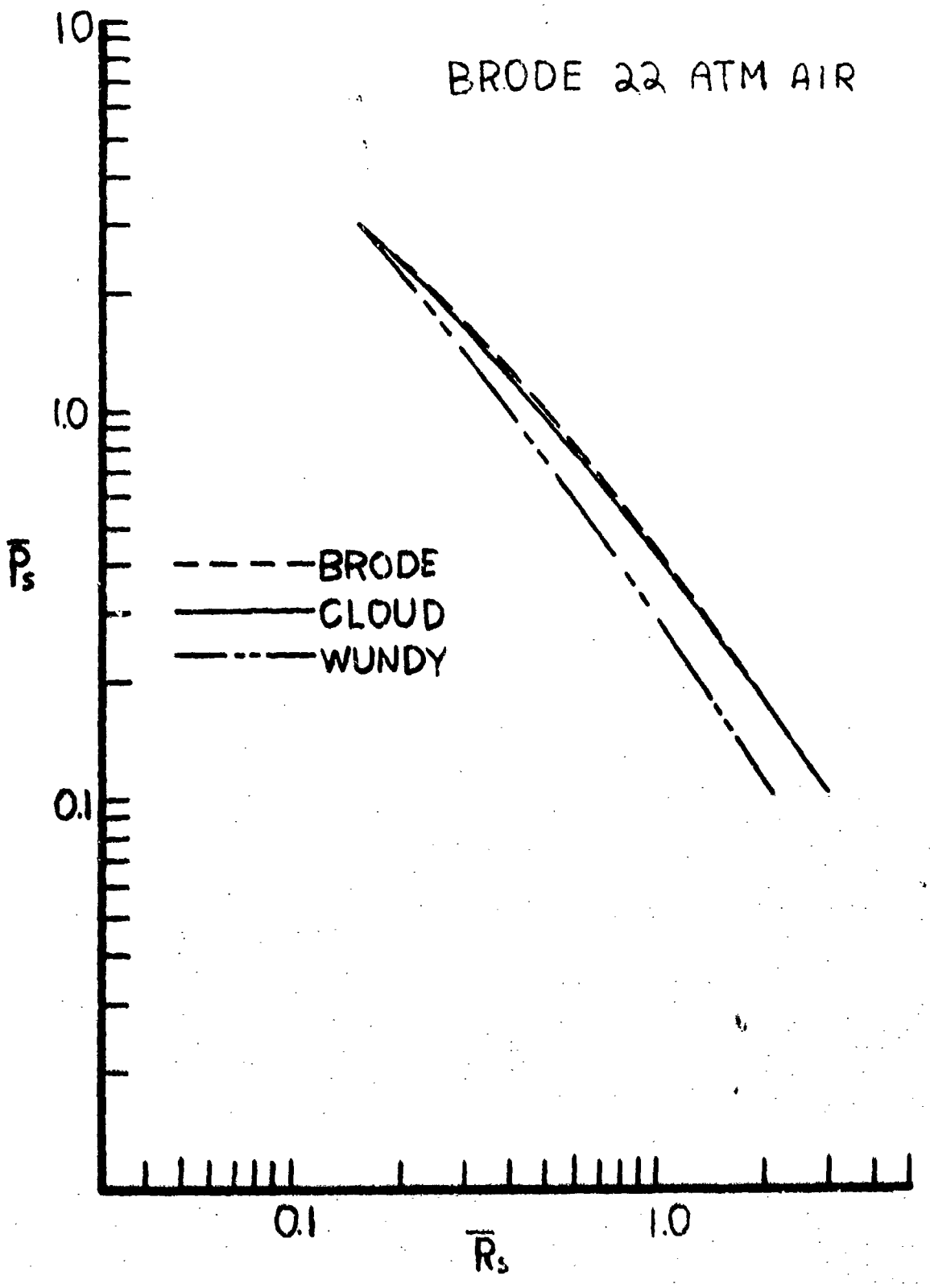

FIGURE 1:Shock Overpressure vs. Energy Scaled Radius

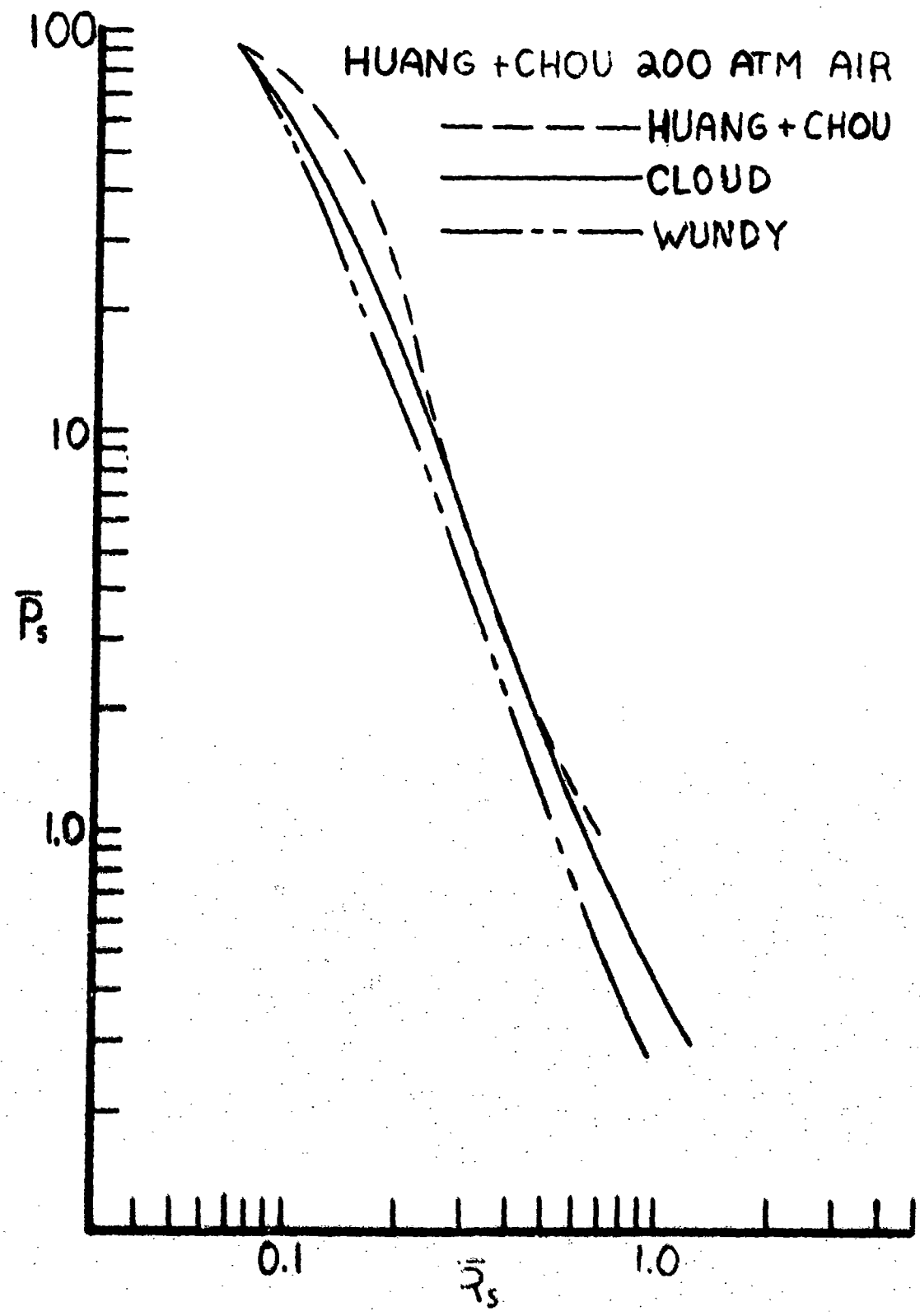

FIGURE 2:Shock Overpressure vs. Energy Scaled Radius

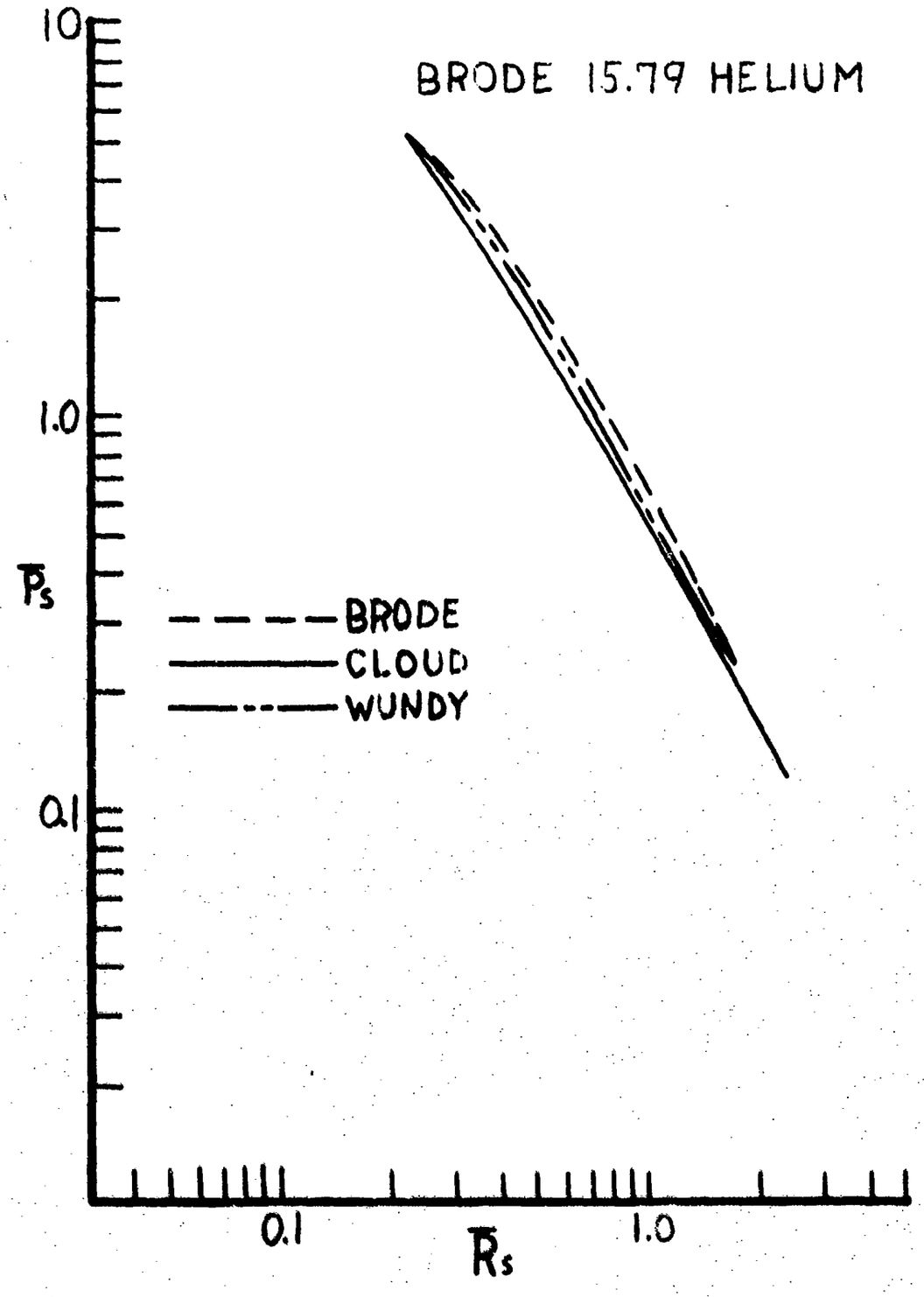

FIGURE 5:Shock Overpressure vs. Energy Scaled Radius

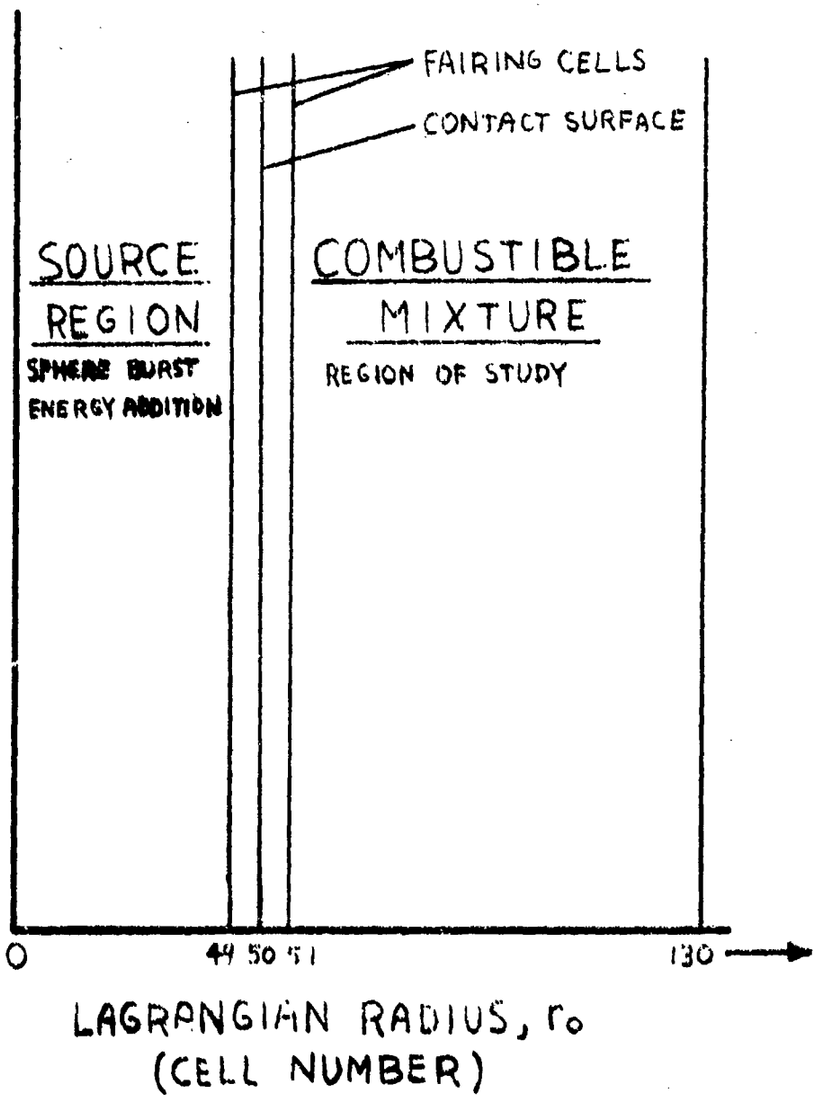

FIGURE 4:Generalized Flow Field

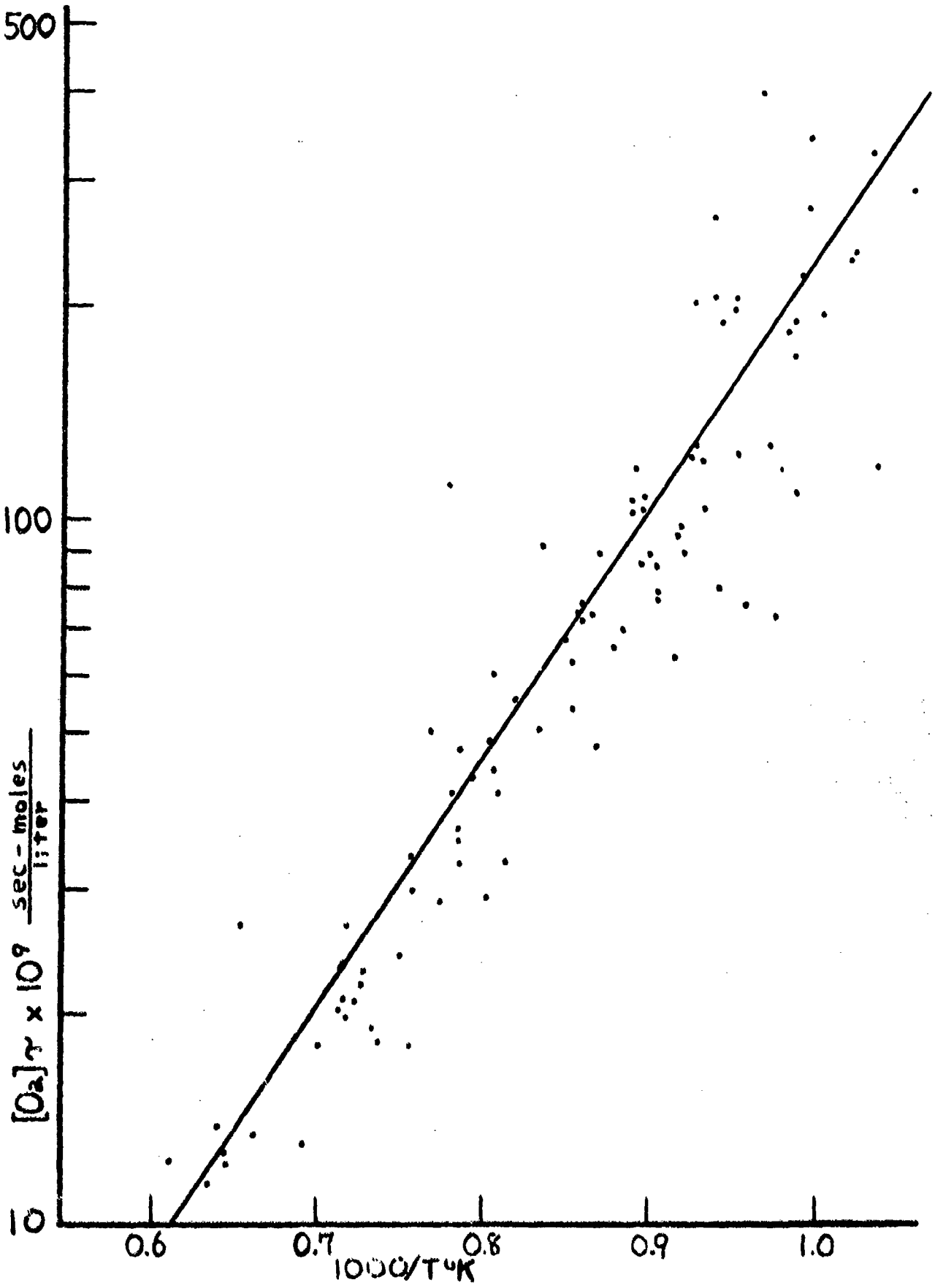

FIGURE 5:Reaction Kinetics (from Strehlow)

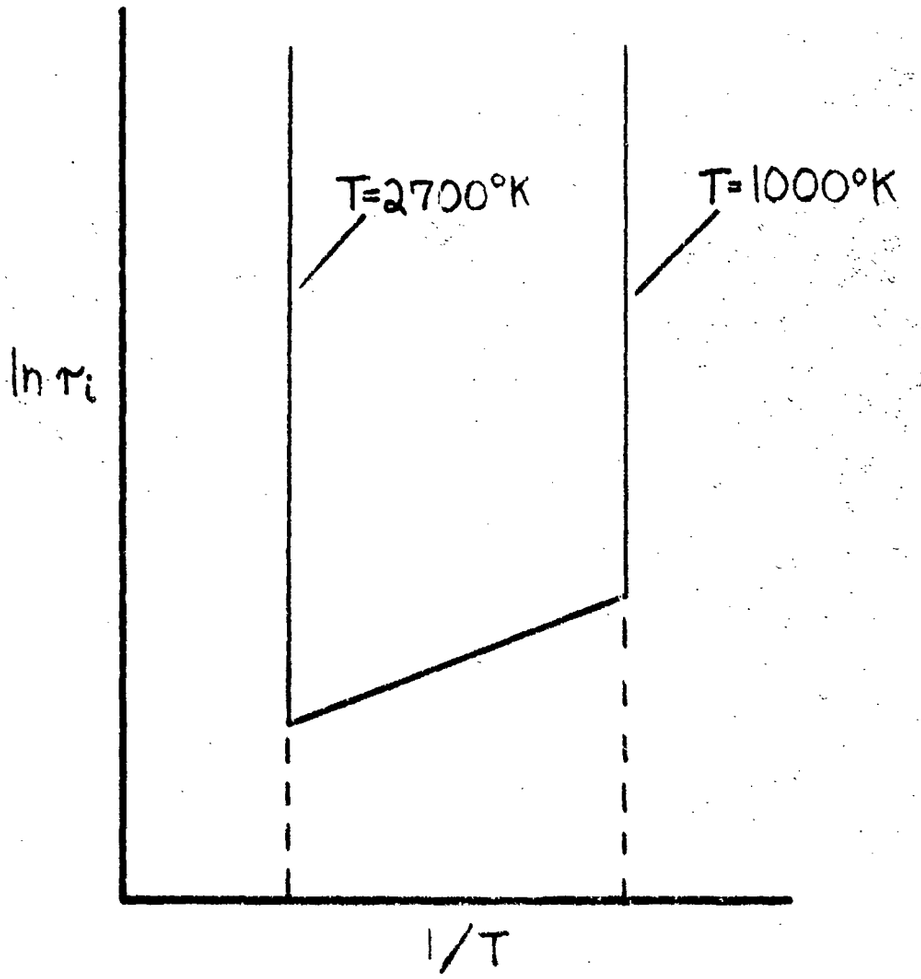

FIGURE 6:Arrhenius Kinetics Temperature Limits

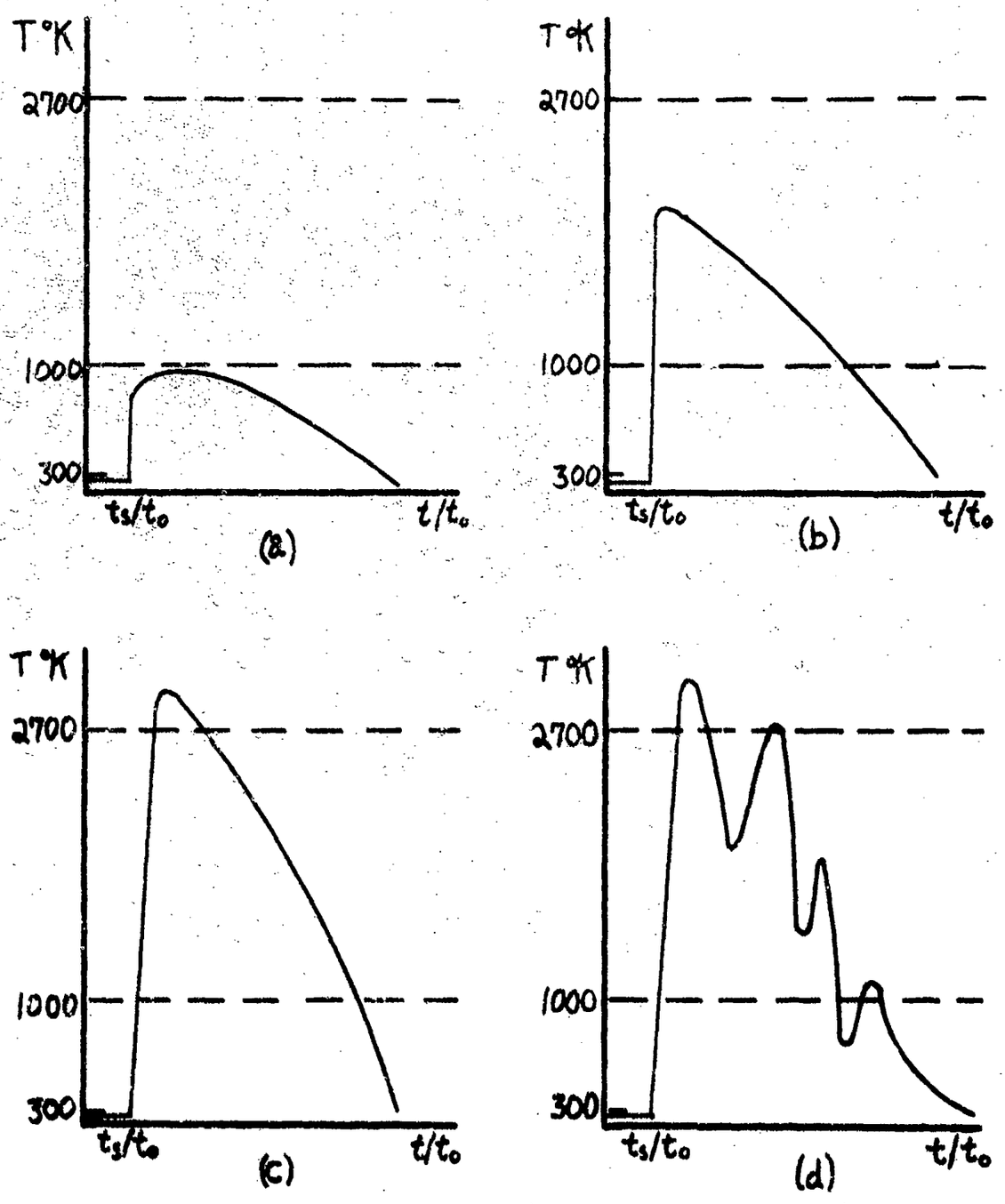

FIGURE 7:Temperature-Time Profiles

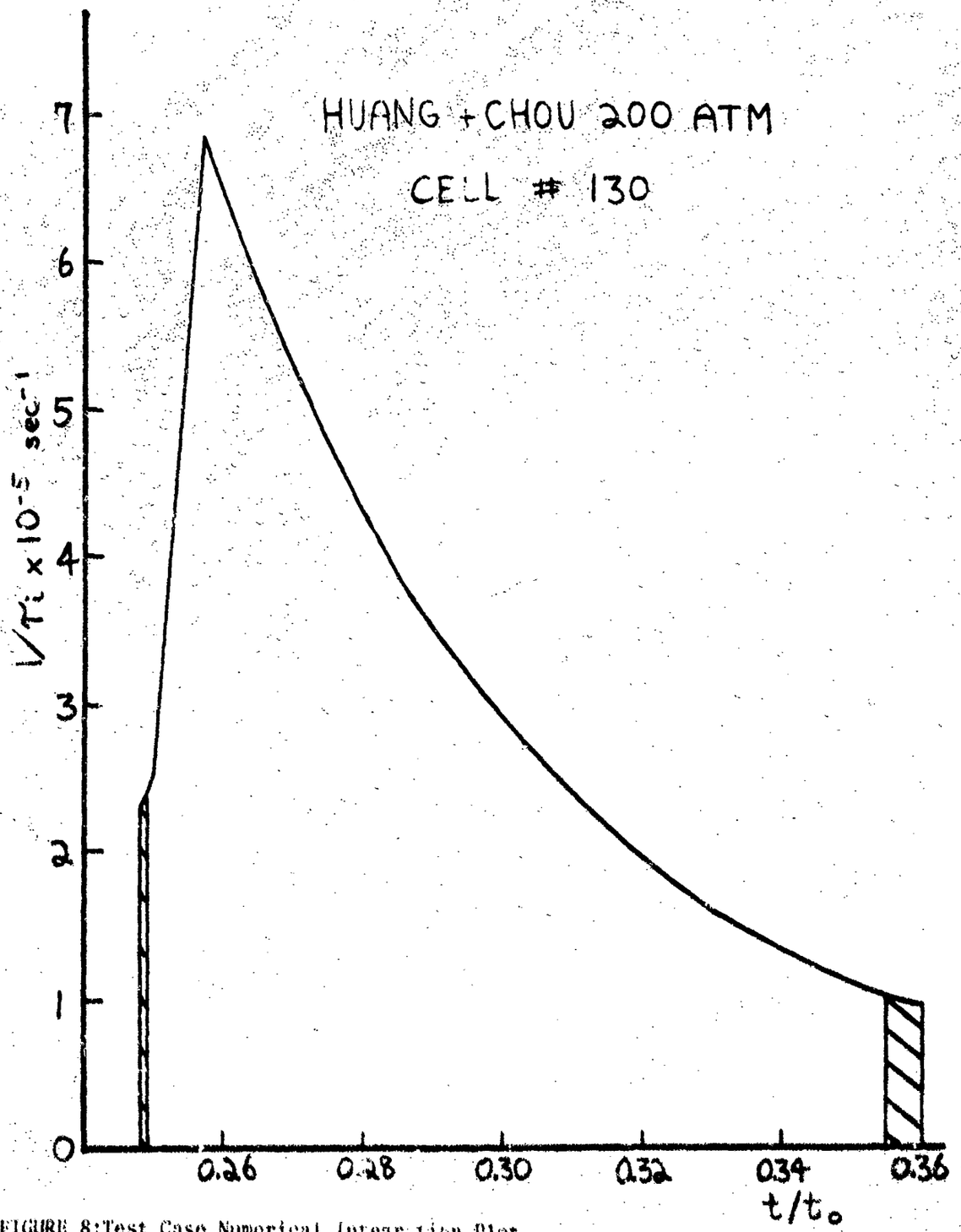

FIGURE 8:Test Case Numerical Integration Plot

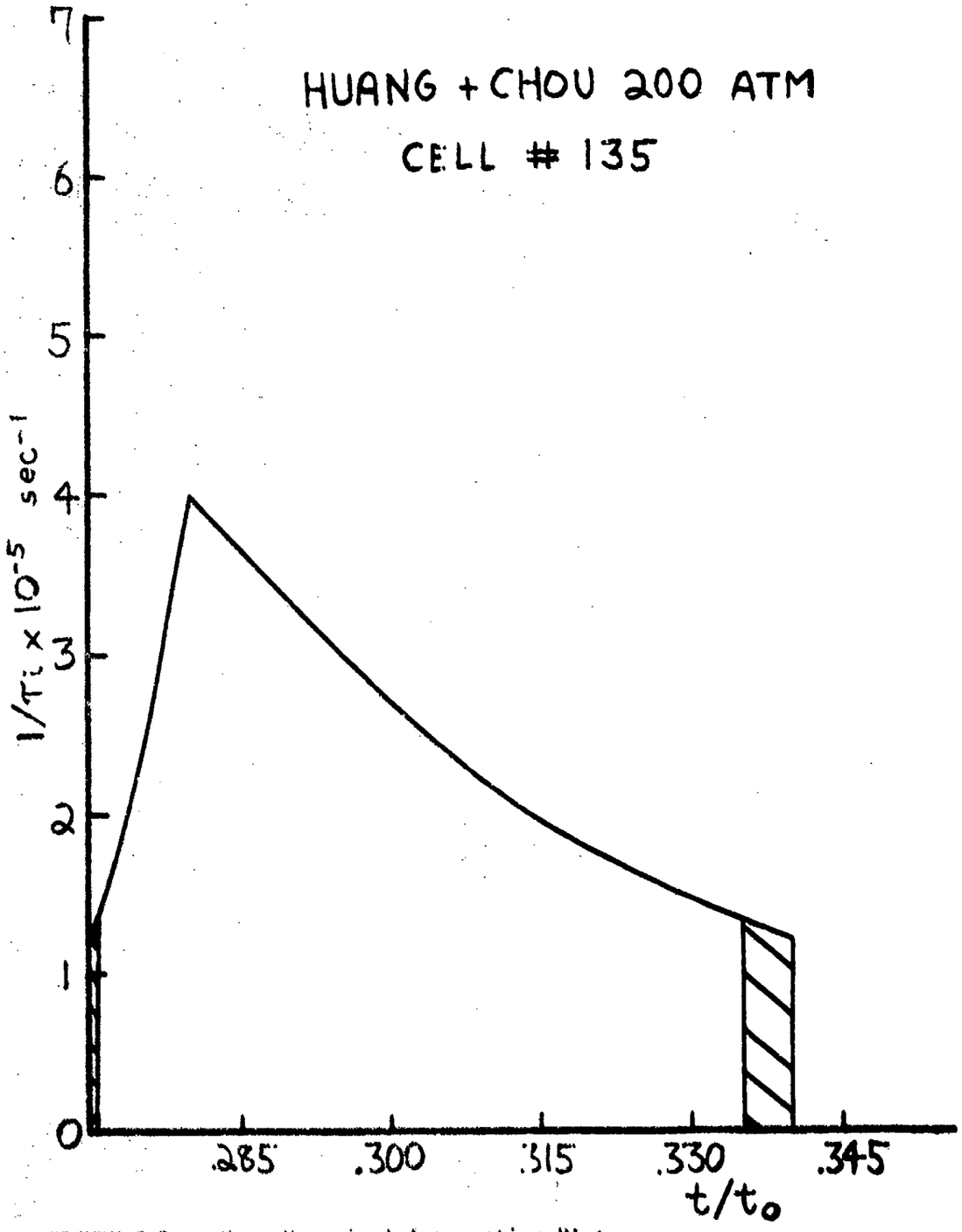

FIGURE 9:Test Case Numerical Integration Plot

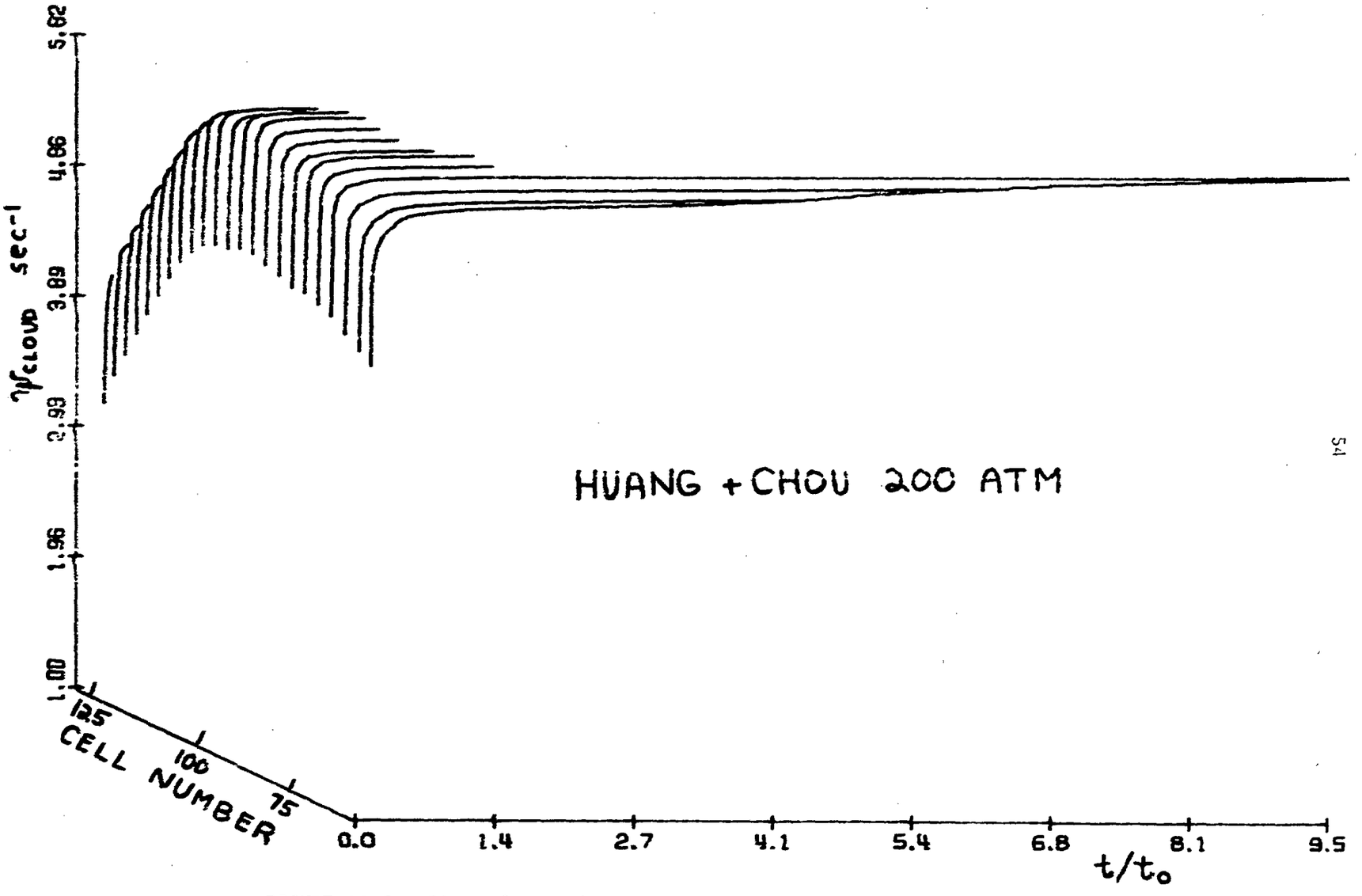

FIGURE 10:3-D Plot of Numerical Integration

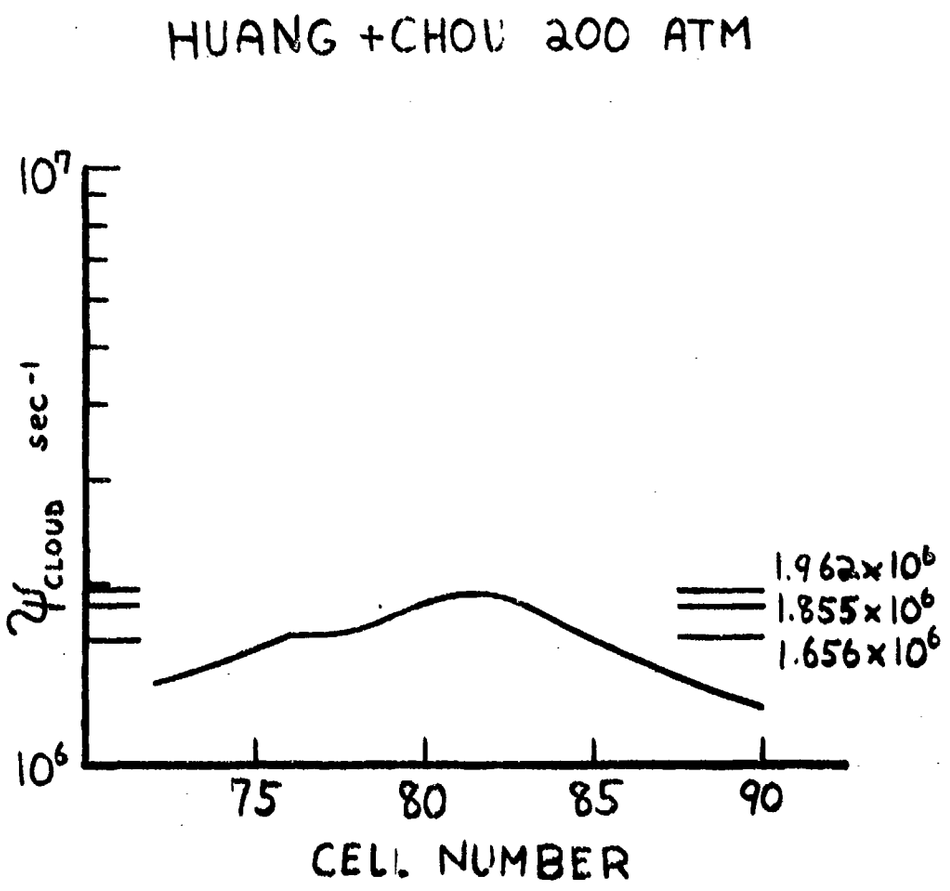

FIGURE 11: ψ_{CLOUD} vs. Cell Number, Huang and Chou

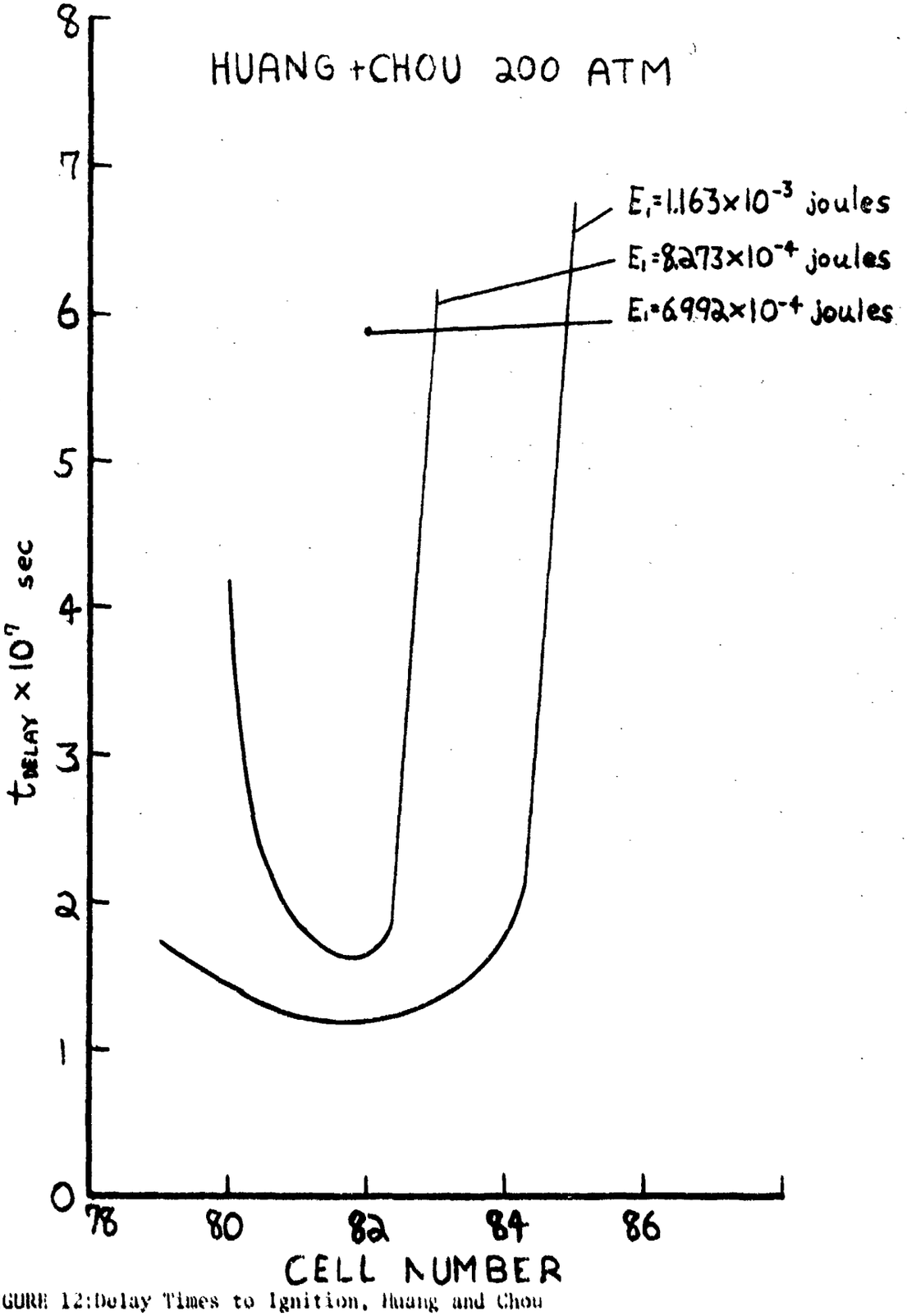

FIGURE 12: Delay Times to Ignition, Huang and Chou

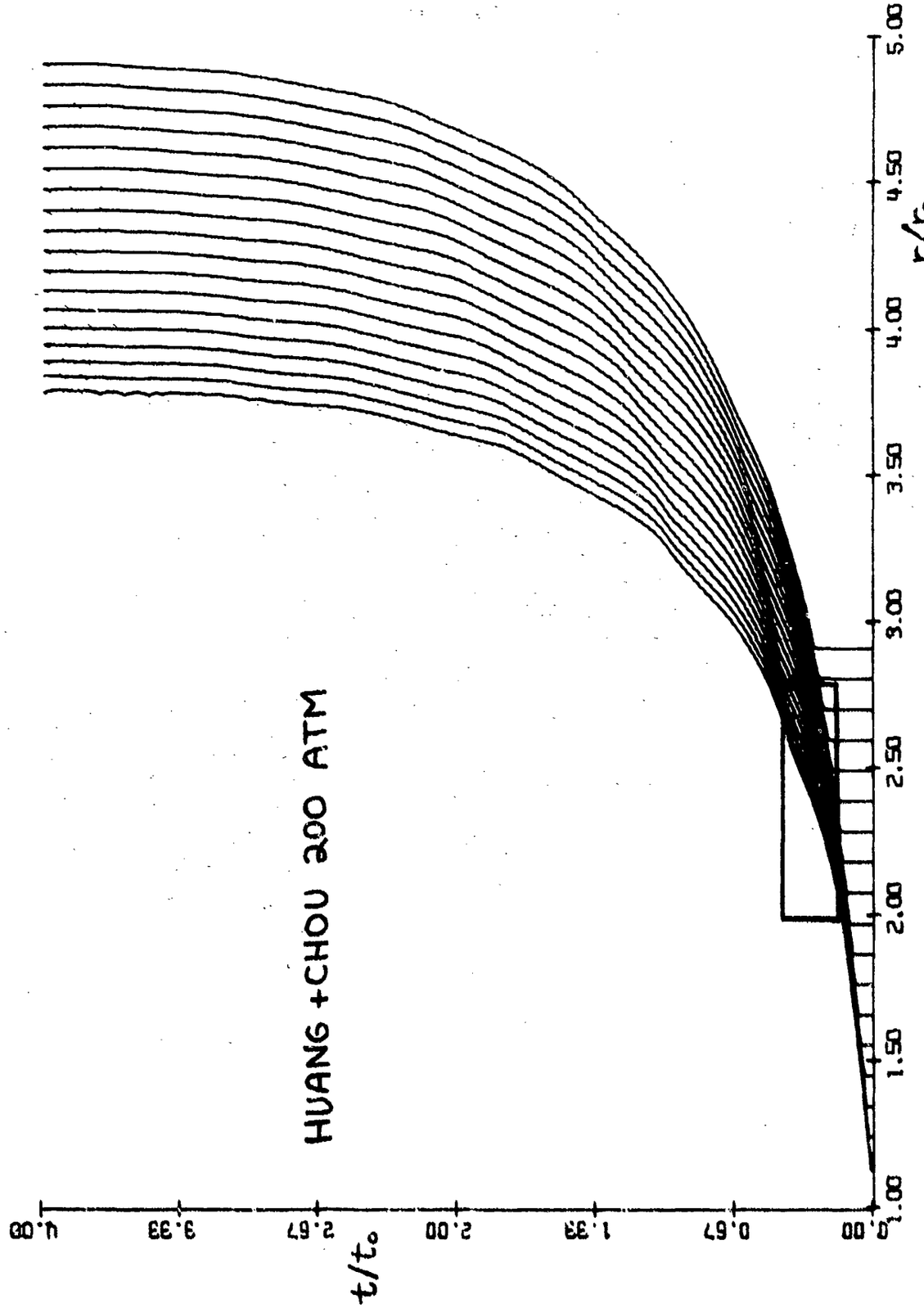

FIGURE 13:Particle Paths, Huang and Chou

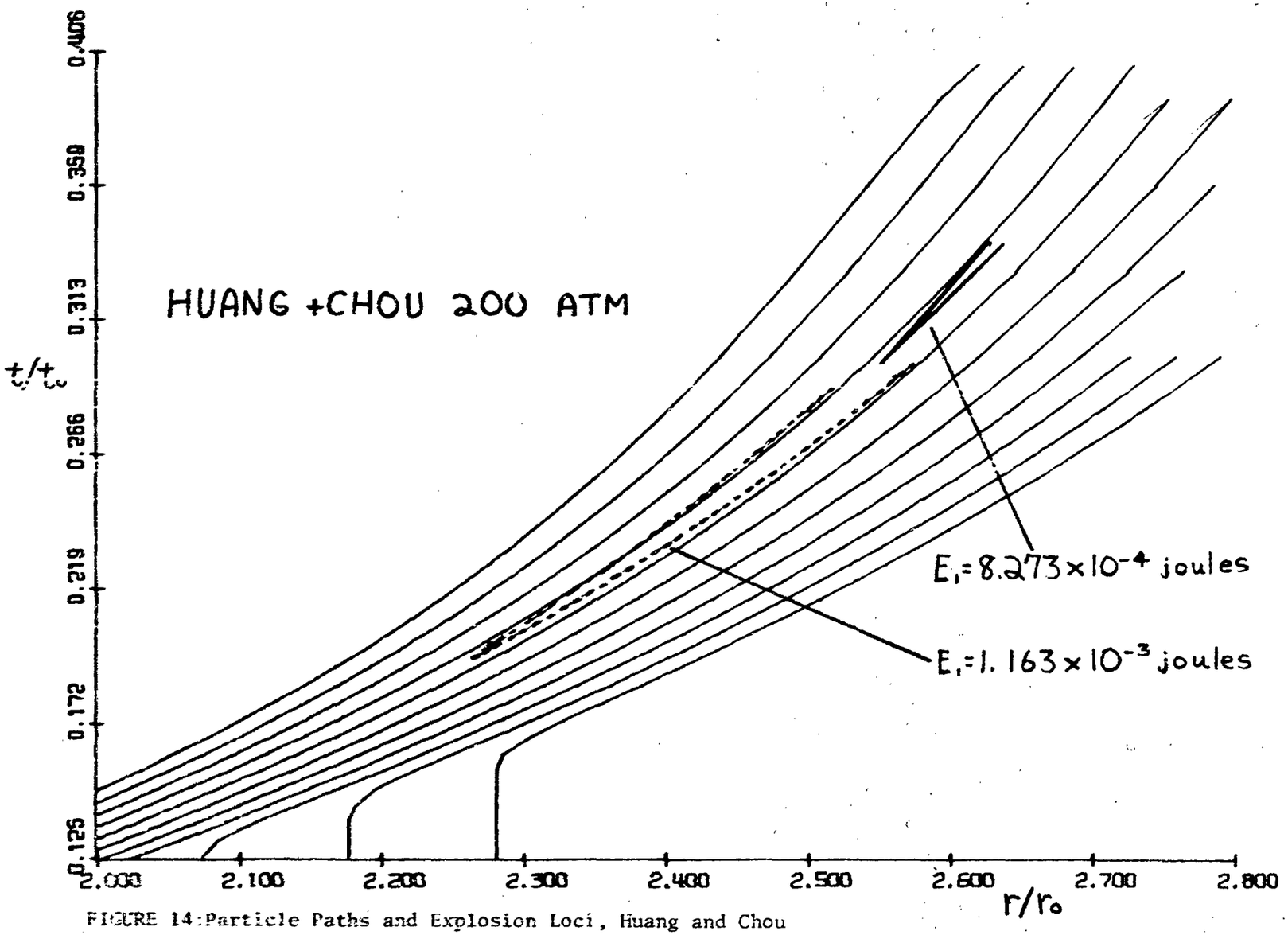

FIGURE 14: Particle Paths and Explosion Loci, Huang and Chou

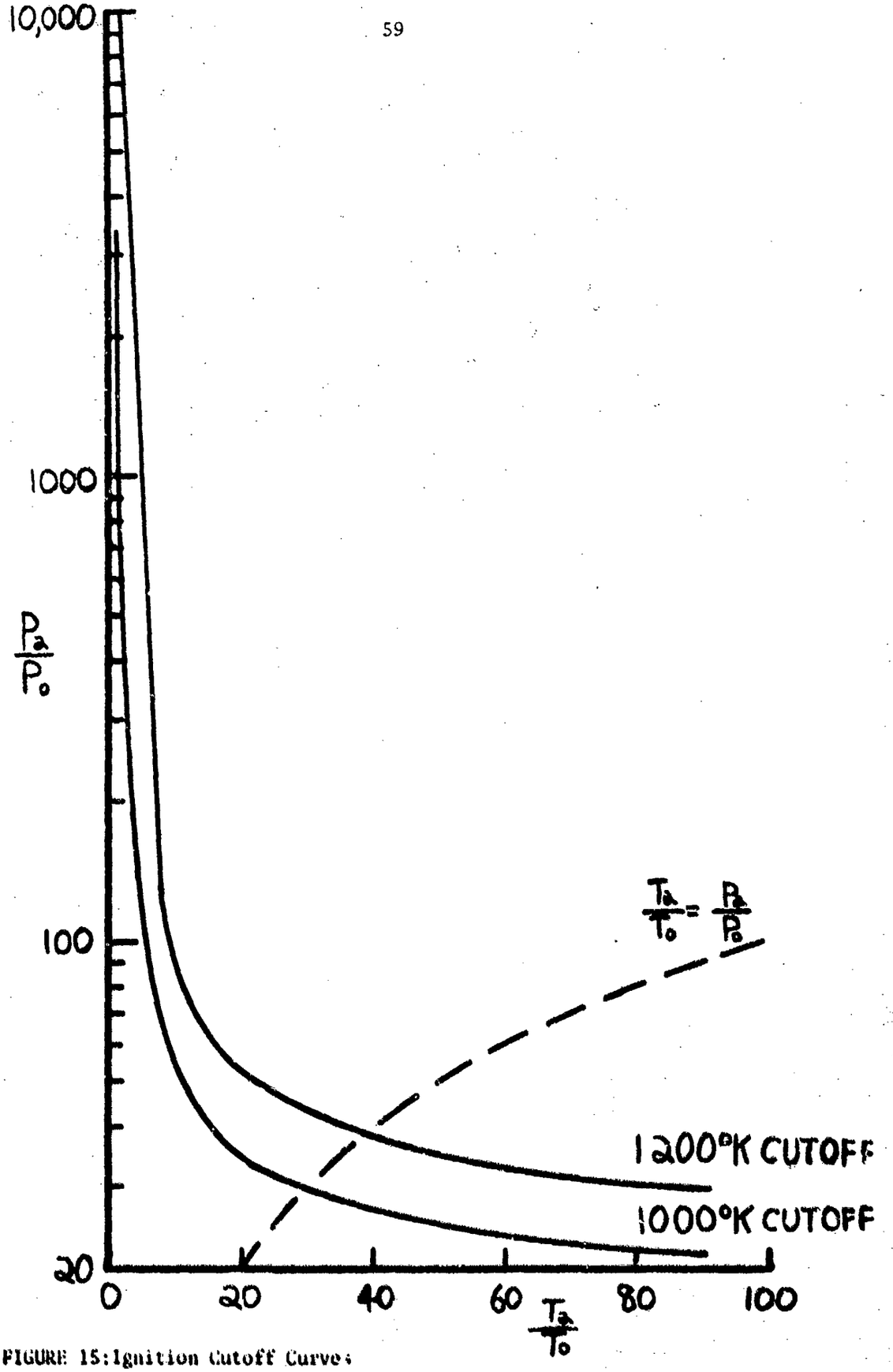

FIGURE 15: Ignition Cutoff Curves

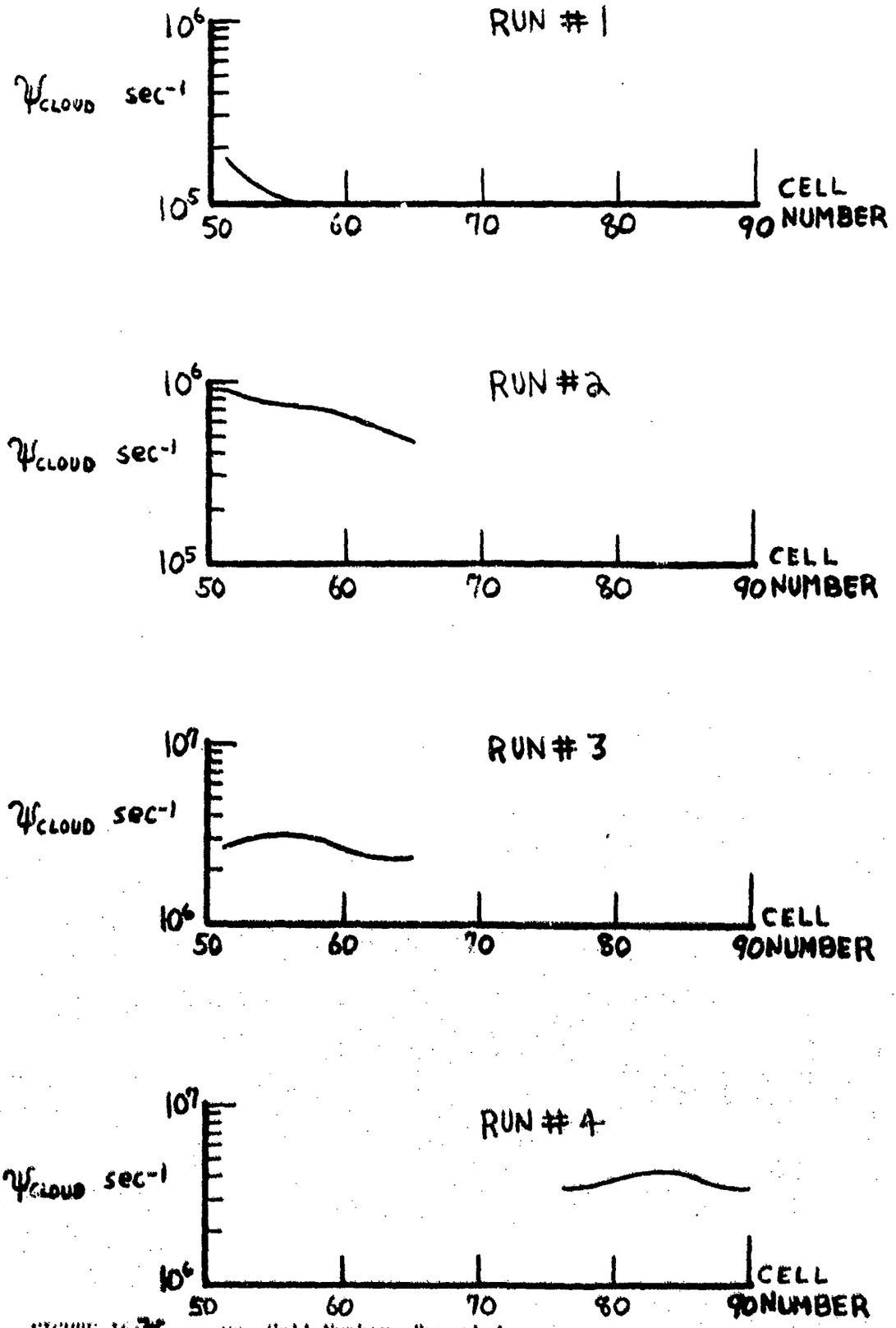

FIGURE 16: ψ_{CLOUD} vs. Cell Number, Runs 1-4

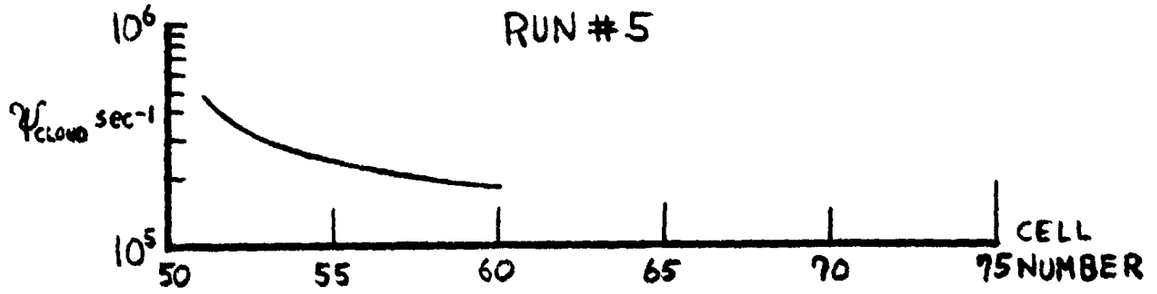

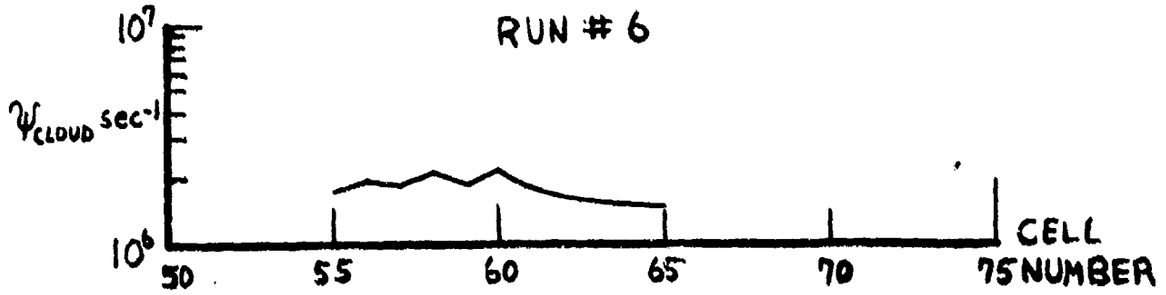

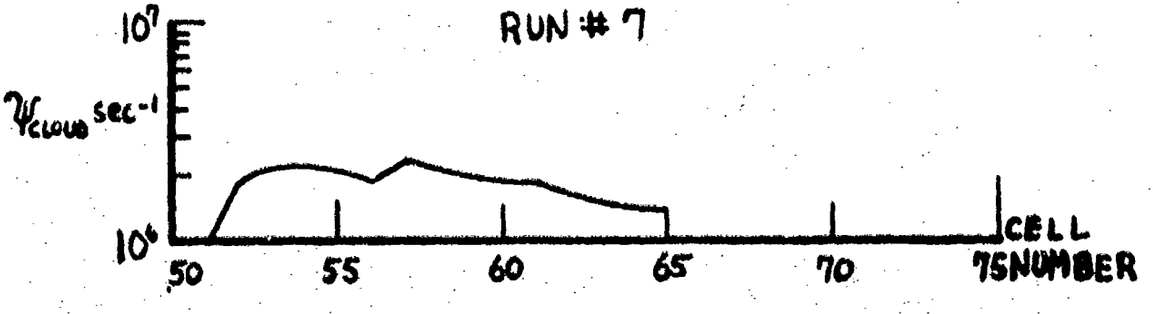

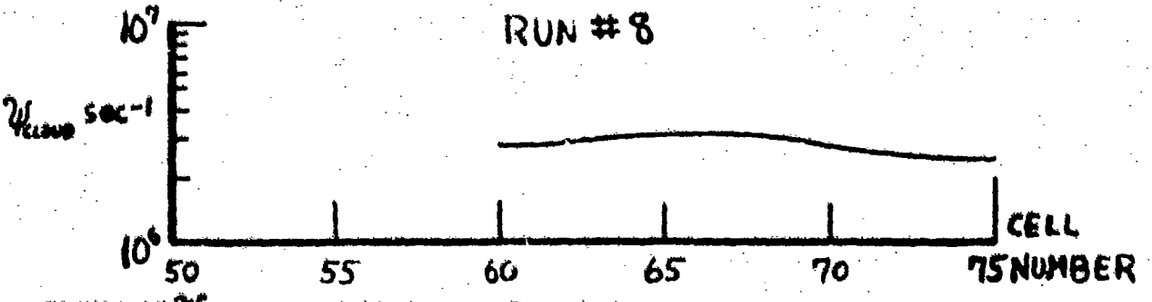

FIGURE 17: Ψ_{CLOUD} vs. Cell Number, Runs 5-8

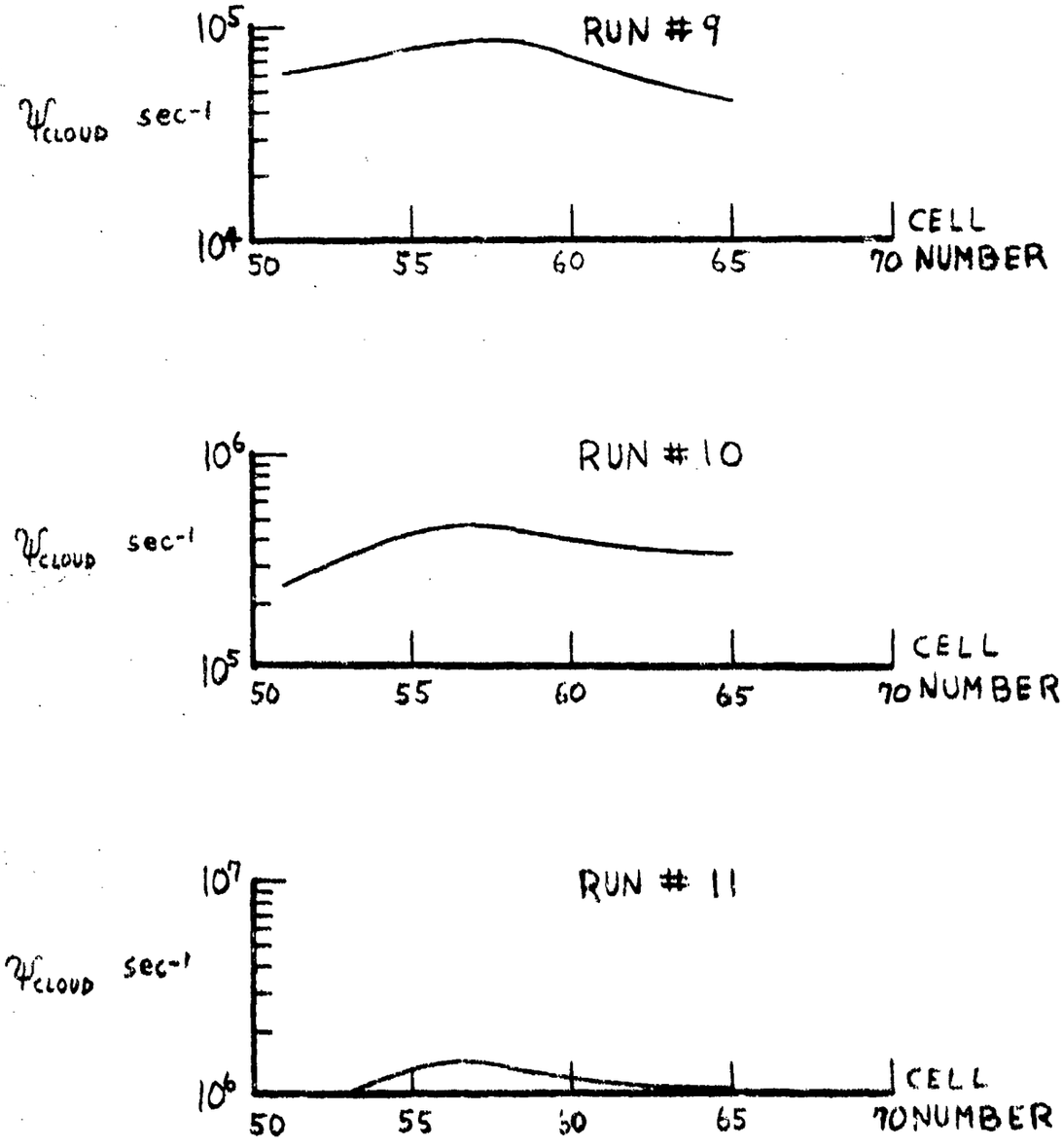

FIGURE 18: Ψ_{CLOUD} vs. Cell Number, Runs 9-11

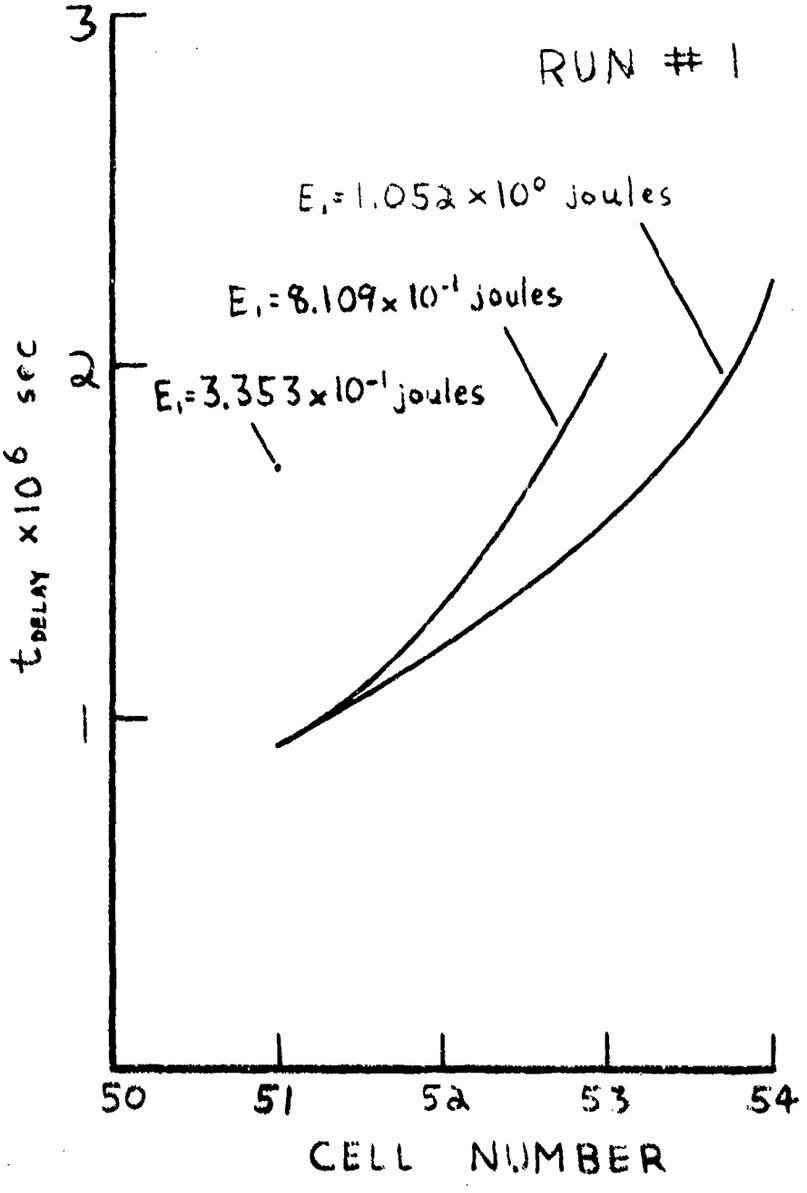

FIGURE 19:Delay Time to Ignition, Run #1

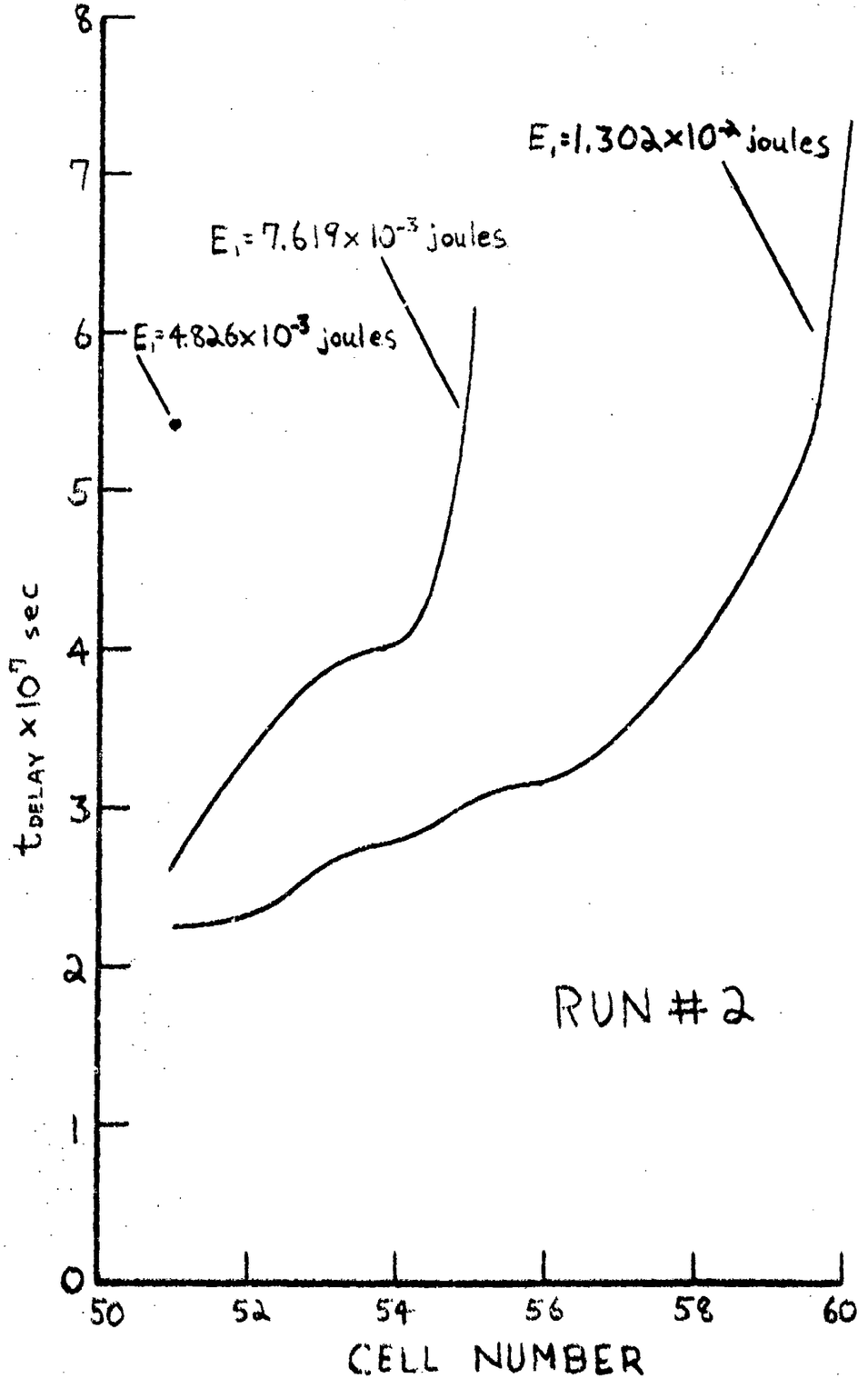

FIGURE 20:Delay Time to Ignition, Run #2

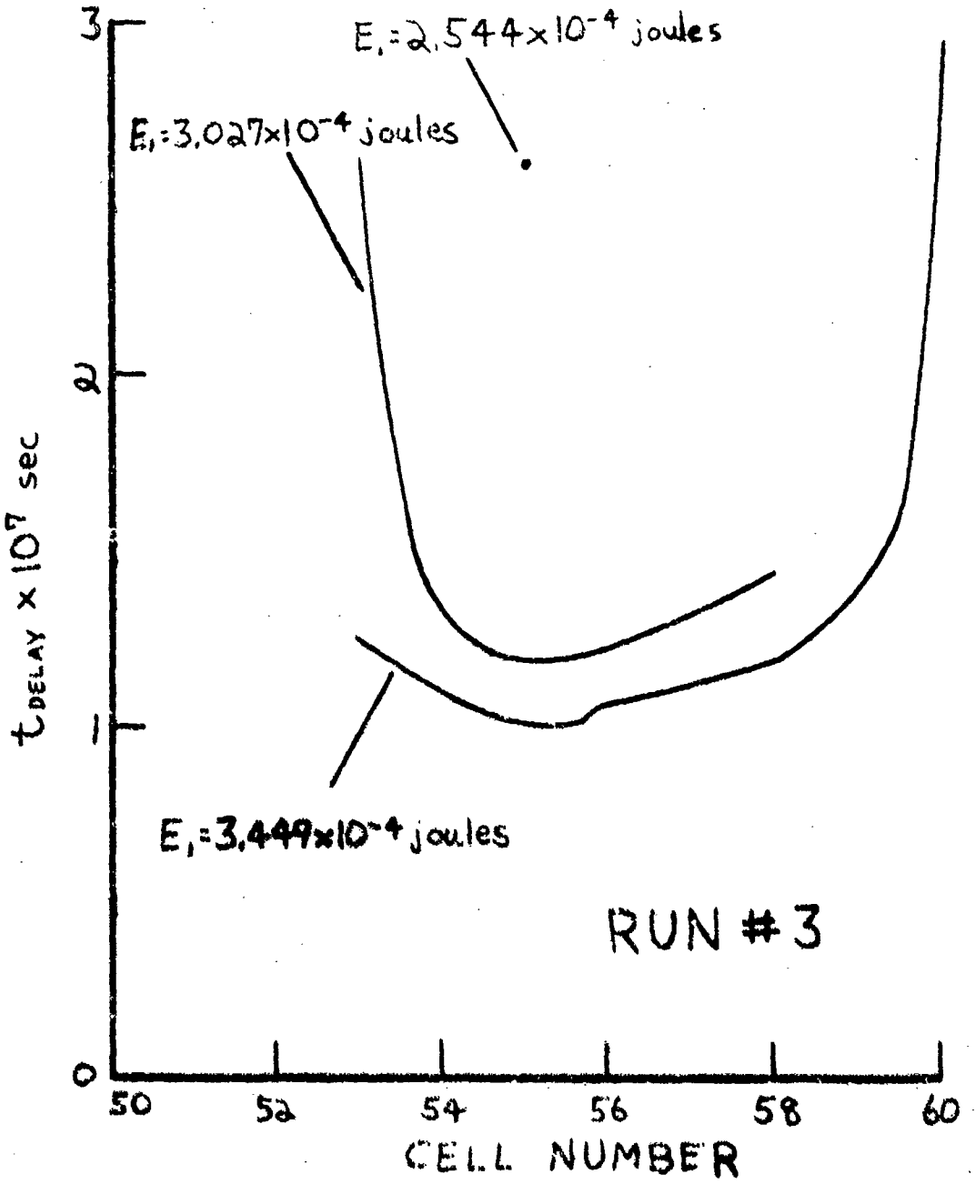

FIGURE 21:Delay Time to Ignition, Run #3

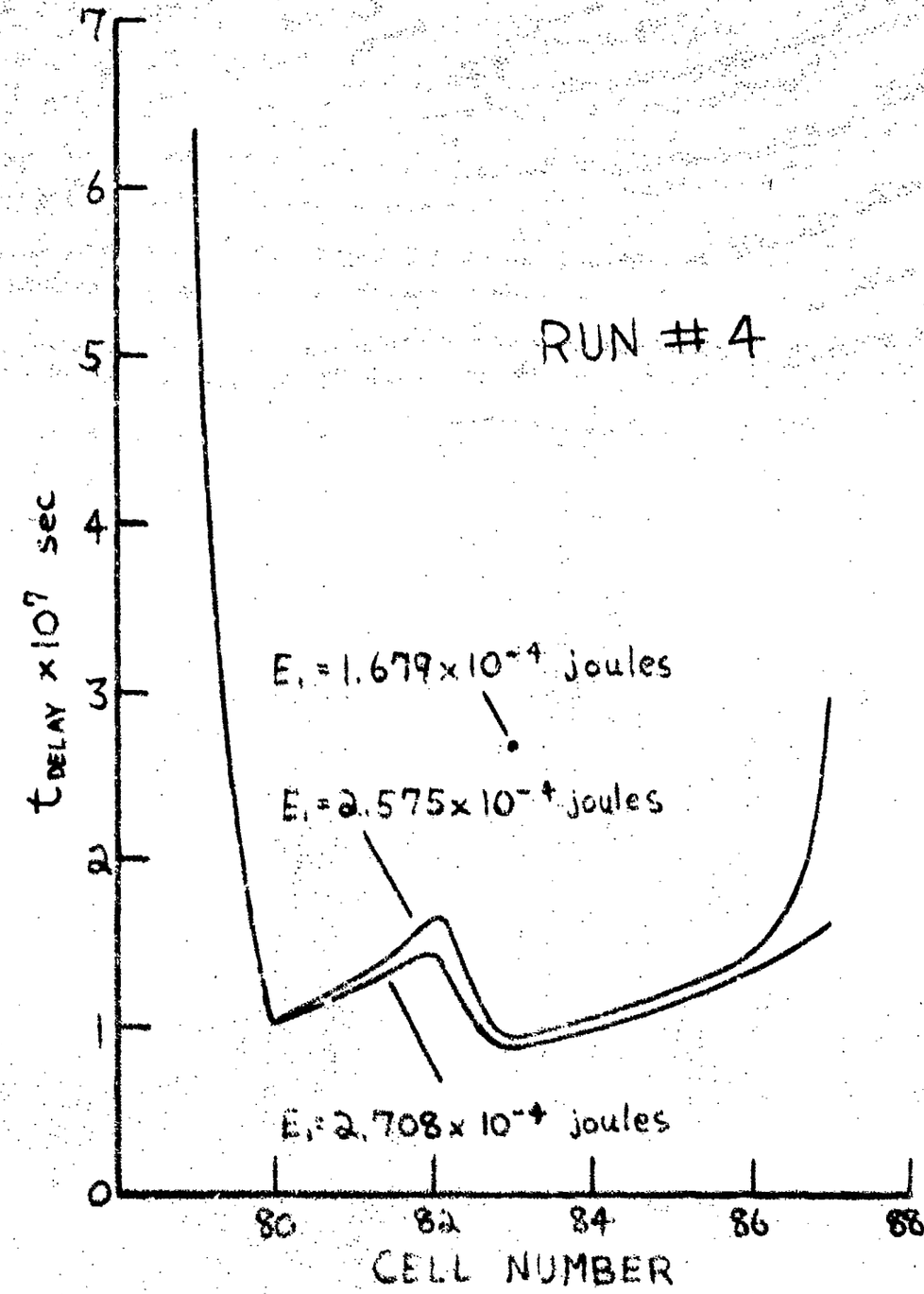

FIGURE 22:Delay Time to Ignition, Run #4

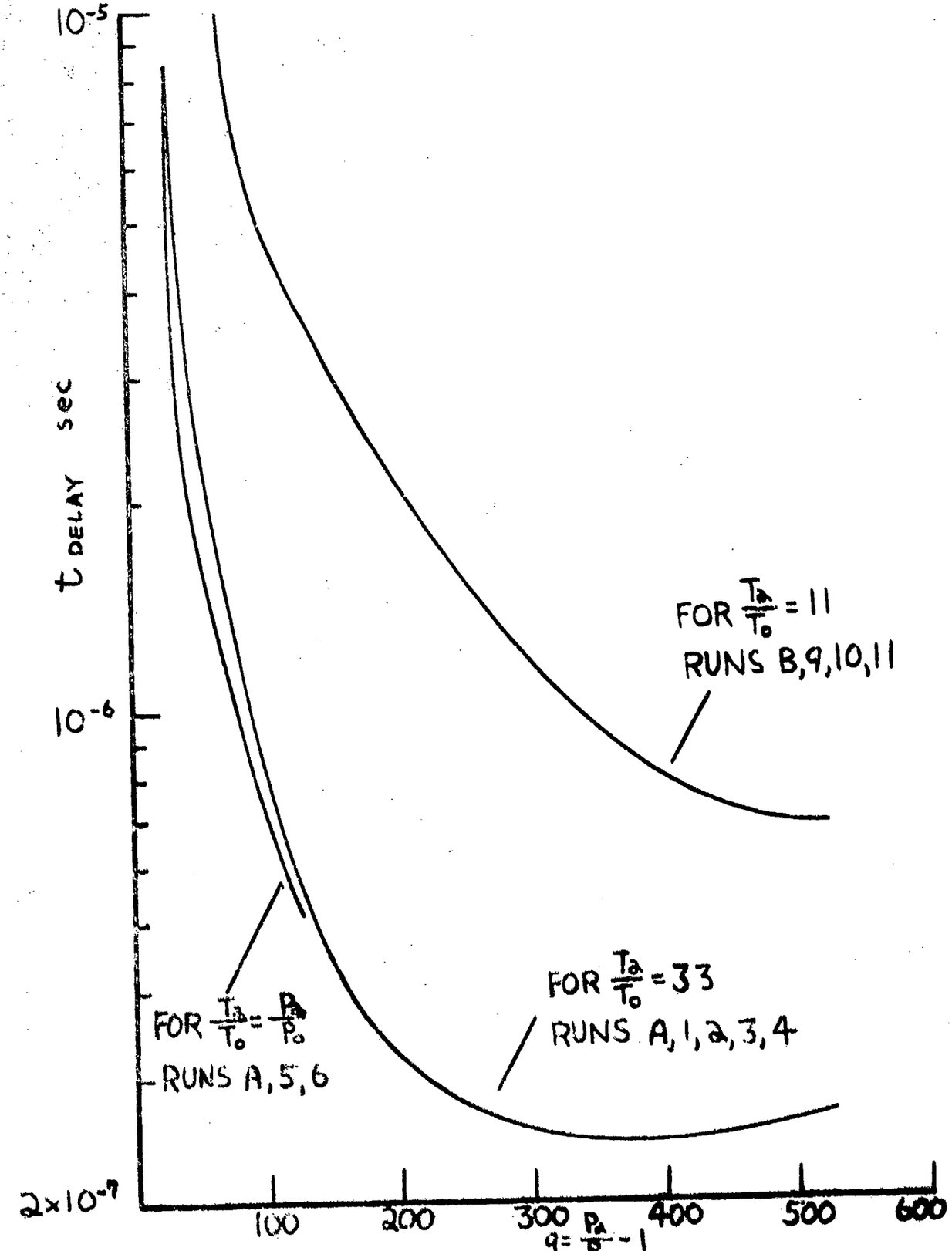

FIGURE 33: Delay Times for Minimum Energy Levels, Runs 1-11, A, B

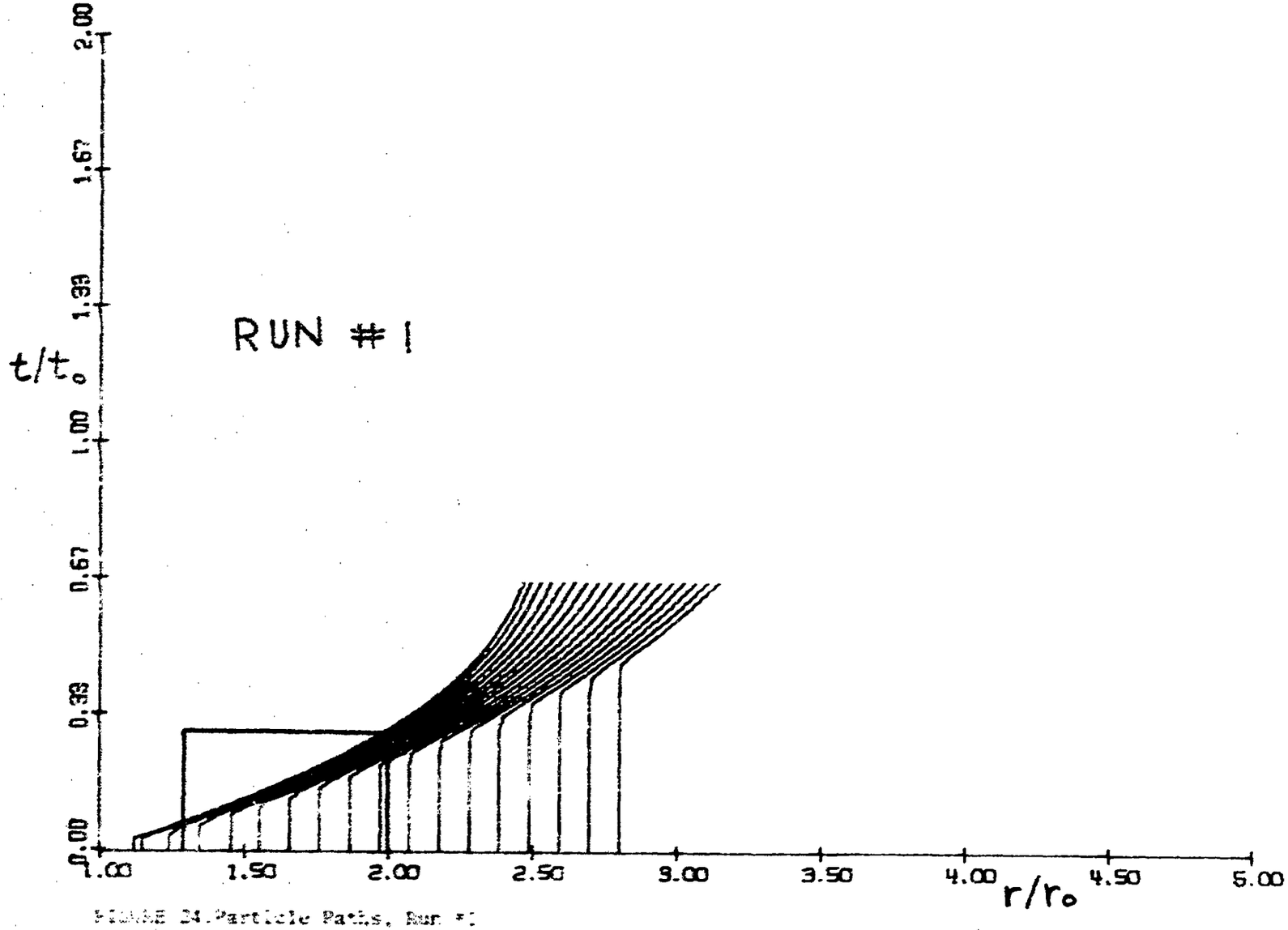

FIGURE 24. Particle Paths, Run #1

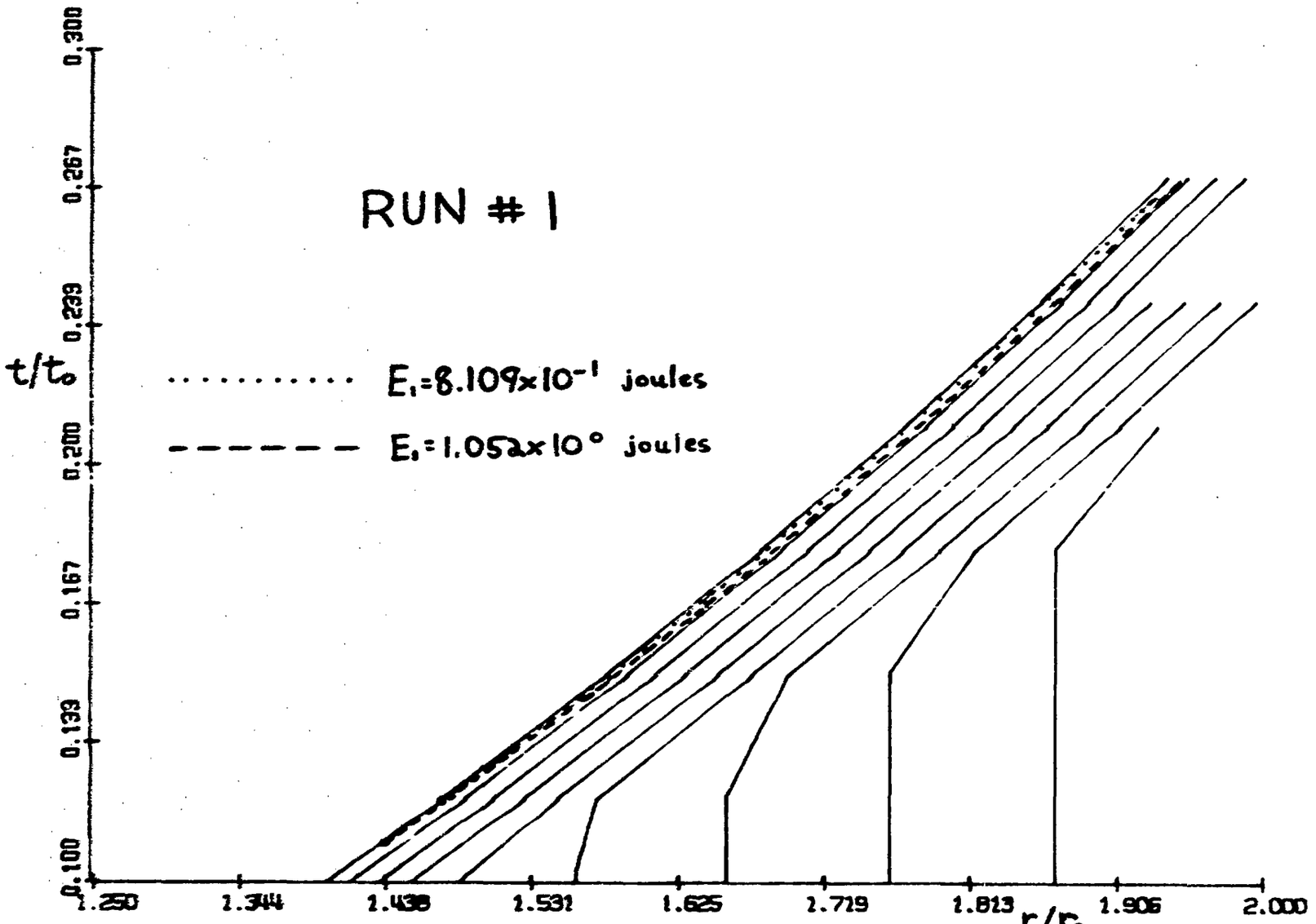

FIGURE 25:Particle Paths and Explosion Loci, Run #1

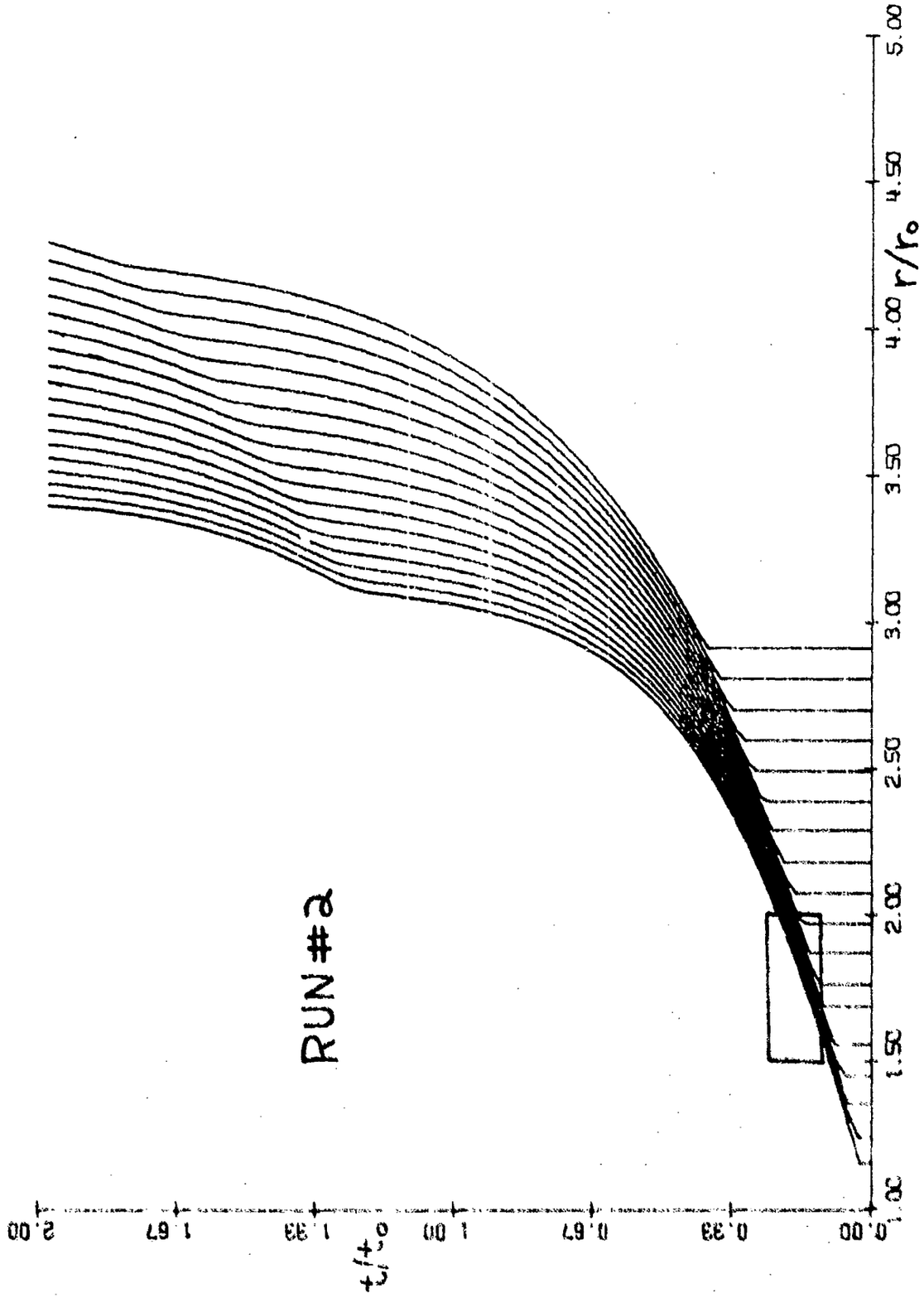

FIGURE 26: Particle Paths, Run #2

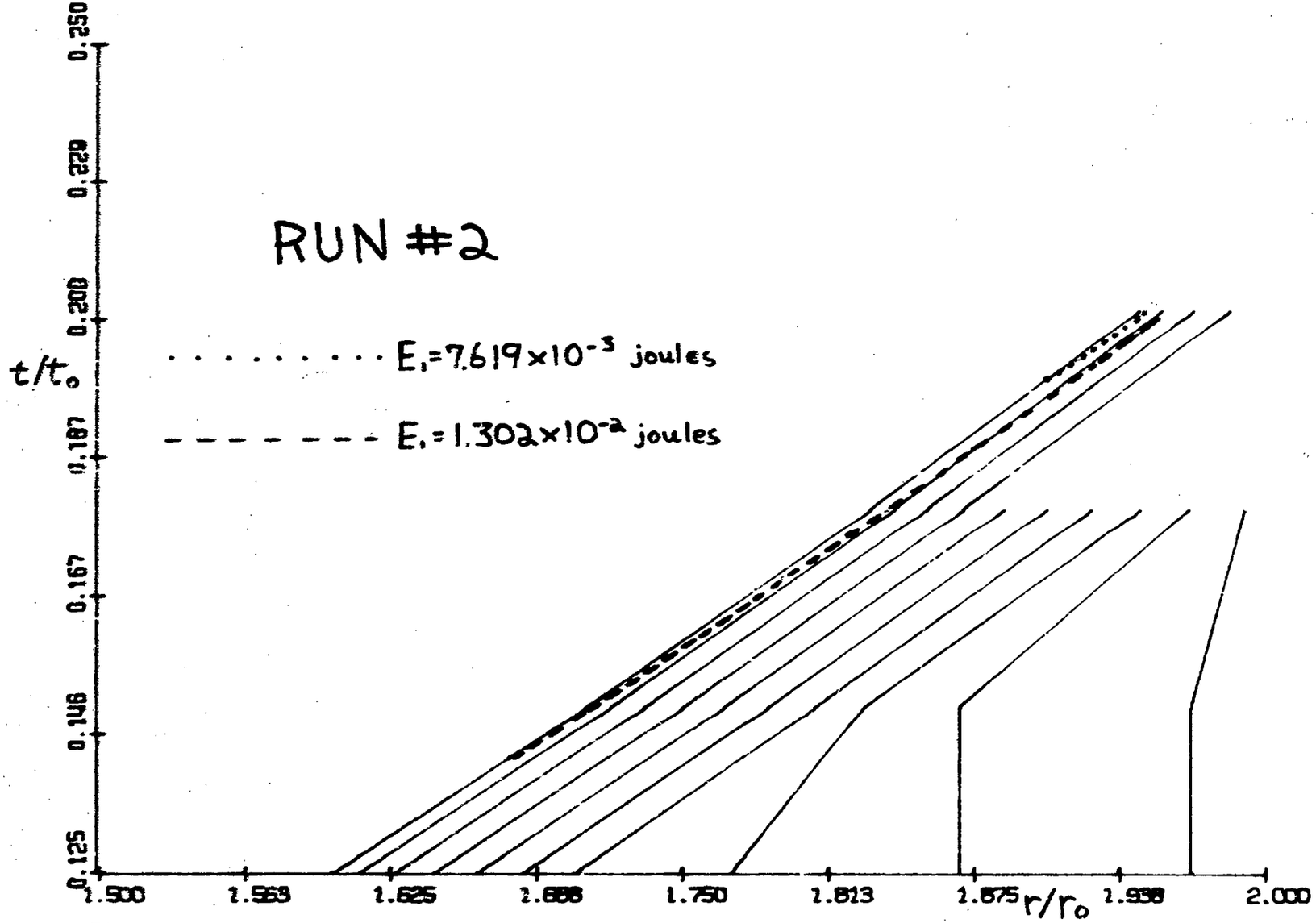

FIGURE 27:Particle Paths and Explosion Loci, Run #2

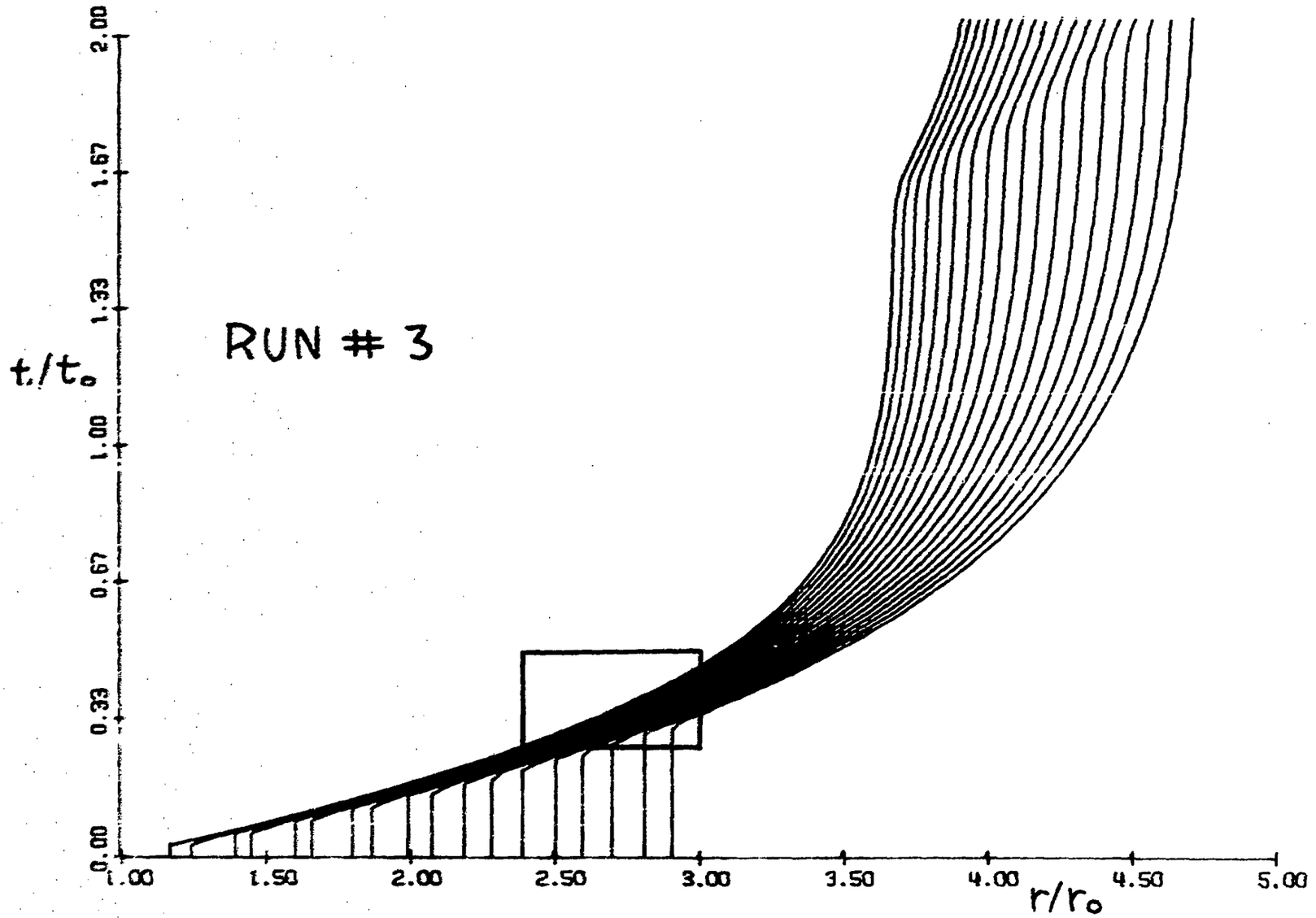

FIGURE 28:Particle Paths, Run #3

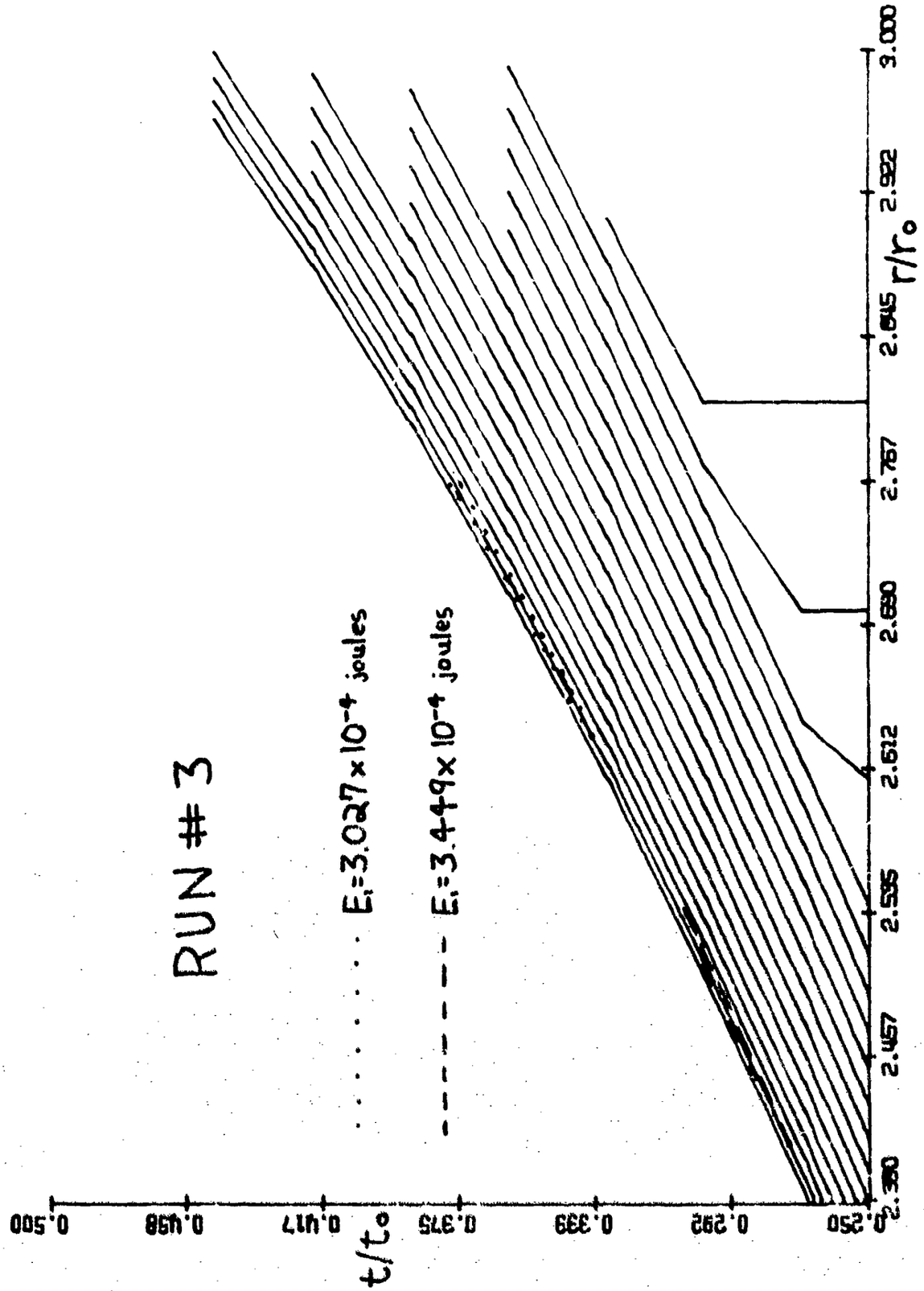

FIGURE 29:Particle Paths and Explosion Loci, Run #3

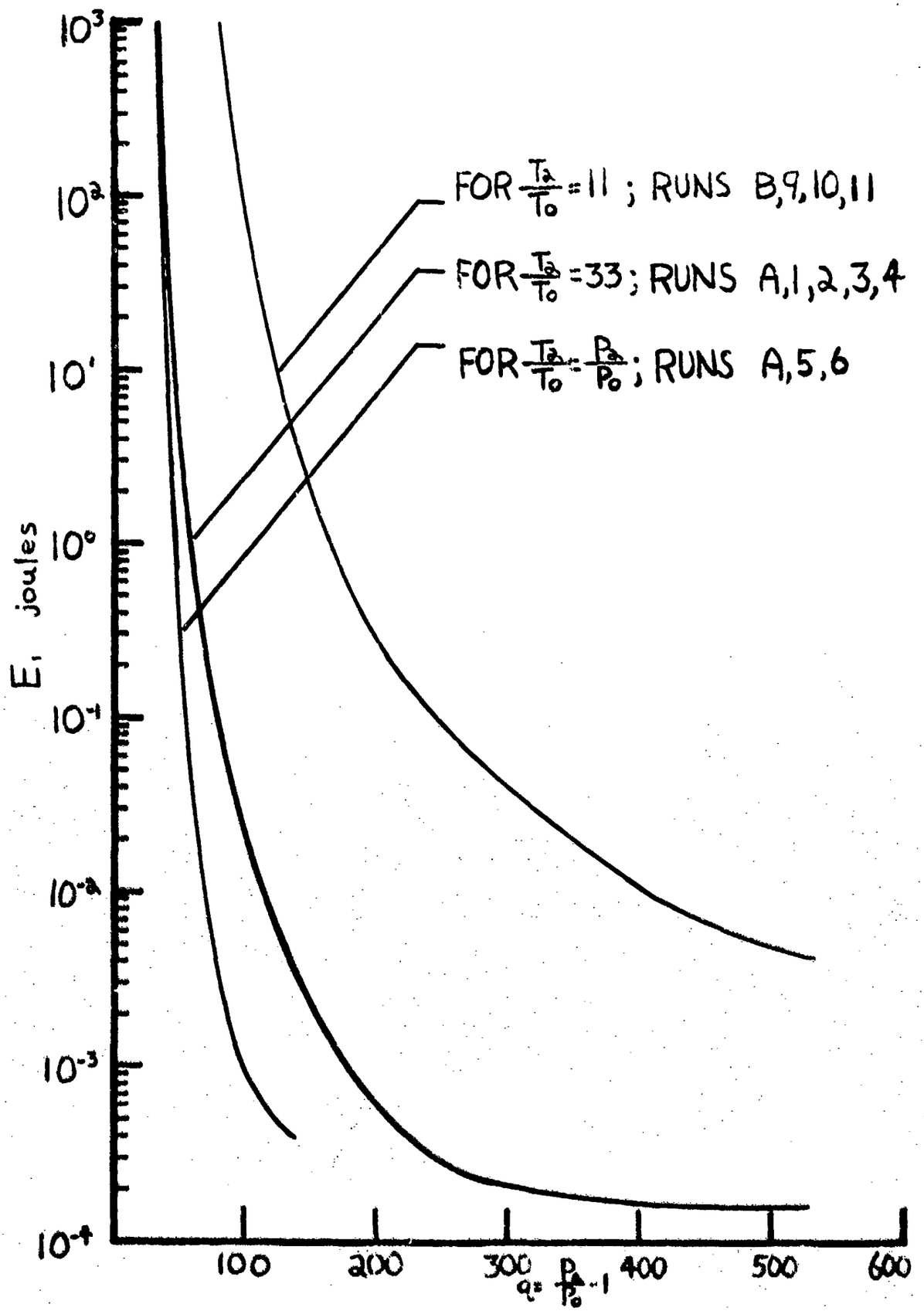

Minimum Ignition Energies, Bursting Sphere

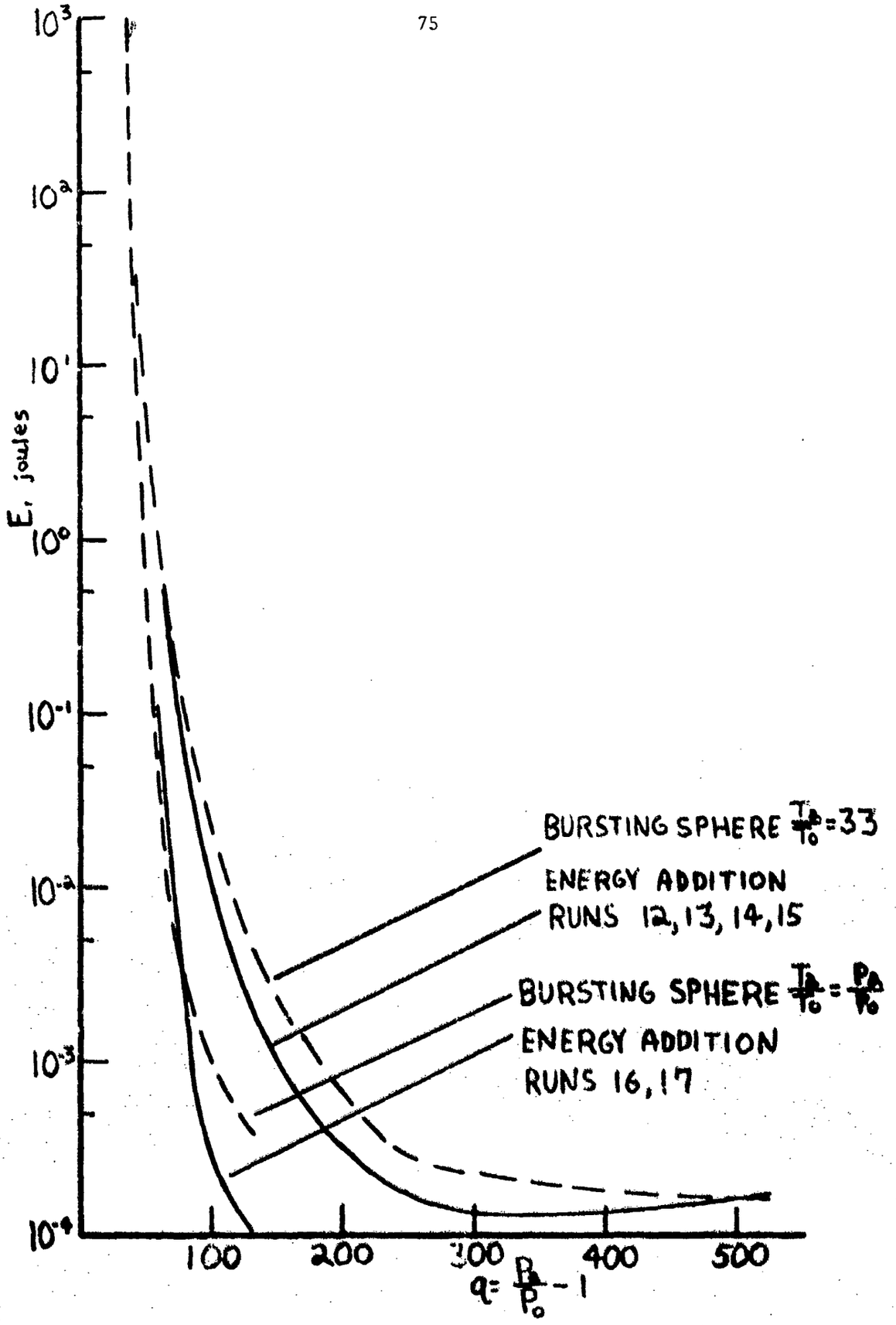

FIGURE 51: Minimum Ignition Energies, Energy Addition

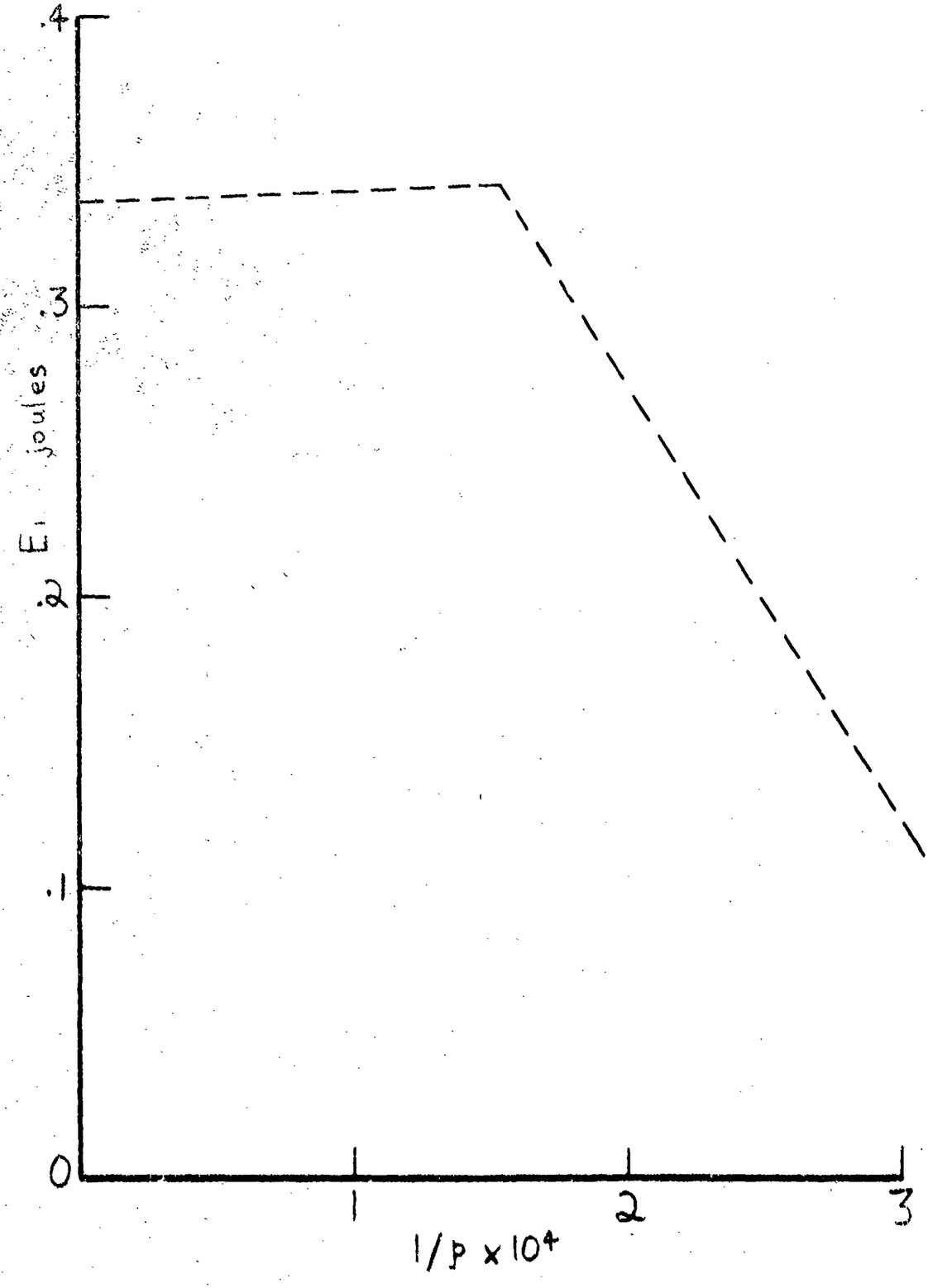

FIGURE 52:Power Density Effect on Minimum Ignition Energy

REFERENCES

1)Zel'dovich, Ia. B. and Kompaneets, A. S., Theory of Detonation, Academic Press Inc., New York, N. Y.

2)Barthel, H. O. and Strehlow, R. A., Wave Propagation in One-Dimensional Reactive Flows, Physics of Fluids 9, 1896-1907 (1966).

3)Barthel, H. O., Reaction Zone-Shock Front Coupling in Detonations, Physics of Fluids, 15, 43-50 (1972).

4)Oppenheim, A. K., Elementary Blast Wave Theory and Computations, University of California, Berkeley (1973).

5)Brode, H. L., Theoretical Solutions of Spherical Shock Tube Blasts, U. S. Air Force Project Rand Research Memorandum, ASTIA Document Number AD 206491 (Sept. 1957).

6)Huang, S. L. and Chou, P. C., Calculations of Expanding Shock Waves and Late-Stage Equivalence, Drexel Institute of Technology Report 125-12 (April 1968).

7)Strehlow, R. A. and Ricker, R., The Blast Wave From a Bursting Sphere, Acta Astronautica, submitted (1975).

8)Liepmann, H. W. and Roshko, A., Elements of Gasdynamics, John Wiley and Sons, Inc., New York, N. Y. (1957).

9)Sternberg, H. M., and Hurwitz H., Calculated Spherical Shock Waves Produced by Condensed Explosives in Air and Water, Advance copy for Sixth Detonation Symposium, Naval Surface Weapons Center, White Oak, Silver Spring, Maryland.

10)Cusey, R. E., Investigation of the Flow Properties Downstream of a Shock Wave Propagating into a Convergent Duct, Technical Report AAE 65-4, University of Illinois, Urbana, Illinois (1965).

11)Strehlow, R. A., Fundamentals of Combustion, International Textbook Company, Scranton, Pennsylvania (1968).

12)Schott, G. L. and Kinsey, J. L., Kinetic Studies of Hydroxyl Radicals in Shock Waves, Journal of Chemical Physics, 29, 1177-1182 (1958).

13)Strehlow, R. A. and Cohen, A., Initiation of Detonation, Physics of Fluids, 5, 97-101 (1962).

14)Adamczyk, A. A., An Investigation of Blast Waves Generated From Non-Ideal Energy Sources, Ph. D. Thesis, Aeronautical and Astronautical Engineering Dept., University of Illinois, Urbana, Illinois (1975).

15)Private Communication with Barthel, H. O.

UNIVERSITY OF ILLINOIS

RECENT AERONAUTICAL AND ASTRONAUTICAL ENGINEERING DEPARTMENT TECHNICAL REPORTS

Technical Report Number	Title	Author	Journal Publication
AAE 62-1	An Introduction to Viscoelastic Analysis	H. H. Hilton	Engineering Design for Plastics, Reinhold Publ. Corp., N.Y., 199-276 (1964).
AAE 62-2	A Method of Characteristics Analysis of Detonation Stability	R. A. Strehlow	
AAE 63-1	On Non-Stationary White Noise	Y. K. Lin	J. Acoust. Soc. Amer. 36:82-84 (1964).
AAE 63-2	Formulation and Evaluation of Approximate Analogies for Transient Temperature Dependent Linear Viscoelastic Media	H. H. Hilton and J. R. Clements	Proc. Conf. on Thermal Loading and Creep, Inst. Mech. Eng., London, 6.17-6.24(1964).
AAE 63-3	Free Vibrations of Continuous Skin-Stringer Panels with Non-Uniform Stringer Spacing and Panel Thickness	Y. K. Lin, T. J. McDaniel, B. K. Donaldson, C. F. Vail and W. J. Dwyer	AFML-TR-64-347, Wright-Patterson AFB (1965).
AAE 64-1	Random Vibrations of a Myklestad Beam	Y. K. Lin	AIAA J., 2:1448-1451 (1964).
AAE 64-2	On Detonation Initiation	R. A. Strehlow	AIAA J., 2:783-784 (1964).
AAE 64-3	A Theoretical Investigation of a Restrictive Model for Detonation Initiation	R. B. Gilbert	AIAA J., 4:1777-1783 (1966).

RECENT AERONAUTICAL AND ASTRONAUTICAL ENGINEERING DEPARTMENT TECHNICAL REPORTS (continued)

Technical Report Number	Title	Author	Journal Publication
AAE 64-4	Transfer Matrix Representation of Flexible Airplanes in Gust Response Study	Y. K. Lin	J. of Aircraft, 2:116-121 (1965).
AAE 64-5	Dynamic Characteristics of Continuous Skin-Stringer Panels	Y. K. Lin	Acoustical Fatigue in Aerospace Structures, Syracuse Univ. Press, 163-184 (1965).
AAE 64-6	Experimental Study of the Growth of Transverse Waves in Detonations	R. Liaugminas	See AAE 66-3
AAE 64-7	Nonstationary Excitation and Response in Linear Systems Treated as Sequences of Random Pulses	Y. K. Lin	Journal of the Acoustical Society of America, 38: 453-460 (1965).
AAE 65-1	Transverse Waves in Detonations	R. A. Strehlow and F. Dan Fernandes	Combustion and Flame, 9:109-119 (1965).
AAE 65-2	A Summary of Linear Viscoelastic Stress Analysis	H. H. Hilton	Solid Rocket Structural Integrity Abstracts, 2: 1-56 (1965).
AAE 65-3	Approximate Correlation Function and Spectral Density of the Random Vibration of an Oscillator with Non-Linear Damping	Y. K. Lin	AFMK-TR-66-62, Wright Patterson AFB (1966).
AAE 65-4	Investigation of the Flow Properties Downstream of a Shock Wave Propagating into a Convergent Duct	R. E. Cusey	See AAE 65-6

RECENT AERONAUTICAL AND ASTRONAUTICAL ENGINEERING DEPARTMENT TECHNICAL REPORTS (continued)

Technical Report Number	Title	Author	Journal Publication
AAE 65-5	A Method for the Determination of the Matrix of Impulse Response Functions with Special Reference to Applications in Random Vibration Problems	Y. K. Lin	AFFDL-TR-66-80, Wright Patterson AFB, 743-751 (1966).
AAE 65-6	Convergent Channel Shock Tube for Detonation Initiation Studies	A. J. Crooker	"Detonation and Initiation Behind an Accelerating Shock Wave" by R. A. Strehlow, A. J. Crooker, R. E. Cusey, Comb and Flame, 11:339-351 (1967).
AAE 66-1	A Comparison of Experimental and Theoretical Transverse Wave Spacings in Detonation	R. H. Watson	See AAE 66-3
AAE 66-2	A Simple Model for the Mechanism of Detonation	J. R. Eyman	See AAE 66-3
AAE 66-3	Transverse Wave Structure in Detonations	R. A. Strehlow, R. Liaugminas, R. H. Watson and J. R. Eyman	11th Symposium (International) on Combustion, Mono Book Corp. Baltimore, Md., (1967).
AAE 66-4	A Real Gas Analysis Using an Acoustic Model for the Transverse Wave Spacing in Detonations	R. E. Maurer	AIAA Journal, 7: 323-328, (1969).
AAE 67-1	Shock Tube Studies in Exothermic Systems	R. A. Strehlow	Phys. Fluids, 12: 96-100, (1969).

RECENT AERONAUTICAL AND ASTRONAUTICAL ENGINEERING DEPARTMENT TECHNICAL REPORTS (continued)

Technical Report Number	Title	Author	Journal Publication
AAE 67-2	Shock Tube Chemistry	R. A. Strehlow	Progress in High Temperature Physics and Chemistry, Pergamon Press, N.Y., 2: 127-176 (1968).
AAE 67-3	Structural Failure Criteria for Solid Propellants Under Multiaxial Stresses	A. R. Zak	J. Spacecraft, 5: 265-269 (1968)
AAE 67-4	Structural Analysis of Realistic Solid Propellant Materials	A. R. Zak	J. Spacecraft, 5: 270-275 (1968).
AAE 67-5	Characteristics of Transverse Waves in Detonations of H_2, C_2H_2, C_2H_4 and CH_4 - Oxygen Mixtures	C. D. Engel	AIAA Journal, 7: 492-496 (1969).
AAE 68-1	A Review of Shock Tube Chemistry	R. A. Strehlow	Progress in High Temperature Physics and Chemistry, Pergamon Press, N.Y., 2: 1-146 (1969).
AAE 68-2	On the Interpretation of Molecular Beam Data	A. Klavins	A. Klavins and L. H. Sentman Rev. Sci. Instr., 41: 1560-1567 (1970).
AAE 68-3	Detonative Mach Stems	R. A. Strehlow H. O. Barthel	
AAE 68-4	On the Strength of Transverse Waves and Geometrical Detonation Cell Model for Gas Phase Detonations	J. R. Biller	R. A. Strehlow and J. R. Biller Comb. and Flame, 13: 577-582, (1970).
AAE 68-5	The MISTRESS User Manual	H. H. Hilton	
AAE 69-1	The Chemical Shock Tube - Implications of Flow Non-Idealities	R. A. Strehlow R. L. Belford	

RECENT AERONAUTICAL AND ASTRONAUTICAL ENGINEERING DEPARTMENT TECHNICAL REPORTS (continued)

Technical Report Number	Title	Author	Journal Publication
AAE 69-2	Phenomenological Investigation of Low Mode Marginal Planar Detonations	A. J. Crooker	Acta Astronautica, 1:303-315(1974).
AAE 69-3	Multi-Dimensional Detonation Wave Structure	R. A. Strehlow	Astronautica Acta, 15:345-358(1970).
AAE 69-4	An Experimental and Analytical Investigation of a Two-Dimensionally Stiffened Panel	A. R. Zak C. E. French	AFML-TR-68-390, Wright-Patterson AFB,(1969).
AAE 69-5	On the Kinetic Equations for a Dilute, Short Range Gas	T. J. Forster L. H. Sentman	with A.D. Grimm, Proc. Ninth International Symposium on Rarefied Gas Dynamics, A3.1-3.8 (1974).
AAE 69-6	The Sawtooth Column of the Supersonic Electric Arc in Sulfur Hexafluoride	C. E. Bond	AIAA J., 9: 510-512 (1971).
AAE 69-7	Theoretical and Experimental Analysis of Stiffened Panels Under Dynamic Conditions	A. R. Zak R. N. Yurkovich J. H. Schmidt	J. of Aircraft, 3: 149-155 (1971).
AAE 70-1	On the Interaction Between Chemical Kinetics and Gas-Dynamics in the Flow Behind a Cylindrical Detonation Front	S. Rajan	
AAE 70-2	Preliminary Studies on the Engineering Applications of Finite Difference Solutions of the Navier-Stokes Equations	W. F. Van Tassell	
AAE 70-3	Some Aspects of the Surface Boundary Condition in Kinetic Theory	A. Klavins	Proc. of International Symposium on Rarefied Gas Dynamics, Pisa, Italy (1970).

RECENT AERONAUTICAL AND ASTRONAUTICAL ENGINEERING DEPARTMENT TECHNICAL REPORTS (continued)

Technical Report Number	Title	Author	Journal Publication
AAE 67-2	Shock Tube Chemistry	R. A. Strehlow	Progress in High Temperature Physics and Chemistry, Pergamon Press, N.Y., 2: 127-176 (1968).
AAE 67-3	Structural Failure Criteria for Solid Propellants Under Multiaxial Stresses	A. R. Zak	J. Spacecraft, 5: 265-269 (1968)
AAE 67-4	Structural Analysis of Realistic Solid Propellant Materials	A. R. Zak	J. Spacecraft, 5: 270-275 (1968).
AAE 67-5	Characteristics of Transverse Waves in Detonations of H_2, C_2H_2, C_2H_4 and CH_4 - Oxygen Mixtures	C. D. Engel	AIAA Journal, 7: 492-496 (1969).
AAE 68-1	A Review of Shock Tube Chemistry	R. A. Strehlow	Progress in High Temperature Physics and Chemistry, Pergamon Press, N.Y., 2: 1-146 (1969).
AAE 68-2	On the Interpretation of Molecular Beam Data	A. Klavins	A. Klavins and L. H. Sentman Rev. Sci. Instr., 41: 1560-1567 (1970).
AAE 68-3	Detonative Mach Stems	R. A. Strehlow H. O. Barthel	
AAE 68-4	On the Strength of Transverse Waves and Geometrical Detonation-Cell Model for Gas Phase Detonations	J. R. Biller	R. A. Strehlow and J. R. Biller Comb. and Flame, 13: 577-582, (1970).
AAE 68-5	The MISTRESS User Manual	H. H. Hilton	
AAE 69-1	The Chemical Shock Tube - Implications of Flow Non-Idealities	R. A. Strehlow R. L. Belford	

RECENT AERONAUTICAL AND ASTRONAUTICAL ENGINEERING DEPARTMENT TECHNICAL REPORTS (continued)

Technical Report Number	Title	Author	Journal Publication
AAE 70-4	A Study of the Transient Behavior of Fuel Droplets during Combustion: Theoretical Considerations for Aerodynamic Stripping	H. Krier	
AAE 70-5	On the Solid Body Model for an Accelerating Electric Arc	F. Klett	
AAE 71-1 UILU-ENG 71 0501	Detonative Mach Stems	R. A. Strehlow H. O. Barthel	
AAE 71-2 UILU-ENG 71 0502	An Investigation of Transient Phenomena in Detonations	R. J. Stiles	with R. A. Strehlow, A. A. Adamczyk, Astronautica Acta, 17: 509-527 (1972)
AAE 71-3 UILU-ENG 71 0503	On the Role of Tangential Velocity Changes in the Scattering of a Molecular Beam from A Solid Surface	C. C. Chrisman L. H. Sentman	Chemical Physics Letters, 26:407-413(1974)
AAE 72-1 UILU-ENG 72 0501	Unconfined Vapor Cloud Explosions - An Overview	R. A. Strehlow	Fourteenth Symposium on Combustion, 1189-1200 (1973).
AAE 72-2 UILU-ENG 72 0502	Application of Illiac IV Computer to Numerical Solutions of Structural Problems	H. H. Hilton A. R. Zak J. J. Kessler F. C. Rockenbach	
AAE 72-3 UILU-ENG 72 0503	On the Measurement of Energy Release Rates In Vapor Cloud Explosions	R. A. Strehlow L. D. Savage G. M. Vance	Combustion Science and Technology, 6: 307-312 (1972).

RECENT AERONAUTICAL AND ASTRONAUTICAL ENGINEERING DEPARTMENT TECHNICAL REPORTS (continued)

Technical Report Number	Title	Author	Journal Publication
AAE 72-4 UILU-ENG 72 0504	A Performance Comparison of Several Numerical Minimization Algorithms	J. E. Prussing	
AAE 73-1 UILU-ENG 73 0501	Stresses and Damping in the Matrix of a Composite Material	A. R. Zak	
AAE 73-2 UILU-ENG 73 0502	Early Burning Anomalies in the XM 645 Flechette Cartridge	H. Krier D. R. Hall	BRL Rept. No. 104 (1973).
AAE 73-3 UILU-ENG 73 0503	Equivalent Explosive Yield of the Explosion in the Alton Southern Gateway Yard, East St. Louis, Ill., January 22, 1972	R. A. Strehlow	
AAE 73-4 UILU-ENG 73 0504	Failure Studies of Gaseous Detonations	R. J. Salm	Acta Astronautica (in press).
AAE 73-5 UILU-ENG 73 0505	An Investigation of Hydrogen-Oxygen-Argon Detonations	J. R. Biller	
AAE 73-6 UILU-ENG 73 0506	Interior Ballistic Predictions Using Data From Closed and Variable-Volume Simulators	H. Krier S. A. Shimpi M. J. Adams	Proc. 11th JANNAF Combustion Meeting, CPIA Publ. 261:17-30(1974).
AAE 73-7 UILU-ENG 73 0507	Theory of Rotationally Symmetric Laminar Premixed Flames	G. M. Vance H. Krier	Comb. and Flame J., 22: 365-375 (1974).
AAE 73-8 UILU-ENG 73 0508	Burning of Fuel Droplets at Elevated Pressures	J. H. Rush H. Krier	Comb. and Flame J., 22: 377-382 (1974).
AAE 73-9 UILU-ENG 73 0509	An Impact Ignition Model for Solid Propellants	H. Krier H. H. Hilton O. Olorunsola D. L. Reuss	BRL Rept. No. 1707 (1974).

RECENT AERONAUTICAL AND ASTRONAUTICAL ENGINEERING DEPARTMENT TECHNICAL REPORTS (continued)

Technical Report Number	Title	Author	Journal Publication
AAE 73-10 UILU-ENG 73 0510	Optimal Multiple-Impulse Direct Ascent Fixed-Time Rendezvous	J. E. Prussing L. R. Gross	AIAA J., 12, 885-889 (1974).
AAE 73-11 UILU-ENG 73 0511	The Structure and Stability of Detonation Waves	R. A. Strehlow	
AAE 74-1 UILU-ENG 74 0501	Model of Flame Spreading and Combustion Through Packed Beds of Propellant Grains	H. Krier W. F. Van Tassell S. Rajan J. T. Ver Shaw	BRL Report No. 147 (1974). Int. J. Heat-Mass Transfer, 1377-86 (1975).
AAE 74-2 UILU-ENG 74 0502	On the Nature of Non-Ideal Blast Waves	R. A. Strehlow A. A. Adamczyk	WSS/CI Paper No. 74-12, Pullman, Wash. (1974).
AAE 74-3 UILU-ENG 74 0503	Viscous Incompressible Flow in Spiral Channels	W. F. VanTassell	
AAE 74-4 UILU-ENG 74 0504	Frequency Response Functions of a Disordered Periodic Beam	J. N. Yang Y. K. Lin	J. Sound and Vibration 38: 317-340 (1975).
AAE 74-5 UILU-ENG 74 0505	Predicting Uniform Gun Interior Ballistics: Part I. An Analysis of Closed Bomb Testing	H. Krier S. A. Shimpi	Comb. and Flame J. 25: 229-240 (1975).
AAE 74-6 UILU-ENG 74 0506	Predicting Uniform Gun Interior Ballistics: Part II. The Interior Ballistic Code	H. Krier M. J. Adams	Proc. 11th JANNAF Comb. Meeting, CPIA Publ. 261: 17-30 (1974).
AAE 74-7 UILU-ENG 74 0507	Predicting Uniform Gun Interior Ballistics: Part III. The Concept and Design of the Dynagun Ballistic Simulator	H. Krier J. W. Black	Proc. 11th JANNAF Comb. Meeting, CPIA Publ. 261: 31-43(1974).
AAE 74-8 UILU-ENG 74 0508	Process of Fluidization During Porous Solid Propellant Combustion	H. Krier J. T. Ver Shaw	AIAA Paper 75-242 (1975).
AAE 74-9 UILU-ENG 74 0509	An Analysis of Flame Propagation Through Coal Dust-Air Mixtures	J. L. Krazinski H. Krier	AIAA Paper 74-1111 (1974).

RECENT AERONAUTICAL AND ASTRONAUTICAL ENGINEERING DEPARTMENT TECHNICAL REPORTS (continued)

Technical Report Number	Title	Author	Journal Publication
AAE 74-10 UILU-ENG 74 0510	An Interior Ballistics Prediction of the M549 Rocket Assisted Projectile	H. Krier S. Shimpi E. Meister	
AAE 75-1 UILU-ENG 75 0501	Dynamically Induced Thermal Stresses in Composite Material, Structural Panels	A. Zak W. Drysdale	
AAE 75-2 UILU-ENG 75 0502	Numerical Analysis of Laminated, Orthotropic Composite Structures	A. R. Zak	
AAE 75-3 UILU-ENG 75 0503	The Characterization and Evaluation of Accidental Explosions	R. A. Strehlow W. E. Baker	NASA CR 134779 (June 1975). Also Progr. Energy & Comb. Sc. (in press).
AAE 75-4 UILU-ENG 75 0504	Program Manual for the Eppler Airfoil Inversion Program	W. G. Thomson	
AAE 75-5 UILU-ENG 75 0505	Design of High Lift Airfoils with a Stratford Distribution by the Eppler Method	W. G. Thomson	
AAE 75-6 UILU-ENG 75 0506	Prediction of Flame Spreading and Pressure Wave Propagation in Propellant Beds	H. Krier	AIAA J. (in press)
AAE 75-7 UILU-ENG 75 0507	Vigorous Ignition of Granulated Beds by Blast Impact	H. Krier S. Gokhale	Int. J. Heat-Mass Transfer (in press)
AAE 75-8 UILU-ENG 75 0508	Solid Propellant Burning Evaluation with the Dynagun Ballistic Simulator	H. Krier T. G. Nietzke M. J. Adams J. W. Black E. E. Meister	
AAE 75-9 UILU-ENG 75 0509	Structural Reliability & Minimum Weight Analysis for Combined Random Loads & Strengths	H. H. Hilton	AIAA J. (in press)

RECENT AERONAUTICAL AND ASTRONAUTICAL ENGINEERING DEPARTMENT TECHNICAL REPORTS (Continued)

Technical Report Number	Title	Author	Journal Publication
AAE 75-10 UILU-ENG 75 0510	Linear Viscoelastic Analysis with Random Material Properties	H. H. Hilton J. Hsu J. S. Kirby	
AAE 76-1 UILU-ENG 76 0501	Two Degree of Freedom Flutter of Linear Viscoelastic Wings in Two Dimensional Flow	C. F. Vail H. H. Hilton	In press AIAA J.
AAE 76-2 UILU-ENG 76 0502	An Error Analysis of Computerized Aircraft Synthesis	V. V. Volodin H. H. Hilton	In press J. of Aircraft
AAE 76-3 UILU-ENG 76 0503	Reactive Two-Phase Flow Models Applied to the Prediction of Detonation Transition in Granulated Propellant	H. Krier M. Dimitstein S. S. Gokhale	
AAE 76-4 UILU-ENG 76 0504	Transient Temperature Response of Charring Composite Slabs	J. E. Prussing H. Krier	
AAE 76-5 UILU-ENG 76 0505	Nonlinear Response of Laminated Composite Material Cylindrical Shells	A. R. Zak J. N. Craddock	
AAE 76-6 UILU-ENG 76 0506	An Investigation of Blast Waves Generated from Non-Ideal Energy Sources	A. A. Adamczyk	
AAE 77-1 UILU-ENG 77 0501	Nonlinear Dynamic Analysis of Flat Laminated Plates by the Finite Element Method	A. R. Zak	
AAE 77-2 UILU-ENG 77 0502	An Investigation of Blast Waves Generated by Constant Velocity Flames	R. T. Luckritz	
AAE 77-3 UILU-ENG 77 0503	On the Blast Waves Produced by Constant Velocity Combustion Waves	R. A. Strehlow R. D. Luckritz	
AAE 77-4 UILU-ENG 77 0504	Direct Initiation of Detonation by Non-Ideal Blast Waves	R. J. Cesarone	
AAE 77-5 UILU-ENG 77 0505	The Blast Wave Generated by Constant Velocity Flames	S. A. Shimpi R. A. Strehlow	

RECENT AERONAUTICAL AND ASTRONAUTICAL ENGINEERING DEPARTMENT TECHNICAL REPORTS (Continued)

Technical Report Number	Title	Author	Journal Publication
AAE 77-6 UILU-ENG 77 0506	Exploratory Studies of Flame and Explosion Quenching	R. A. Strehlow L. C. Sorenson L. D. Savage H. Krier	